





PROCESSING OPTIMIZATION OF SiO<sub>2</sub>-CAPPED ALUMINUM-DOPED ZnO  
AND AMORPHOUS In-Zn-Sn-OXIDE THIN FILMS FOR TRANSPARENT  
HEATER AND NEAR-INFRARED REFLECTING APPLICATIONS

A THESIS SUBMITTED TO  
THE GRADUATE SCHOOL OF NATURAL AND APPLIED SCIENCES  
OF  
MIDDLE EAST TECHNICAL UNIVERSITY

BY

HİLAL AYBIKE CAN

IN PARTIAL FULFILLMENT OF THE REQUIREMENTS  
FOR  
THE DEGREE OF MASTER OF SCIENCE  
IN  
METALLURGICAL AND MATERIALS ENGINEERING

FEBRUARY 2022





Approval of the thesis:

**PROCESSING OPTIMIZATION OF SiO<sub>2</sub>-CAPPED ALUMINUM-DOPED  
ZnO AND AMORPHOUS In-Zn-Sn-OXIDE THIN FILMS FOR  
TRANSPARENT HEATER AND NEAR-INFRARED REFLECTING  
APPLICATIONS**

submitted by **HİLAL AYBIKE CAN** in partial fulfillment of the requirements for  
the degree of **Master of Science in Metallurgical and Materials Engineering,**  
**Middle East Technical University** by,

Prof. Dr. Halil Kalıpçılar  
Dean, Graduate School of **Natural and Applied Sciences,**  
**METU**

Prof. Dr. C. Hakan Gür  
Head of the Department, **Metallurgical and Materials**  
**Engineering, METU**

Prof. Dr. Tayfur Öztürk  
Supervisor, **Metallurgical and Materials Engineering, METU**

Assoc. Prof. Dr. Hasan Akyıldız  
Co-Supervisor, **Metallurgical and Materials Engineering,**  
**Konya Technical University**

**Examining Committee Members:**

Prof. Dr. H. Emrah Ünalın  
Metallurgical and Materials Eng., METU

Prof. Dr. Tayfur Öztürk  
Metallurgical and Materials Eng., METU

Assoc. Prof. Dr. Hasan Akyıldız  
Metallurgical and Materials Eng., Konya Technical University

Assist. Prof. Dr. Fatih Pişkin  
Metallurgical and Materials Eng., Muğla Sıtkı Koçman  
University

Assist. Prof. Dr. Şahin Coşkun  
Metallurgical and Materials Eng., Eskişehir Osmangazi  
University

Date: 09.02.2022

**I hereby declare that all information in this document has been obtained and presented in accordance with academic rules and ethical conduct. I also declare that, as required by these rules and conduct, I have fully cited and referenced all material and results that are not original to this work.**

Name Last name : Hilal Aybike Can

Signature :

## ABSTRACT

### **PROCESSING OPTIMIZATION OF SiO<sub>2</sub>-CAPPED ALUMINUM-DOPED ZnO AND AMORPHOUS In-Zn-Sn-OXIDE THIN FILMS FOR TRANSPARENT HEATER AND NEAR-INFRARED REFLECTING APPLICATIONS**

Can, Hilal Aybike

Master of Science, Metallurgical and Materials Engineering

Supervisor: Prof. Dr. Tayfur Öztürk

Co-Supervisor: Assoc. Prof. Dr. Hasan Akyıldız

February 2022, 164 pages

In this study, AZO/SiO<sub>2</sub> and amorphous In-Zn-Sn-oxide (a-ZITO) functional coatings were developed with combinatorial approach for transparent heater and heat reflecting applications. AZO/SiO<sub>2</sub> and amorphous In-Zn-Sn-oxide (a-ZITO) coatings were obtained via magnetron sputtering. A series of optimization steps were carried out specific to each method and coating type. The samples were produced on 75x50 mm<sup>2</sup> glass substrates. Further, optimum post-deposition annealing conditions were identified as 400 °C and Ar+4% H<sub>2</sub> atmosphere to improve electrothermal properties.

750 nm thick and polycrystalline AZO/SiO<sub>2</sub> coatings displayed impressive room-temperature electrical conductivity of nearly 3774 S/cm with a sheet resistance of 3.53 Ω/□, carrier concentration of 1.14x10<sup>21</sup> cm<sup>-3</sup>, and Hall mobility of 20.48 cm<sup>2</sup>/Vs. These films exhibited very high optical transmittance (96%) in the visible range and reflectance (73% at 2.5 μm) in the NIR region. Electrothermal tests demonstrated that the achievable saturation temperature was 161 °C with a power density of 5981 W/m<sup>2</sup> in case of applying 12 V. Deicing tests were performed with samples cooled to -40 °C and resulted with complete removal of ice/water only within 180 s.

a-ZITO coatings were deposited using a 3” sputtering target on substrates held at 150 °C. This target was prepared within a particular oxide composition which was

determined via combinatorial approach. The films were remained amorphous after the annealing step and demonstrated room-temperature electrical conductivity of 1805 S/cm, sheet resistance of 7.49  $\Omega/\square$ , carrier concentration of  $0.3 \times 10^{21} \text{ cm}^{-3}$ , and Hall mobility of 36.59  $\text{cm}^2/\text{Vs}$ . The transmission in the visible range and reflectance at 2.5  $\mu\text{m}$  were measured as 86% and 35%, respectively. a-ZITO coating was displayed a saturation temperature of 112  $^{\circ}\text{C}$  and a power density of 4635  $\text{W}/\text{m}^2$  whereas defrosting within 173 s (initial temperature -40  $^{\circ}\text{C}$ ) was observed with 12 V input.

**Keywords:** Transparent heaters, Heat reflecting mirrors, AZO, ZITO, Magnetron sputtering

## ÖZ

### **AZO/SiO<sub>2</sub> ve a-ZITO İNCE FİLMLERİN SAYDAM ISITICI VE ISI YANSITMA UYGULAMALARINA YÖNELİK OPTİMİZASYONU**

Can, Hilal Aybike  
Yüksek Lisans, Metalurji ve Malzeme Mühendisliği  
Danışman: Prof. Dr. Tayfur Öztürk  
Eş Danışman: Doç. Dr. Hasan Akyıldız

Şubat 2022, 164 sayfa

Bu tez çalışmasında, saydam ısıtıcı ve ısı yansıtıcı uygulamalarına yönelik olarak AZO/SiO<sub>2</sub> ve amorf In-Zn-Sn-oksit (a-ZITO) fonksiyonel kaplamalar geliştirilmiştir. Her iki kaplama türü de magnetron sıçratma yöntemi ile üretilmiş, fakat a-ZITO kaplamaların geliştirilmesinde kombinatorial yöntemden faydalanılmıştır. Nihai fonksiyonel kaplamalara bir dizi optimizasyon sonrası ulaşılmıştır. Örnekler 75x50 mm<sup>2</sup> cam altlıklar üzerinde biriktirilmiştir. Ayrıca, elektrotermal özelliklerin iyileştirilmesi için biriktirme sonrası tavlama koşulları 400 °C ve Ar+%4 H<sub>2</sub> atmosferi olarak belirlenmiştir.

750 nm kalınlıkta ve polikristalin yapıda üretilen AZO/SiO<sub>2</sub> kaplamalar, oda sıcaklığında 3774 S/cm elektriksel iletkenlik, 3,53 Ω/□ düzlemsel direnç, 1,14x10<sup>21</sup> cm<sup>-3</sup> taşıyıcı konsantrasyonu ve 20,48 cm<sup>2</sup>/Vs Hall mobilitesi değerlerini sağlarken, görünür bölgede %96 ışık geçirgenliği ve 2,5 µm'de %73 reflektans sergilemiştir. Elektrotermal testler, 12 V uygulama durumunda 5981 W/m<sup>2</sup> güç yoğunluğu ile yüzey doyum sıcaklığının 161 °C olduğunu göstermiştir. Buz giderme testleri, -40

°C'ye soğutulmuş numunelerle gerçekleştirilmiş ve tüm buz ve suyun giderilmesi için gereken sürenin 180 saniye olduğunu ortaya koymuştur.

Nihai, a-ZITO kaplama kompozisyonu kombinatorial biriktirme yöntemi kullanılarak belirlenmiş ve bu kompozisyon dahilinde üretilen hedef malzemedan, 150 °C altlık sıcaklığında kaplamalar oluşturulmuştur. 750 nm kalınlığındaki ZITO kaplamalar, tavlama sonrası da amorf yapıyı korumuştur. Bu kaplamaların, oda sıcaklığı elektriksel iletkenliği 1805 S/cm, düzlemsel direnci 7,49  $\Omega/\square$ , taşıyıcı konsantrasyonu  $0,3 \times 10^{21} \text{ cm}^{-3}$  ve Hall mobilitesi 36,59  $\text{cm}^2/\text{Vs}$  olarak belirlenirken, görünür bölge ışık geçirgenliği %86 ve 2,5  $\mu\text{m}$ 'de reflektans değeri %35 şeklinde ölçülmüştür. 12 V gerilim altında yüzey doyum sıcaklığı 112 °C, güç yoğunluğu 4635  $\text{W/m}^2$  ve -40 °C'den başlayacak şekilde buz giderme süresi 173 saniye olarak saptanmıştır.

**Anahtar Kelimeler:** Saydam Isıtıcılar, Isı yansıtıcılar, AZO, ZITO, Magnetron Sıçratma

*To my most precious family...*

## ACKNOWLEDGMENTS

I would like to express my sincere gratitude to my thesis advisor Prof. Dr. Tayfur Öztürk for giving me an opportunity to have my masters's in Middle East Technical University. I am indepted to my co-advisor Assoc. Prof. Dr. Hasan Akyıldız for the continuous support of my Master's study and research, for his patience, motivation, enthusiasm, and immense knowledge. His guidance helped me in all the time of research and writing of this thesis. I could not have imagined having a better advisor and mentor for my Master's study. Even at most stressful times, his support was with me. I became a much better researcher with my advisor's expertise.

Besides my advisors, I would like to thank the rest of my thesis committee: Prof. Dr. H. Emrah Ünalın, Assist. Prof. Dr. Şahin Coşkun, and Assist. Prof. Dr. Fatih Pişkin, for their encouragement and insightful comments.

I appreciate all my labmates Yiğit Akbaş, Fahrettin Kılıç, M. Mert Köse, N. Özgür Darıcıoğlu, H. Eda Aysal, Aylin Elçi and Ramin Babazadeh for their lovely friendship and support whenever I need.

Although my family say that they prefer the happiest daughter instead of the most successful one, they always give priority to my education. They raised me as a strong and independent person. They always believed in me, and I felt this. I could not achieve this accomplishment without their support and trust.

Lastly, this study was financially supported by the Scientific and Technological Research Council of Turkey (TUBITAK) under Grant No: 118M013.



## TABLE OF CONTENTS

ABSTRACT.....	v
ÖZ .....	vii
ACKNOWLEDGMENTS .....	x
TABLE OF CONTENTS.....	xi
LIST OF TABLES .....	xiii
LIST OF FIGURES .....	xv
CHAPTERS	
1 INTRODUCTION .....	1
2 LITERATURE REVIEW .....	7
2.1 Overview of Transparent Heaters.....	8
2.2 Transparent Conductive Oxides (TCOs).....	14
2.2.1 Al-doped ZnO (AZO) Transparent Conductive Oxide Thin Films ..	16
2.2.2 Amorphous Transparent Conductive Oxides.....	23
3 EXPERIMENTAL .....	31
3.1 Magnetron Sputtering of AZO/SiO <sub>2</sub> and a-ZITO thin films .....	31
3.2 Post-deposition annealing of thin films.....	37
3.3 Characterization.....	37
4 RESULTS AND DISCUSSION .....	45
4.1 Optimization of Production of AZO Thin Films on Glass Substrates by Magnetron Sputter Deposition.....	45
4.1.1 Thickness optimization .....	45

4.1.2	Annealing optimization .....	51
4.1.3	Deposition temperature optimization .....	56
4.2	Production of AZO/SiO <sub>2</sub> thin films .....	62
4.2.1	Structural analysis of AZO/SiO <sub>2</sub> thin films .....	63
4.2.2	Morphological analysis of AZO/SiO <sub>2</sub> thin films .....	64
4.2.3	Optical analysis of AZO/SiO <sub>2</sub> thin films .....	67
4.2.4	Electrical analysis of AZO/SiO <sub>2</sub> thin films .....	70
4.2.5	Electro-thermal performance of AZO/SiO <sub>2</sub> transparent heaters .....	71
4.3	Optimization of amorphous ZITO thin film production .....	77
4.3.1	Deposition time and sputtering pressure optimization .....	77
4.3.2	Deposition temperature optimization .....	86
4.3.3	Annealing optimization of a-ZITO thin films .....	92
4.4	Production and characterization of a-ZITO transparent heaters .....	112
4.4.1	Visual examination .....	112
4.4.2	Structural examination .....	114
4.4.3	Morphological examination .....	115
4.4.4	Optical analysis of a-ZITO thin films .....	120
4.4.5	Electrical analysis of a-ZITO thin films .....	124
4.4.6	Electro-thermal analysis of a-ZITO thin films .....	128
5	CONCLUSION .....	137
6	FUTURE STUDY .....	141
	REFERENCES .....	143

## LIST OF TABLES

Table 2.1 Comparison of the general properties of transparent conductors [31]....	13
Table 2.2 Comparison of the properties of AZO and ITO thin film transparent electrodes [56].....	17
Table 2.3 Basic properties of crystalline and amorphous TCOs.....	23
Table 3.1 The achieved film thicknesses after 30 min of depositions with samples #1 (corner) and #8/9 (center) as a function of sputtering power.....	35
Table 4.1 Thickness dependent structural properties of AZO thin films deposited at RT with various thicknesses .....	47
Table 4.2 Optical properties depending on thickness and annealing condition in RT deposited AZO thin films.....	53
Table 4.3 Electrical properties depending on thickness and annealing condition in RT deposited AZO thin films. ....	54
Table 4.4 FOM values depending on thickness and annealing condition in RT deposited AZO thin films.....	55
Table 4.5 Structural properties of 750 nm thick AZO films produced at substrate temperatures of 100, 200 and 300 °C.....	57
Table 4.6 Electrical properties of 750 nm thick AZO thin films produced at different substrate temperatures.....	59
Table 4.7 Comparison of the optical properties of 750 nm thick AZO thin films in as-deposited state and after annealing under various atmospheres.....	60
Table 4.8 Comparison of the electrical properties of 750 nm thick AZO thin films in as-deposited state and after annealing under various atmospheres.....	61
Table 4.9 Comparison of the FOM values of 750 nm thick AZO thin films in as-deposited state and after annealing under various atmospheres .....	62
Table 4.10 Electrical properties Measurements of as-deposited and annealed AZO/SiO <sub>2</sub> thin films.....	71
Table 4.11 EDX results belongs to ZITO thin film samples 1, 5, 9, 13, 16, and 21 deposited for 45 min at a sputtering pressure of 10 mTorr.....	81

Table 4.12 Optical properties of a-ZITO thin films deposited at 10 mTorr sputtering pressure for 45 min.....	86
Table 4.13 Optical properties of a-ZITO thin films deposited at 10 mTorr sputtering pressure and 250 °C substrate temperature for 45 min.....	90
Table 4.14 Optical properties of a-ZITO films annealed in Ar atmosphere at 400 °C for 1 h after being deposited at RT under 10 mTorr sputtering pressure for 45 min .....	99
Table 4.15 Optical properties of a-ZITO films annealed in Ar+4% H <sub>2</sub> atmosphere for 1 h after being deposited at RT under 10 mTorr sputtering pressure for 45 min ..	104
Table 4.16 Optical properties of a-ZITO thin films annealed successively in Ar+4%H <sub>2</sub> and Ar atmospheres for 1 h at 400 °C .....	108
Table 4.17 Candidate samples for a-ZITO transparent heater production .....	110
Table 4.18 Hall effect measurement results for a-ZITO thin films deposited at various substrate temperatures and after annealing for 90 min at 400 °C in Ar+4 % H <sub>2</sub> atmosphere.....	126

## LIST OF FIGURES

Figure 1.1. Schematic representation of transparent heaters currently in use/in development; as can be seen, transparent heaters include one of four primary material groups (metal oxides, metals, conductive polymers, and carbon) or a combination of these in the form of hybrid/nanocomposite systems. The figure also reveals the diversity and abundance of materials in transparent heaters technology.....	3
Figure 2.1. Pictures showing the melting of snow on an automobile windshield by a 30 x 47 cm <sup>2</sup> Cu-NWs mesh type transparent heater [23].....	11
Figure 2.2. Visible and IR region transmittance of ITO, AZO, PEDOT: PSS (poly(3,4-ethylene dioxythiophene) polystyrene sulfonate), silver nanowires, and carbon nanotube coatings ( <i>R<sub>s</sub></i> values of coatings are given in parenthesis) [31]....	12
Figure 2.3. <b>a)</b> Structure of a typical smart glass coated with a TCO heater [41] <b>b)</b> Optical interference formation due to ITO transparent heater coating on an airplane cockpit windshield. The film thickness is not uniform on the entire surface to ensure homogenous heating [42].....	15
Figure 2.4. <b>a)</b> Transmittance, reflectance and absorption values of 670 nm thick AZO thin film coated on glass by sputter deposition [75], <b>b)</b> Variation of resistivity ( $\rho$ ), carrier concentration ( $n_e$ ) and Hall mobility ( $\mu$ ) values as a function of substrate temperature in AZO thin films deposited with PLD [68], <b>c)</b> The change in the transmittance of AZO thin films up to 3000 nm as a function of sputtering power [76].....	20
Figure 2.5 <b>a)</b> Schematic overview of the combinatorial deposition process, <b>b)</b> ZnO-ITO sample libraries obtained via using the deposition geometry given in (a) [117] .....	26
Figure 2.6 The change in the electrical resistance, carrier concentration, and mobility of ZITO thin films as a function of at. Zn % in the composition and RF power used in ZnO sputtering [117] .....	27
Figure 3.1 Thin-film deposition geometry used for the sample production .....	32
Figure 3.2 Multi-substrate carrier magazines employed in the deposition of <b>a)</b> AZO/SiO <sub>2</sub> , <b>b)</b> a-ZITO, and deposition geometries for <b>c)</b> AZO/SiO <sub>2</sub> , <b>d)</b> a-ZITO thin films. (Substrates were rotated at 8 rpm during AZO/SiO <sub>2</sub> thin film deposition) ..	33

Figure 3.3 <b>a)</b> Schematic drawing of the arrangement of the components in the vacuum chamber, <b>b)</b> Schematic drawing of the deposition geometry used during the optimization step of a-ZITO thin-film production via combinatorial approach (t: the thickness of the depositing film) .....	34
Figure 3.4 <b>a)</b> General view of the system used in the electrical property measurements of the thin films, <b>b)</b> a closer view of the probe station of the system in Van der Pauw geometry .....	41
Figure 3.5 <b>a)</b> General view of the system used for electrothermal measurements, <b>b)</b> sample, <b>c)</b> schematic drawing of the system .....	42
Figure 4.1 XRD patterns of AZO thin films deposited at RT and thicknesses of 250, 500, 750, and 1000 nm. ....	46
Figure 4.2 Surface SEM images of AZO thin films deposited at RT with various thicknesses; <b>a)</b> 250 nm, <b>b)</b> 500 nm, <b>c)</b> 750 nm, <b>d)</b> 1000 nm.....	48
Figure 4.3 Cross-sectional SEM images of AZO thin films deposited at RT with various thicknesses; <b>a)</b> 250 nm, <b>b)</b> 500 nm, <b>c)</b> 750 nm, <b>d)</b> 1000 nm .....	48
Figure 4.4 Transmittance spectra of AZO thin films deposited at RT with various thicknesses (The inset shows the estimated direct band gap energy of the films) ..	50
Figure 4.5 Electrical properties of AZO thin films deposited at RT with various thicknesses.....	51
Figure 4.6 Transmittance spectra of AZO thin films (RT, 250–1000 nm) after annealing under various atmospheres for 1 h; <b>a)</b> vacuum, 300 °C, <b>b)</b> Ar, 400 °C, <b>c)</b> Ar + 4% H <sub>2</sub> , 400 °C (The insets show the estimated direct band gaps of the films for each condition) .....	52
Figure 4.7 XRD patterns of 750 nm thick AZO thin films deposited at 100, 200, and 300 °C substrate temperatures .....	56
Figure 4.8 <b>a)</b> Transmittance spectra and <b>b)</b> electrical properties of 750 nm thick AZO thin films as a function of substrate temperature (The inset in (a) show the estimated direct band gaps of the films) .....	58
Figure 4.9 <b>a)</b> Transmittance spectra, <b>b)</b> Tauc plots and direct band gap values of 750 nm thick AZO thin film deposited at 200 °C and annealed under various atmospheres .....	60

Figure 4.10 Digital images of 750 nm thick AZO/SiO <sub>2</sub> thin film <b>a)</b> deposited at 200 °C, <b>b)</b> after annealing under Ar+4% H <sub>2</sub> atmosphere for 1 h at 400 °C.....	63
Figure 4.11 <b>a)</b> XRD patterns of AZO and AZO/SiO <sub>2</sub> thin films deposited at substrate temperature of 200 °C, along with annealed AZO/SiO <sub>2</sub> thin film <b>b)</b> Magnified view of the (002) peaks for the given pattern (a).....	63
Figure 4.12 AFM surface images of AZO and AZO/SiO <sub>2</sub> thin films <b>a)</b> deposited at 200 °C, <b>b)</b> SiO <sub>2</sub> top layer coated at RT following the deposition at 200 °C (inset images (a) and (b) provide a general view of the surface).....	65
Figure 4.13 AFM surface topography of <b>a)</b> 200 °C as-deposited AZO, <b>b)</b> SiO <sub>2</sub> capped as-deposited AZO, and FE-SEM surface images of <b>c)</b> 200 °C as-deposited AZO, <b>d)</b> Ar+4% H <sub>2</sub> annealed AZO/SiO <sub>2</sub> (the insets given in (c) shows the general view of the surface of as deposited AZO and (d) cross-section FE-SEM image of Ar + 4% H <sub>2</sub> annealed AZO/SiO <sub>2</sub> sample) .....	66
Figure 4.14 <b>a)</b> Transmittance spectra and <b>b)</b> Tauc's plots of as-deposited AZO, SiO <sub>2</sub> capped as-deposited AZO, and Ar+4% H <sub>2</sub> annealed AZO/SiO <sub>2</sub> thin films.....	68
Figure 4.15 Reflectance spectra of as-deposited AZO, SiO <sub>2</sub> capped as-deposited AZO, and Ar+4% H <sub>2</sub> annealed AZO/SiO <sub>2</sub> thin films .....	69
Figure 4.16 Electro-thermal response of AZO/SiO <sub>2</sub> transparent heater; <b>a)</b> thermal response of the heater to incremental input voltage increase, <b>b)</b> heating behavior under different applied voltages, <b>c)</b> surface temperature vs power density plot, <b>d)</b> long term loading stability, <b>e)</b> cyclic loading performance of the heater (the insets in a, b, and d refer to thermal camera images of the sample at the relevant temperature) .....	73
Figure 4.17 <b>a)</b> Deicing performance and heating curves of dry-ice cooled AZO/SiO <sub>2</sub> transparent heater with various input voltages, <b>b)</b> digital images showing the course of deicing on 5.0 x 7.5 mm <sup>2</sup> AZO/SiO <sub>2</sub> transparent heater under 12 .....	75
Figure 4.18 Digital images of ZITO thin films deposited at 5 mTorr sputtering pressure for various deposition time <b>a)</b> 15 min, <b>b)</b> 30 min, <b>c)</b> 45 min, and <b>d)</b> 60 min (the center schematic drawing shows the arrangement of the substrates on the carrier magazine with reference to gun 1, 2, and 3) .....	77

Figure 4.19 Sheet resistance of ZITO thin films deposited at 5 mTorr sputtering pressure for 15, 45, and 60 min .....	78
Figure 4.20 Digital images of ZITO thin films deposited at 10 mTorr sputtering pressure <b>a)</b> 45 min, <b>b)</b> 60 min .....	79
Figure 4.21 Sheet resistance of ZITO thin films <b>a)</b> deposited at 10 mTorr sputtering pressure for 45 and 60 min, <b>b)</b> deposited at 5 mTorr and 10 mTorr sputtering pressures for 45 min .....	81
Figure 4.22 EDX results of samples 1, 5, 9, 13, 16, and 21 deposited for 45 min at 10 mTorr sputtering pressure (relevant sample numbers and their location on the sample holder are given as insets) .....	83
Figure 4.23 XRD patterns of ZITO thin films deposited at 10 mTorr sputtering pressure for 45 min .....	84
Figure 4.24 <b>a)</b> Transmittance spectra, <b>b)</b> Tauc's plots of a-ZITO thin films deposited for 45 min at 10 mTorr sputtering pressure .....	85
Figure 4.25 The digital images of a-ZITO thin films deposited at 10 mTorr sputtering pressure for 45 min at different substrate temperatures, <b>a)</b> 250 °C, <b>b)</b> RT (given as comparison) .....	87
Figure 4.26 XRD patterns of a-ZITO thin films deposited for 45 min at a sputtering pressure of 10 mTorr and a substrate temperature of 250 °C .....	87
Figure 4.27 <b>a)</b> Transmittance spectra, <b>b)</b> Tauc's plots of a-ZITO thin films deposited at 10 mTorr sputtering pressure and 250 °C substrate temperature for 45 min .....	89
Figure 4.28 Sheet resistance values of a-ZITO thin films deposited at RT and 250 °C substrate temperatures for 45 min at 10 mTorr sputtering pressure .....	91
Figure 4.29 Digital images of a-ZITO thin films produced for 45 min at 10 mTorr sputtering pressure and RT, <b>a)</b> as deposited, <b>b)</b> annealed in air atmosphere for 1 h at 400 °C, <b>c)</b> sheet resistance of thin films given in (a) and (b) .....	93
Figure 4.30 XRD patterns of ZITO thin films in as-deposited state (RT, 45 min, 10 mTorr Ar) and after annealing in air atmosphere at 400 °C for 1 h, <b>a)</b> sample 17, <b>b)</b> sample 18 .....	94



Figure 4.31 Sheet resistance of a-ZITO thin films deposited at RT and then annealed in Ar for 1 h at 300 °C and 400 °C; (the table shows the sheet resistance of samples which are lower than 100 $\Omega/\square$ , in any applied condition) .....	95
Figure 4.32 Digital images of a-ZITO thin films; <b>a)</b> annealed in Ar atmosphere for 1 h at 400 °C, <b>b)</b> in as-deposited state, <b>c)</b> samples with profound change in their transmittance after annealing .....	97
Figure 4.33 <b>a)</b> Transmittance spectra, and <b>b)</b> Tauc's plots of Ar-annealed (400 °C, 1h) a-ZITO thin films, <b>c)</b> comparison of the $T_{vis}$ values of as-deposited and Ar- annealed a-ZITO thin films .....	98
Figure 4.34 Sheet resistance of a-ZITO thin films deposited at RT and then annealed in Ar+4% H <sub>2</sub> for 1 h at 400 °C (the table shows the sheet resistance of samples lower than 100 $\Omega/\square$ , in any applied condition) .....	100
Figure 4.35 Digital images of a-ZITO thin films <b>a)</b> annealed in Ar+4% H <sub>2</sub> atmosphere for 1 h at 400 °C, <b>b)</b> in as-deposited state, <b>c)</b> samples with profound change in their transmittance after annealing .....	102
Figure 4.36 <b>a)</b> Transmittance spectra, and <b>b)</b> Tauc's plots of Ar+4% H <sub>2</sub> annealed (400 °C, 1h) a-ZITO thin films, <b>c)</b> comparison of the $T_{vis}$ values of as-deposited, Ar annealed and Ar+4% H <sub>2</sub> annealed a-ZITO thin films.....	103
Figure 4.37 Digital images of a-ZITO thin films <b>a)</b> successively annealed in Ar+4% H <sub>2</sub> and Ar atmospheres for 1 h at 400 °C, <b>b)</b> in as-deposited state, <b>c)</b> samples with profound change in their transmittance after annealing.....	106
Figure 4.38 <b>a)</b> Transmittance spectra, <b>b)</b> Tauc's plots of a-ZITO thin films annealed successively in Ar+4% H <sub>2</sub> and Ar atmospheres for 1 h at 400 °C.....	107
Figure 4.39 <b>a)</b> Sheet resistance of as-deposited (RT, 45 min), and annealed (successively in Ar+4 % H <sub>2</sub> and Ar for 1 h, 400 °C) a-ZITO thin films, <b>b)</b> $T_{vis}$ values of as-deposited and annealed a-ZITO thin films (data for various annealing atmospheres denoted via different colored spheres) .....	109
Figure 4.40 EDX spectrum and elemental composition of sample 18 (the sample was obtained under 10 mTorr sputtering pressure for 45 min and on substrates kept at RT) .....	111

Figure 4.41 Digital images of a-ZITO thin films deposited at various substrate temperatures, <b>a)</b> on 18 mm diameter glass substrates <b>b)</b> on 5 cm x 7.5 cm glass substrates, left; as-deposited, right; after annealing under Ar+4% H <sub>2</sub> atmosphere for 1.5 h at 400 °C.....	113
Figure 4.42 XRD patterns of a-ZITO thin films deposited on glass substrates at various temperatures <b>a)</b> as-deposited, <b>b)</b> after annealing in Ar+4% H <sub>2</sub> atmosphere at 400 °C for 90 min. ....	114
Figure 4.43 Surface SEM images of a-ZITO thin films produced at various substrate temperatures, as-deposited <b>a)</b> RT, <b>c)</b> 150 °C, <b>e)</b> 250 °C, after annealing in Ar+4% H <sub>2</sub> atmosphere at 400 °C for 90 min. <b>b)</b> RT, <b>d)</b> 150 °C, <b>f)</b> 250 °C (inset images provide general view for the surfaces) .....	116
Figure 4.44 3D AFM images of a-ZITO thin films produced at various substrate temperatures, as-deposited <b>a)</b> RT, <b>c)</b> 150 °C, <b>e)</b> 250 °C, after annealing in Ar+4% H <sub>2</sub> atmosphere at 400 °C for 90 min. <b>b)</b> RT, <b>d)</b> 150 °C, <b>f)</b> 250 °C.....	117
Figure 4.45 Through thickness fracture surface SEM images of a-ZITO thin films produced at various substrate temperatures, as-deposited <b>a)</b> RT, <b>c)</b> 150 °C, <b>e)</b> 250 °C, after annealing in Ar+4% H <sub>2</sub> atmosphere at 400 °C for 90 min. <b>b)</b> RT, <b>d)</b> 150 °C, <b>f)</b> 250 °C. (inset images provide general views of the surfaces).....	118
Figure 4.46 EDX analyses of a-ZITO thin films produced at various substrate temperatures, as deposited at <b>a)</b> RT, <b>c)</b> 150 °C, <b>e)</b> 250 °C, after annealing in Ar+4% H <sub>2</sub> atmosphere at 400 °C for 90 min. (The inset tables denote the elemental ratio of the cations present in the samples) .....	119
Figure 4.47 Transmittance spectra and Tauc's plots of a-ZITO thin films produced at various substrate temperatures, <b>a)</b> and <b>b)</b> as-deposited, <b>c)</b> and <b>d)</b> after annealing in Ar+4% H <sub>2</sub> atmosphere at 400 °C for 90 min. (the inset numerical values given in (b) and (d) denotes the band gap values of the corresponding samples).....	121
Figure 4.48 <b>a)</b> Reflectance spectra, and <b>b)</b> absorption spectra of a-ZITO thin films deposited at 150 °C substrate temperature and annealed at 400 °C Ar+4% H <sub>2</sub> for 90 min.....	122
Figure 4.49 Electrical properties of a-ZITO thin films as a function of substrate temperature <b>a)</b> Sheet resistance and <b>b)</b> resistivity values of the films in as-	

deposited state and after annealing for 90 min at 400 °C in Ar+4 % H <sub>2</sub> atmosphere. .....	124
Figure 4.50 Heating behaviour of a-ZITO transparent heaters as a function of applied voltage <b>a)</b> RT deposited, <b>b)</b> annealed, <b>c)</b> 150 °C deposited, <b>d)</b> annealed, <b>e)</b> 250 °C deposited, <b>f)</b> annealed (annealing was performed at 400 °C for 90 min under Ar+4% H <sub>2</sub> atmosphere, the inset images given in each figure refers to the thermal camera image of the sample at the corresponding saturation temperature) .....	129
Figure 4.51 Heating behavior of annealed a-ZITO thin films under 12 V .....	131
Figure 4.52 Electro-thermal response of 150 °C deposited a-ZITO transparent heater after annealing under Ar+4% H <sub>2</sub> for 90 min at 400 °C; <b>a)</b> thermal response of the heater to incremental input voltage increase, <b>b)</b> long-term loading stability, <b>c)</b> cyclic loading performance of the heater, <b>d)</b> power density vs. surface saturation temperature plot (the insets in (a) and (b) refer to thermal camera images of the sample at the relevant temperature) .....	132
Figure 4.53 <b>a)</b> Deicing performance and heating curves of dry-ice cooled a-ZITO transparent heater with various input voltages <b>b)</b> digital images showing the course of deicing under 12 V on 5.0 x 7.5 mm <sup>2</sup> a-ZITO transparent heater (the insets given in (a) shows the thermal camera images of the sample during deicing at some certain time and temperatures).....	134



## **CHAPTER 1**

### **INTRODUCTION**

Outdoor materials, including the photovoltaic cells, luminous diodes, panels, touch screens, and glass surfaces, are highly affected by environmental factors. For example, they may lose their functionality in terms of visible region transparency due to condensation below dew point or icing even at lower temperatures.

The icing or fogging of any surface is a usual climatic phenomena and seems quite ordinary, but it actually cause many problems related to variety of applications such as billboards that require transparency to display informations/advertisements, commercial freezers used in the markets, bus stops and traffic lights, security cameras on streets or buildings that need transparency for recording, optical systems (camera and sensors), front/rear and fog lights used in automobiles, flight control tower glasses at airports, sports goggles, windows or windshields of marine, air or railway vehicles, and etc.

In case of automobiles, fogging or icing in the cold seasons may cause undesirable results in terms of energy and safety issues. Today, the traditional technology to defog or deice an automobile windshield requires blowing of the preheated air to the corresponding glass surface. Currently, the heating of this blowing air is provided by the waste heat of the engine. Especially in the case of deicing, additional fuel consumption may be needed up to 20 to 30 min to generate a sufficient amount of waste heat. Further, warm air blowing is an inefficient process due to the low thermal conductivity of air ( $\sim 0.025$  W/mK at 25 °C), thus causing loss of energy and time. The second problem related to fogging/icing is the interruption of the driver's vision, which is extremely important for driving safety.

On the other hand, considering the hot weather conditions, another undesirable environmental effect occurs due to the solar radiation beyond the visible region of the spectrum. About 50% of the total radiation coming from the sun is in the near-infrared (IR) region ( $0.8\ \mu\text{m}$  -  $2.5\ \mu\text{m}$ ). Radiation at these wavelengths may increase the temperature of the interior of an automobile, simply by passing through the transparent windows. In addition, substances that absorb the sunlight can re-radiate the heat in the form of IR radiation at the wavelength range of  $2.5$  to  $20\ \mu\text{m}$ , and therefore indirectly increase the heat of the indoor environments. In this case, two different problems arise for the automobiles. The first is that the air conditioning, which is preferably used to cool down the cabin, causes high fuel consumption. The other one is the damage that may occur on the interior surfaces and driver/passenger skin due to long-term exposure to the sun.

These problems may be solved using special types of optical coatings which covers a variety of materials for different purposes. Figure 1.1 shows these material systems. As seen from this figure, metals, metal oxides, polymers, carbon-based materials, and their hybrids can be used for heating or spectral filter purposes. Here, the principal approach is the deposition of a transparent conductive layer which consists one of these functional materials or their hybrids on a substrate, such as glass. Among them, metal oxides are the first employed group for transparent heater applications. The process was developed during the World War II for the windshields of airplanes. In this application, the windshield was coated with transparent and conductive Antimony-doped Tin Oxide ( $\text{SnO}_2\text{:Sb}$ ) layer using the pyrolysis method. Then, by applying a specific voltage to this coating, the temperature of the windshield was increased, thereby the airplane could operate at higher altitudes in cold weather conditions without any frosting on the windows. Joule heating of the windshield or side windows with transparent heaters is still essential today for automobiles, marine, railway or aeronautical transportation applications [1], [2].

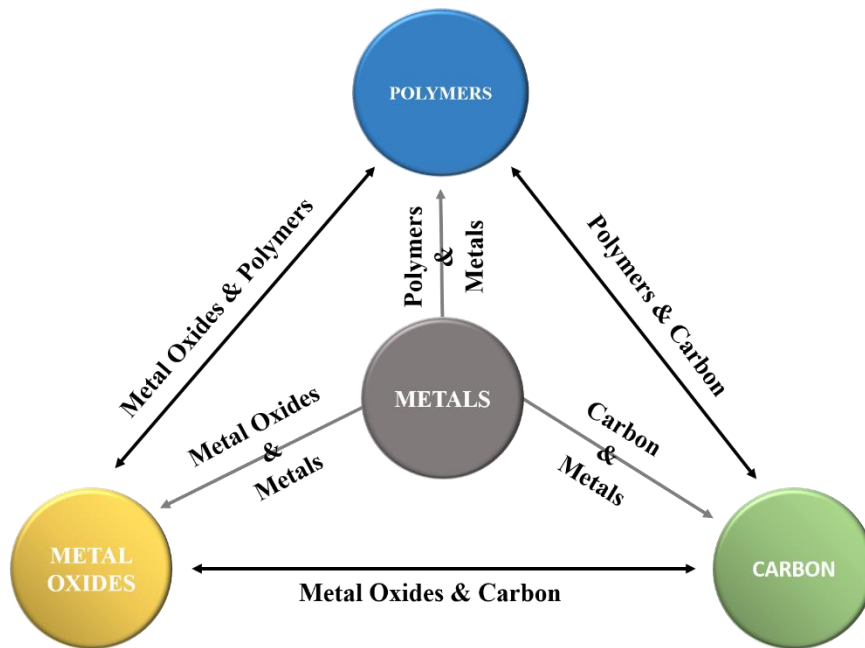


Figure 1.1. Schematic representation of transparent heaters currently in use/in development; as can be seen, transparent heaters include one of four primary material groups (metal oxides, metals, conductive polymers, and carbon) or a combination of these in the form of hybrid/nanocomposite systems. The figure also reveals the diversity and abundance of materials in transparent heaters technology

Transparent heaters are functional coatings/devices exhibiting electrical conductivity and transmittance in the visible region. According to Joule's law, a current " $I$ " passing through a homogeneous conductive material with electrical resistance " $R$ " releases heat of  $I^2R$  per unit time [3]. Therefore, when a potential applied through the edges of a transparent heater layer, the material heats up due to the Joule effect. With this effect, the material reaches a saturation temperature depending on the balance between the applied power and heat losses [4]. Heat loss occurs in three ways. These are losses; i) by conduction to the substrate, ii) to the surrounding by convection, and iii) by radiation emitted from the hot surface.

Today the market for transparent heaters covers a wide range of industrial field such as military technologies, transportation, architectural structures, health, and sports. The research on transparent antennas, smart windows, deicers/defoggers, displays,

thermal therapy pads, and sensors has attracting growing attention. For example, transparent heaters can extend the operating temperature range of liquid crystal displays in cold environments and prevent the formation of fog/ice in many optical systems. In case of specific industrial processes, transparent heaters can keep the displays, microfluidic chips, kiosks, or handheld devices at an appropriate temperature. The fastest development regarding to transparent heaters is observed in the display technologies and smart windows industries. This is mostly depending on the configurable optical and electrical properties of these materials. Today, these devices are on the market with a wide range of visible transmittance, heating power and dimensions both for transport and interior/exterior architecture applications.

The level of optical transmittance required by a transparent heater may vary depending on the application. For example, such a coating in automobile windshield is subjected to narrower limitations than that of smart windows used in the buildings. In terms of visible region transmittance ( $T_{vis}$ ), automobile windshields have to ensure a minimum value of 75% in Europe and 70% in the U.S. and Japan. Further, the coating should reach a sufficient temperature under low input voltages (maximum 12 V) with a minimum response time to remove ice or fog. If heat reflection is required from the coating, the coating should additionally exhibit reflective properties in the IR region.

One of the essential criteria for the heating function is the low sheet resistance ( $R_s$ ). The lower the sheet resistance, the higher the power density (W) obtained under any applied constant voltage.  $R_s$  can be reduced by increasing the coating thickness or electrical conductivity ( $\sigma$ ). On the other hand, visible region transmittance is inversely proportional to the coating thickness. While electrical conductivity can be increased by the carrier concentration ( $n$ ) and Hall mobility ( $\mu$ ) of the material, a decrease in transmittance can be observed. On the other hand, an excessive increase in carrier concentration will decrease the plasma wavelength ( $\lambda_p$ ) due to the inverse ratio between them. For reflectivity in the IR region, a highly conductive coating, high carrier concentration ( $10^{20}$ - $10^{21}$  cm<sup>-3</sup>), and mobility are required [5]. This will



also affect the visible region transmittance of the material. Considering these relationships, optimization of the production process of functional coatings is crucial.

Therefore, the current study aims to produce thin films of transparent conductive oxides which can successfully provide enough heating power to deice an automobile windshield at a shorter time when compared to conventional warm air blowing. For this purpose, two different functional coatings were developed using magnetron sputtering. These were preferred as SiO<sub>2</sub> capped Al-doped ZnO (AZO) as an Indium free composition and amorphous In-Zn-Sn-oxide (a-ZITO) coatings with reduced Indium content compared to the well-known transparent heater material Tin-doped In<sub>2</sub>O<sub>3</sub> (ITO). The samples were obtained on 75x50 mm<sup>2</sup> glass substrates. A series of optimization steps were carried out specific to each coating type. Among them, AZO/SiO<sub>2</sub> thin films were achieved by successive sputtering of high purity AZO and SiO<sub>2</sub> targets, whereas the final composition for a-ZITO coatings were determined by co-sputtering of In<sub>2</sub>O<sub>3</sub>, ZnO, and SnO<sub>2</sub> targets using the combinatorial approach. Then, a mixed oxide target was produced with a single composition based on the results obtained from the combinatorial study. Further, optimum post-deposition annealing conditions were identified for each type of transparent heater coatings.

This thesis comprises 6 chapters. Literature review is presented in Chapter 2 following the introduction section. In Chapter 3, the experimental set-up, optimization steps, and characterizations are given in details. The production of crystalline AZO/SiO<sub>2</sub> thin films and determination of a single a-ZITO composition using the combinatorial approach and deposition of final amorphous mixed oxide thin films are discussed in Chapter 4. These two chapters emphasizes all experimental results, a broad discussion on the optimization and production of these films and their electrothermal properties. The conclusions derived from the current study are given in Chapter 5. Finally, future study is defined in Chapter 6.



## **CHAPTER 2**

### **LITERATURE REVIEW**

Today, the use of smart windows grows continuously in many application areas such as display technologies, construction and automotive industries. Considering the automobiles, the producers aim to increase customer perception, driving/vehicle safety, and passenger comfort by developing new technologies. Smart materials constitute the most important part of these developing technologies. These are relatively new types of materials that designed to alter their properties (shape, stiffness, fluidity, vibration damping, light transmittance, temperature, etc.) in a controlled manner, depending on the external factors such as temperature, pH, voltage, humidity, magnetic field, and light. Examples of these materials include thermo-responsive materials, piezoelectrics, shape memory alloys and polymers, photo-chromic and thermo-chromic materials, electro-rheological, and electro-thermal materials. When considered in this context, driving safety, driving comfort, and energy-saving in automobiles have been increased to higher levels than in the past, with the use of smart windows.

Smart glasses can either be produced to react to external factors by tailoring the glass composition or surface modification (e.g. thin film coating). In applications where functionality is achieved through a coating, for example, the mentioned glass is an automotive windshield, the coating also needs to have a high visible light transmittance (e.g.  $\geq 75\%$  for Europe) [6]. In addition, the deposition method has to allow the coating to be applied on large areas with homogeneous layer thickness. It should be compatible with the thermal expansion of the glass and stable against environmental effects such as humidity. It also has to exhibit enough strength against mechanical effects such as scratching or impacts.

Considering the discussion given above, the main objective of this study is to develop high-performance transparent heater coatings on glass substrates that is free of In or contain reduced amount of In in its composition compared to commercial ITO coatings. In addition, the study aims to examine and determine the heat reflecting behaviour of the coatings in near infrared region. Therefore, the section below, first discusses on which problems can be solved in automobiles by using commercially available transparent conductive materials, then comparing with the alternatives, why AZO/SiO<sub>2</sub> and a-ZITO as the functional coatings and combinatorial approach for thin film processing were preferred within the scope of this study.

## **2.1 Overview of Transparent Heaters**

Transparent heater applications were dominated by transparent conductive oxides until the mid 90's. Depending on the layer thickness, transparent conductive oxides can exhibit electrical conductivity in the range of  $10^3$ – $10^4$  Scm<sup>-1</sup>, with a visible light transmittance of around 90% [7]. Despite their superior optoelectronic properties, due to their ceramic-based nature, these materials are not suitable for flexible applications, such as heating pads used in healthcare. Therefore, for the last two decades, carbon nanotubes, graphene, metallic nanowires, conductive polymers, or hybrid/nanocomposite structures have attracted attention for flexible transparent electrode or heater applications [4], [8]–[10].

ITO is the most widely used material among the traditional transparent heaters, especially for the display applications. However, since In is toxic, rare, and expensive, it does not seem possible to use it in high amounts in near future. For this reason, transparent heaters having compositions with reduced In or without In are becoming more and more critical.

In environments where the air temperature drops, automobile windows can be covered with ice or snow. This situation can easily hinder the vision of the driver. The most common method currently used for defogging/de-icing of the windshields

is the utilization of the waste heat of the engine. The blowing air temperature was raised with this waste heat and then blown to the glass through channels. This is simply, the heating of the glass by convection mechanism [11]. Within this method, if the outside temperature is very low, approximately 20 to 30 min requires to defrost the windshield and reach safe driving conditions [11], [12]. On the other hand, if it is assumed that the electric cars will be the first choice instead of cars with internal combustion engines in near future, a continuous supply of warm blowing air to the windshield by using the waste heat of the engine also appear as a problem that needs to be solved.

Visible light transmittance of the glass parts on automobiles are subjected to some limitations by law. So, any coating layer on the windshield must first provide enough visible transmittance. Since, metal-based thick heating elements that employed on the rear windows can not be used on the windshield due to transmittance concern, micro-wire approach was proposed for the windshields in 1974. This method is still in use today and employ thin (15-29  $\mu\text{m}$  diameter) tungsten wires as the heating element. These wires are used by embedding directly in the glass or more commonly, into the polyvinyl butrial (PVB) layer to provide a certain pattern and fixation between the two glass plates. The wires can be supplied with voltages in the range of 12 to 440 V by the busbars for heating purposes, depending on the type of the application (e.g., higher voltages for marine vehicles). The available heating power can vary between  $0.03 \text{ W/m}^2$  -  $0.3 \text{ W/m}^2$  [13]. Depending on the application, defrosting can be done within 10-15 min (12 min at  $-18^\circ\text{C}$ , and 5 min at  $-7^\circ\text{C}$ ). This approach is much more effective than blowing hot air because no melting is obtained with conventional air blowing within the first 5 min of defrosting.

Although the glass-embedded micro-wire heater approach is widely used in automotive, railroad, and marine vehicles, this approach has certain disadvantages. The first requirement is the production of these wires in low diameters to ensure the visibility is not affected from the wire itself. As for comparison, for a 60-watt 120-volt incandescent lamp, the diameter of the tungsten filament is  $46 \mu\text{m}$  and the efficiency of the lamp increases with a larger filament diameter. As the filament of

a lamp is clearly visible to human eye, the micro-wires for heating applications have to be much thinner than 46  $\mu\text{m}$ . On the other hand, to achieve the necessary power density for homogeneous heating, the distance between the wires must be shortened. Therefore, in this approach optical distortions can occur due to the arrangement of the micro-wires in a pattern, especially during night time driving. [14]. Optical distortions appear in the form of diffractions. Thus, the drivers can easily be distracted due to irritation of their eyes by the head lights of the oncoming cars or streetlights. On the contrary, transparent conductive materials (metallic, carbon, polymeric or oxide-based) can eliminate this problem if they can be applied on the surface of the windshield in the form of a continuous thin film layer.

Silver (Ag) ( $\sigma = 6.3 \times 10^5 \text{ Scm}^{-1}$ ) is one of the most widely studied material in terms of wire-based heater approach [15]. However, Ag exhibits high optical absorption coefficient that prevents light from traveling too far in the material. For Ag thin films to compete with conventional transparent conductive oxides in terms of visible light transmission, the film thickness should not be more than 5-10 nm. Therefore, wire-approach is more reasonable than using the Ag as in the form of a continuous thin film layer for transparent heater applications. Following this idea, Ag-nanowires (AgNWs) with 4-12  $\mu\text{m}$  length and 45-100 nm diameter were produced at relatively low temperatures by the polyol process [16]. These wires can be dispersed in liquids such as methanol/ethanol and coated on substrates using spraying, dropping, Meyer stick, membrane transfer or Langmuir-Blodgett methods [17]–[21]. While the liquid phase is removed by evaporation at room temperature, a mesh structure consisting of randomly oriented wires remained on the substrate. In these coatings,  $T_{vis} = 80\%$  and  $R_s$  values of 10-100  $\Omega/\square$  can be achieved depending on the wire density per unit area [17]–[19]. Each contact point between the AgNWs on this deposit serves for heating purposes due to ohmic resistance. On the other hand, these hot spots also accelerate degradation of the coating and cause problems in long-term use [22]. In addition, considering the requirements for de-icing in automobile windows, the mass production of nanowires is still limited because their prices are quite high. Further,

their applicability to large-area surfaces is limited ( $>100$  mg per  $m^2$ ), the surface roughness is high, and the spacing between the wires causes parasitic lateral currents.

Copper (Cu) is another highly conductive material that is widely studied in transparent heater nano-wire applications. The motivation behind using Cu instead of Ag is the low price of this metal when compared to Ag. Figure 2.1 shows an example on how Cu meshes can be effectively designed for de-icing applications. In this study, a Cu-network is prepared and placed on the inside of a car windshield and heated in a snowy weather under 20 V for 5 min. At the end of this time, snow is melted due to produced heat by the metallic heater, Figure 2.1 (b and c) [23].

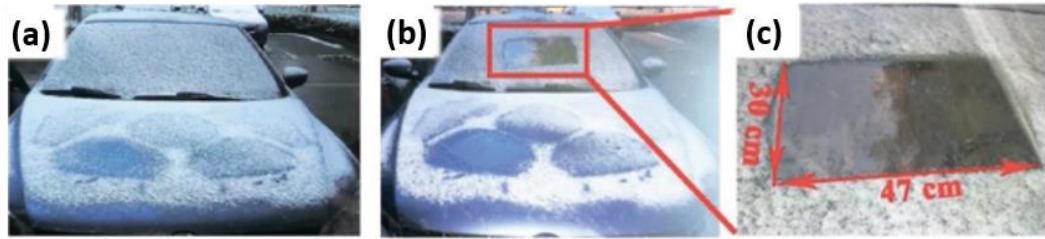


Figure 2.1. Pictures showing the melting of snow on an automobile windshield by a  $30 \times 47 \text{ cm}^2$  Cu-NWs mesh type transparent heater [23]

However, it is known that the oxidation resistance of Cu-based nanowires is quite low. For this reason, many research have been carried out to increase the stability of metallic nano-wires by depositing an organic or inorganic outer layer. For example, a transparent coating made of Cu-nanowires becomes completely electrically non-conductive after 250 min in air at  $75^\circ\text{C}$ . On the other hand, the decrease in conductivity can be decelerated after passivation of the wires with a benzotriazole outer layer and conductivity can be extended up to almost 50 days [24].

Another popular material among the transparent heater's family is graphene. Graphene is the name given to  $sp^2$ -bonded monolayer of carbon (C) atoms in a two-dimensional (2D) honeycomb lattice. Graphene can exhibit very high " $\mu$ " values such as  $>15000 \text{ cm}^2\text{V}^{-1}\text{s}^{-1}$  [25]. It can also be deposited on relatively large substrates

by chemical vapor deposition (CVD) and reduction of graphite oxide [26], [27]. However, graphene coatings can absorb 2.3% of white light even though they are only one atom thick for a single layer [28]. In addition, the sheet resistance of graphene coatings is usually in the order of several hundreds  $\Omega/\square$  [29]. Therefore, the voltage values that will provide the necessary heating are also high. The conductivity can be increased by increasing the layer thickness, but the light transmittance must be sacrificed in this case. Considering the production processes and properties, graphene coatings are more suitable for use in touch screens than automobile glasses and flexible electronic materials due to their high mechanical strength. Since graphene coatings have very high IR region transmittance like AgNWs (see Figure 2.2), their use in this study was not considered [30].

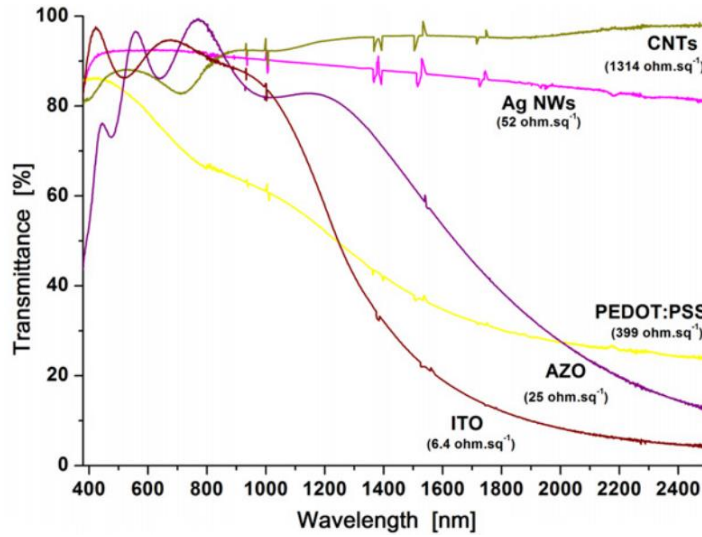


Figure 2.2. Visible and IR region transmittance of ITO, AZO, PEDOT: PSS (poly(3,4-ethylene dioxythiophene) polystyrene sulfonate), silver nanowires, and carbon nanotube coatings ( $R_s$  values of coatings are given in parenthesis) [31]

Another carbon-based material that has been extensively studied for transparent heater applications is the carbon nanotubes (CNT). The electrical properties of single-walled CNTs depend on their chiral vector, that is, in which direction the graphene plate is folded. For transparent heater applications, CNTs can be produced in metallic or semiconductor character, with large sizes or diameters [32]. On the



other hand, the performance of coatings made of carbon nanotubes is not sufficient to work as a heater in large areas such as automobile windshields due to their high contact resistance [33]. But it is also worth to mention here that the commercial heaters based on carbon nanotubes are available today. These coatings are not applicable to large areas as big as a car windshield, but can be applied to headlights on the cars or housings of cameras and sensors [33].

As it is clear from Figure 2.2, the IR reflectance of CNTs ( $\leq 10\%$ ,  $\lambda=1.0 - 2.0 \mu\text{m}$ ) is almost negligible [31], [34]. Moreover, CNTs are both expensive and labor-intensive to manufacture for transparent conductive heater applications [35]. Therefore, the use of this material in this thesis was not considered.

Table 2.1 Comparison of the general properties of transparent conductors [31]

<b>Fabrication method</b>	<b>TCOs</b>	<b>Graphene</b>	<b>CNTs</b>	<b>AgNWs</b>
Chemical vapor deposition	+++	+++	+	-
Sputtering	+++	-	-	-
Spin coating	-	+	++	++
Spray deposition	++	+	+++	+++
Screen printing	--	+	++	++
Cost	Low-High	High	High	Medium
Processing temperature ( $^{\circ}\text{C}$ )	200–1000	RT–1000	RT–700	RT–700
Uniformity	+++	+ to +++	++	++
Typical thickness (nm)	100-300	<5	<10	25 > 600
Typical $R_s$ ( $\Omega/\square$ )	5–100	30–5000	60–300	1–50
Typical transmittance (at 550 nm)	80–97%	80–96%	80–91%	80–96%

Table 2.1 summarizes the discussion given above for the comparison of different type of transparent conductive materials. As can be seen, in terms of transmittance in the optical region, all transparent conductors provide the  $T_{vis} \geq 75\%$  that is the lower limit for automobile windshields. In addition, the  $R_s$  values of carbon-based materials are generally higher than the others. Therefore, it is not appropriate to heat a windshield using carbon-based materials with 12 V supply in automobiles. Further,

when other factors such as applicability to large areas and IR region transmittance are considered, transparent conductive oxides seem more feasible among the others in terms of the objectives of this study.

The haze factor is defined as the ratio between the diffuse transmitted light intensity divided by the total transmitted intensity [36]. As is the case for displays, low haze values are essential for window defrosting applications. Therefore, it is desirable to achieve transparent heaters with low haze, high transmittance and high electrical conductivity all at once. On the other hand, the relationships between the optical scattering, transparency and electrical conductivity of transparent heaters involve trade-offs. The haze factor should be typically below 2 or 3% if the transparent heater is to be used on windscreens, visors or displays to ensure eye comfort in terms of blurriness. The haze factor is generally low for TCOs (especially for vacuum deposited thin films), while it can vary drastically for other transparent heater technologies [4].

Therefore, we aimed to develop two separate transparent conductive oxide coatings instead of using other alternative materials for de-icing and IR reflecting applications. It has been stated in the previous sections that these materials are AZO and ZITO. For this reason, in the following section, an introductory discussion will be given on transparent conductive oxide materials, and then the reasons why AZO and a-ZITO are preferred among many other transparent conductive oxides.

## **2.2 Transparent Conductive Oxides (TCOs)**

Transparent conductive oxides are a group of materials that exhibit both optical transmittance and electrical conductivity. The transmittance in the visible region is due to the wide band gap ( $\geq 3.0$  eV) of these materials and the low electrical resistivity results from high concentration of charge carriers. The carrier concentration increases by forming a degenerate semiconductor through doping of the material with intrinsic defects or extrinsic atoms. In other words, the material can

be modified to become metallically conductive via the shifting of the Fermi level within a band with a large density of states (DoS) [37]. This generates high concentration of mobile charge carriers due to this DoS distribution, degenerate doping in oxide material with widely scattered conduction bands enables high charge carrier mobility and small effective masses with low optical absorption [37], [38]. Furthermore, due to the structure of these highly scattered energy bands, the Fermi level is displaced above the conduction band minimum (CBM) – a phenomenon known as the Burstein-Moss band-filling effect, which enhances the optical bandgap broadening [39], [40]. Many binary metal oxides, such as  $\text{In}_2\text{O}_3$ ,  $\text{SnO}_2$ ,  $\text{CdO}$ , and  $\text{ZnO}$  behave as TCO as a result of the defects created in the structure by intrinsic or extrinsic doping.

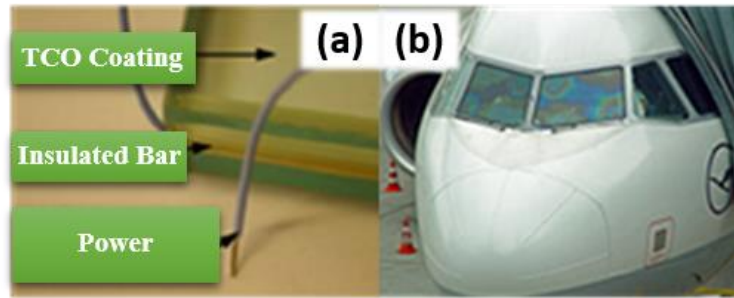


Figure 2.3. **a)** Structure of a typical smart glass coated with a TCO heater [41] **b)** Optical interference formation due to ITO transparent heater coating on an airplane cockpit windshield. The film thickness is not uniform on the entire surface to ensure homogenous heating [42]

As mentioned above, TCO coatings are on the market for transparent heating applications since the World War II. Today, most of the commercially available transparent heating systems used in military equipments or vehicles are based on ITO [43]. ITO coatings can be produced in different thicknesses by sputtering, chemical/physical vapor deposition, and spray pyrolysis methods, Figure 2.3 (a) [41], [44]–[46]. The resistivity of these thin films is generally  $10^{-4} \Omega\cdot\text{cm}$ , and the carrier concentrations are  $\sim 10^{21} \text{ cm}^{-3}$ . Commercially available ITO heaters (diagonal length 2.5-150 cm) can be obtained with  $R_s$  values in the range of 1 to  $350 \Omega/\square$  and

power densities of  $155 - 7750 \text{ W/m}^2$  [47]. These thin films are produced with low defect densities and surface roughness. In addition to their excellent adhesion to the substrate, they are generally coated with an extra protective layer to increase mechanical strength, impact resistance, and chemical stability. Further, additional optical coatings can be applied to improve reflection losses or haze.

Although ITO thin films are widely used in transparent heaters, this material has many disadvantages. ITO coatings are not stable at high temperatures, especially under reducing atmosphere conditions [48]. The films of ITO are quite brittle which makes them suitable for flat and rigid substrates [49]. In order to eliminate this disadvantage, ITO coatings can be coated on an already bended glass, intentionally in non-uniform thickness to provide homogeneous heating. However, this causes aesthetically undesirable colorations, especially at high angles, due to optical interference as seen in Figure 2.3 (b) [42]. Further, In is a rare, expensive and toxic element. At this point, AZO attracts attention because it consists of both less toxic and much cheaper elements compared to ITO.

### **2.2.1 Al-doped ZnO (AZO) Transparent Conductive Oxide Thin Films**

When the literature on transparent heater applications is examined, it is seen that one of the most important candidates among alternative materials that can be used instead of ITO is ZnO due to its relatively low price, availability, and high transmittance [12, 15, 55]. While ZnO has very high electrical resistance in its pure form, coatings with  $10^{-4}$ - $10^{-5} \text{ } \Omega\cdot\text{cm}$  resistivity and  $10^{20}$ - $10^{21} \text{ cm}^{-3}$  carrier concentration can only be obtained if ZnO is doped with other elements [51]. In case of 1-2 wt.% Al doping, electrical and optical properties can be tuned in a wide range by substitutional doping of  $\text{Zn}^{2+}$  ( $0.74 \text{ } \text{\AA}$ ) with  $\text{Al}^{3+}$  ( $0.53 \text{ } \text{\AA}$ ) ions [52]. Moreover, AZO is more stable than ITO under high temperature-reducing atmosphere conditions.

AZO thin films can be produced on variety of substrates by using vacuum or solution-based methods. These methods include spray pyrolysis, magnetron sputtering, sol-gel, and pulsed laser deposition [53]–[55].

Table 2.2 compares the properties of AZO and ITO thin films. As seen from this table, AZO thin films are comparable to ITO coatings in terms of electrical conductivity and visible transmittance. On the other hand, it should be noted that the values given here are measured on films produced by pulsed laser deposition (PLD) or magnetron sputtering methods [16]. Another point is the importance of the oxidizing atmosphere in the production of AZO thin films with a carrier concentration of around  $10^{21} \text{ cm}^{-3}$ . The oxidizing atmosphere significantly effects the amount of oxygen absorption at the surface and grain boundaries. Thus the conductivity decreases in the films produced in a highly oxidizing atmosphere [57]. Therefore, in deposition methods other than PLD, a weak oxidizing atmosphere, target material with low oxygen content, or annealing in a reducing atmosphere is necessary to achieve  $10^{-5} \Omega \cdot \text{cm}$  resistivity values. In addition, AZO thin films exhibit higher crystallinity with PLD, thus the mobility ( $\sim 50 \text{ cm}^2 \text{V}^{-1} \text{s}^{-1}$ ) is higher for PLD deposited thin films compared to that of obtained by magnetron sputtering ( $\sim 25 \text{ cm}^2 \text{V}^{-1} \text{s}^{-1}$ ).

Table 2.2 Comparison of the properties of AZO and ITO thin film transparent electrodes [56]

	<b>AZO</b>	<b>ITO</b>
Resistivity ( $\Omega \cdot \text{cm}$ )	$10^{-5}$	$10^{-5}$
Practical resistivity ( $\Omega \cdot \text{cm}$ )	$2\text{--}3 \times 10^{-4}$	$1 \times 10^{-4}$
$E_g$ (eV)	3.3	3.7
Index of refraction	2	2
Transmittance (@ 550 nm)	> %85	> %90
Cost	Inexpensive	Expensive
Acid solution stability	Good	Stable
Alkali solution stability	Good	Stable
Oxidizing atmosphere at high temperature	Good	Stable
Reducing atmosphere at high temperature	Stable	Good

Table 2.2 also compares the stability of ITO and AZO thin films under different environmental conditions. As seen from the table, AZO is a stable composition at high temperatures, especially under reducing atmosphere, whereas ITO is more stable in acidic, alkaline, high humidity, and oxidizing atmospheres. At this point, it is also worth to mention that the stability of thin films can be improved substantially using a protective capping layer consist of metals, polymers or oxides [48], [58].

AZO thin films produced in this study are coated with a  $\text{SiO}_2$  capping layer. This layer was basically used for two purposes. The first is to isolate the active layer from the environment. A resistive heater for an automobile windshield can be applied to the interior or outer surface of the glass or with the PVB layer in between the two glass layers. In the micro-wire approach, the wires are used together with the PVB layer inbetween the two glass layers to prevent the degradation of the wires due to atmospheric conditions. In terms of efficient heat transfer during deicing, it is reasonable to apply the functional coating to the outer surface of the windshield. This approach requires the exposing of the coating to open atmosphere. Therefore, using a capping layer can be useful to increase the resistance against external factors.

One of the most important disadvantages of transparent conductive oxides obtained by doping is the degradation of electrical properties with aging, especially in humid high temperature atmospheres [59]. In case of AZO, the degradation in time is attributed to the decrease in carrier mobility due to oxygen absorption along the grain boundaries [58], [60]. Capping of the film with a proper top layer is a widely used approach to overcome this problem [58], [61], [62]. Besides metallic top layers, oxides such as  $\text{Al}_2\text{O}_3$  and  $\text{SiO}_2$  are also used as coating materials for TCOs [63], [64]. These extra layers are generally applied to increase light transmission, increase or decrease reflectivity and protect the underlying TCO layer from the environmental factors. For instance, previous studies have shown that the transmittance and electrical stability of AZO thin films can be improved by layering of the films with a  $\text{SiO}_2$  top layer [65], [66]. In addition, this coating can protect the active layer from the detrimental effects of the environment to a certain extent. Therefore, in addition

to environmental concerns, the SiO<sub>2</sub> capping layer was employed to optimize the visible and IR region transmittance of the developed AZO coatings in this study.

As mentioned previously, the heat reflecting properties of the coatings are also important for the purposes of this study. The reflectivity of AZO thin films is known to increase with the increasing film thickness [67]. It was shown that the films deposited at a substrate temperature of 350 °C could exhibit 50% reflectance at a wavelength of 2000 nm [68]. Das and Ray claimed that the IR reflectivity of AZO can be increased by depositing non-stoichiometric films with sputtering gas atmosphere containing hydrogen [69]. In addition, it is known that the reflectivity of AZO can be increased by annealing in a reducing atmosphere [70].

Antireflection coatings are generally used on semiconductor thin films to reduce the surface losses associated with reflected light. These coatings also act as a shield against electromagnetic radiation by scattering the static charges on the surface. For this purpose, two low refractive index materials, i.e., MgF<sub>2</sub> and SiO<sub>2</sub>, are widely used [71], [72]. Following this idea, AZO thin film was deposited in a sandwich structure between two ~100 nm thick SiO<sub>2</sub> layers by magnetron sputtering method [73]. The AZO layer thickness was 800 nm. The average transmission was measured to be  $\geq 90\%$  in the wavelength range of 380-760 nm. In addition, it has been stated that the reflectivity values of this multilayer structure vary between 27- 40 % in the near IR and 70-90% in the mid and far IR regions. Thus, the SiO<sub>2</sub> capping layer used in this study is expected to improve optical properties of AZO thin film layers.

Figure 2.4 (a) shows the optical properties of a 670 nm thick AZO thin film deposited on glass substrate by magnetron sputtering. In AZO and, indeed, in TCOs in general, the transmittance at wavelengths below 400 nm depends on the band gap absorption. In comparison, at wavelengths of 750 nm and above, the number of free charge carriers affects the optical properties. As can be seen from this figure, AZO exhibits a high optical reflectivity with metal-like behavior in the near IR region. The electrical and optical behaviour of AZO thin films can be tailored by microstructural modifications and also by changing the processing parameters [70], [74]. Figure 2.4

(b) and (c) shows the change in the electrical and optical properties of AZO thin films as a function of substrate temperature and sputtering power, respectively. The lowest electrical resistivity value was obtained as  $4.5 \times 10^{-4} \Omega \cdot \text{cm}$  for the thin film sample produced at a substrate temperature of  $350^\circ \text{C}$  with 730 nm thickness. In addition, it has been reported that these films showed the best IR reflectance (15% at 1500 nm and ~50% at 2000 nm) and visible transmittance above 87%. These results indicate that the deposition temperature and the thickness of the film affects the properties significantly. Further, Figure 2.4 (c) clearly shows that the optical properties of AZO thin films can be tuned as a function of sputtering power. The transmittance spectra given in this figure indicates that the visible and near IR transmittance of the films increases with the decrease of sputtering power at constant substrate temperature.

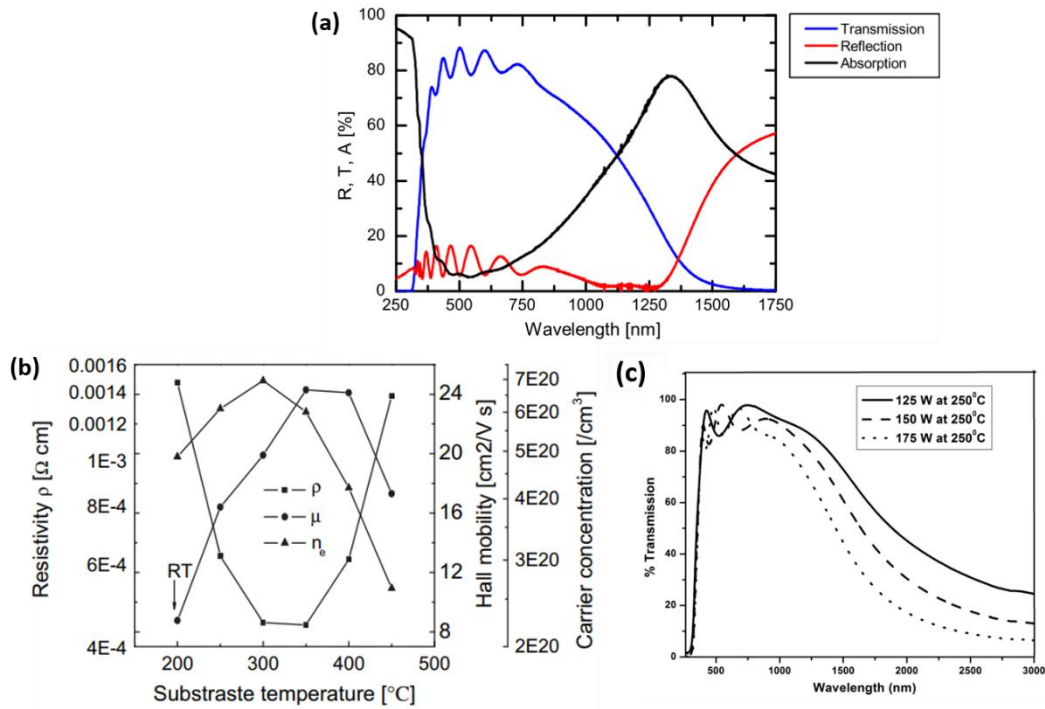


Figure 2.4. **a)** Transmittance, reflectance and absorption values of 670 nm thick AZO thin film coated on glass by sputter deposition [75], **b)** Variation of resistivity ( $\rho$ ), carrier concentration ( $n_e$ ) and Hall mobility ( $\mu$ ) values as a function of substrate temperature in AZO thin films deposited with PLD [68], **c)** The change in the transmittance of AZO thin films up to 3000 nm as a function of sputtering power [76]



As it is clear from the above discussion, the  $R_s$ ,  $T_{vis}$  and IR reflection of AZO thin films are highly dependent on the processing parameters. Therefore, it will be useful to examine the following equations to understand the relationship between the parameters in detail. These equations show the dependency of sheet resistance, carrier concentration and mobility of the charge carriers to the film thickness.

$$\sigma = nq\mu = 1/\rho \quad (2.1)$$

$$R_s = \rho/t \quad (2.2)$$

In equation (2.1),  $\sigma$  ( $S\ m^{-1}$ ),  $\rho$  ( $\Omega\ m$ ), and  $q$  ( $1.6 \times 10^{-19}$  C) refers to electrical conductivity, electrical resistivity, and charge of an electron, respectively. As can be seen from the relationship between  $\sigma$  and  $R_s$ , carrier concentration, carrier mobility, or film thickness must be increased to decrease the sheet resistance or increase the conductivity in TCO thin films.

In the thin films, the onset of infrared reflectivity frequency ( $\omega_c$ ) is related to the plasma frequency ( $\omega_p$ ) according to Equation (2.3).

$$\omega_c = \omega_p(\varepsilon_\infty/\varepsilon_0 - 1)^{1/2} \quad (2.3)$$

Further, the relation between the  $\omega_p$  and  $m_e^*$ ,  $n$ , and  $\mu$  is given in Equations (2.4) and (2.5);

$$\omega_p^2 = ne^2/[\varepsilon_0 m_e^*(\varepsilon_\infty - 1)] - \gamma^2 \quad (2.4)$$

$$\gamma^2 = e/[m_e^* \mu] \quad (2.5)$$

Here,  $m_e^*$  is the effective mass of an electron and equals to  $0.38m_e$ ,  $\varepsilon_0$  is the permittivity of the vacuum, and  $\varepsilon_\infty$  is the dielectric constant at high frequency (3.85). Thus, the plasma wavelength  $\lambda_p$  can be expressed as;

$$\lambda_p = 2\pi\varepsilon_0/\omega_p \quad (2.6)$$

In order to increase the reflectivity in the near IR region,  $\omega_p$  should be increased or  $\lambda_p$  should be decreased. Considering the above equations, it is clear that one of the simplest ways of increasing reflectivity is to increase the carrier concentration and charge mobility. This also led to decrease in the sheet resistance of the film.

According to the literature, the carrier concentration of AZO depends on parameters such as the type of the doping element and its concentration, the deposition method, sputtering gas pressure and its composition, post-deposition annealing temperature and annealing atmosphere [69], [77]–[82].

ZnO can be doped with Al, Ga, B, Sc, Si, V, and F. Very similar optical and electrical properties can be obtained with 2-7 wt.% Ga-doped ZnO thin films compared to AZO [9]. This is due to the localization of electrons in anisotropic *p* or *d* states in the presence of Ga ions. On the other hand, since Ga is an expensive element, it was not considered as a doping agent in this study.

Since the final behaviour of AZO thin films depends on the sputtering parameters, the substrate temperature [82]–[84], sputtering gas pressure [79], [85], [86], and radio frequency power [87] have been widely studied in literature. In addition to these, the crystallinity, surface chemistry and morphology, defect concentration, and electrical and optical properties of the films were tried to be improved by post-deposition annealing under vacuum, Ar, or forming gas atmospheres [88]–[94]. Therefore, to control the optical and electro-thermal properties of AZO coatings, the sputtering deposition conditions must be optimized.

Electrothermal properties of AZO-based transparent heaters on rigid glass substrates have been reported in literature [95]. These studies have shown that the electrothermal properties of the films scatters widely. In addition, the potential of AZO thin films for flexible transparent heater applications were recently revealed on substrates such as polyethylene terephthalate and mica [95], [96]. These examples from the literature showed that AZO thin films can be produced on rigid and flexible

substrates via the sputtering method for a variety of applications including the transparent heaters and heat mirrors.

In this thesis study, AZO thin films were produced using magnetron sputtering method. The deposition temperature, layer thickness and post-deposition annealing of AZO thin films were optimized to achieve thin films with optimum optical and electrical properties. Then, the final coatings were achieved by applying a thin SiO<sub>2</sub> capping layer on top of the AZO layers.

### 2.2.2 Amorphous Transparent Conductive Oxides

As mentioned previously, in this thesis study, a mixture of Zn-In-Sn-oxide was selected as the second coating material. One of the important details about this composition is that the coating is planned to be produced in an amorphous structure. The first study on the production of amorphous TCOs was carried out in 1995 [97]. Comparison of the basic properties of crystalline and amorphous ITO is given in Table 2.3.

As can be seen from this table; amorphous TCOs can exhibit properties comparable to crystalline ones in terms of carrier concentration, mobility, and visible region transmittance.

Table 2.3 Basic properties of crystalline and amorphous TCOs

Property	Crystalline TCOs	Amorphous TCOs
Carrier concentration, $\eta$ (cm <sup>-3</sup> )	$\sim 10^{19}$ (V <sub>O</sub> ) $\sim 10^{21}$ (doping)	$\leq 10^{20}$
Carrier mobility, $\mu$ (cm <sup>2</sup> V <sup>-1</sup> s <sup>-1</sup> )	10-100	10-60
$E_g$ (eV)	$\geq 3$	Reduced optical band gap
Transmittance (visible region, %)	80–90%	Transparent upon Burstein–Moss shift
Production temperature	High	Low
Mechanical behavior	Brittle	Flexible

As an advantage, amorphous TCOs can be produced at relatively lower temperatures when compared to their crystalline counterparts. This simplifies the deposition process and extends the range of usable substrates, for example, to polymers. More importantly, amorphous films are not brittle like crystalline ones. As it is well known, crystalline ITO thin films are brittle in nature and its optoelectronic properties deteriorates by mechanical deformation [98]. In addition to low-temperature production and mechanical flexibility, amorphous TCOs exhibit lower surface roughness than crystalline-ITO. They are also more stable at higher temperatures i.e., 350-600 °C [99]–[101]. Further, the films are chemically and electrically stable for long periods under atmospheric conditions, even at very high doping amounts [102].

Commercially available TCOs mainly consist of In, Ga, Zn, Sn, and Cd oxides. These elements belong to heavy metal cation group, and their electronic configuration is  $(n-1) d^{10} ns^0$ . Binary oxides of these elements show strong s-character. Due to the large spherical s-orbitals in the amorphous structure, the overlap of the “ $ns$ ” orbitals causes the formation of conduction channels for electron transport. Therefore the electrical conductivity of amorphous TCOs (due to high mobility) can be quite high [103]. In addition, the lack of grain boundaries in the amorphous structure reduces carrier scattering [98].

In TCOs, carrier concentration and plasma wavelength are inversely proportional ( $\lambda_p \propto 1/n)^{1/2}$ ). Therefore, the best way to increase the electrical conductivity without reducing light transmission is to increase mobility. Amorphous TCOs are also advantageous at this point as they have high carrier mobility [104]. In addition, short-distance ordering is similar in amorphous and crystalline structures. The difference is that the bond angles vary in the amorphous structure. However, this does not prevent electron conduction. Moreover, the absence of high electron density traps in the band gap with strong ionic bonding also contributes to mobility. In amorphous TCOs, carriers are typically formed due to anion vacancies. Cation doping does not increase the number of carriers but increase the stability of the amorphous phase. Therefore, the carrier density of the amorphous TCOs can be modified in a wide

range without decreasing the carrier mobility. In crystalline TCOs, electron mobility is mainly determined by ionized impurities, phonons, and grain boundary scattering. On the other hand, in amorphous TCOs the mobility determined by the local distortions in metal-oxygen polyhedra and by the long-distance structural ordering, if present. Considering the discussion given above, it is clear that amorphous TCOs can exhibit good electrical properties due to their unique structure.

When the literature on amorphous TCOs is examined, it can be seen that three basic approaches were followed in the production of these materials. The first is the amorphization of already existing TCOs (e.g., AZO or ITO) [105], [106]. Amorphous thin films of these materials are generally produced by vacuum deposition methods on substrates maintained at low temperatures, e.g., liquid N<sub>2</sub> cooled substrates for AZO deposition. It is also noted that the literature on this field has been focused basically on how the properties are changing with the amorphous structure and the dependence of these properties on parameters such as substrate temperature, deposition pressure, and atmosphere. The second approach is to form amorphous oxide systems by heavy doping of In<sub>2</sub>O<sub>3</sub> with elements such as Zn, Ti, Mo, ZnO with Al and Sn, and SnO<sub>2</sub> with elements such as Ga and Zn [107]–[109]. The third and final approach is based on making In<sub>2</sub>O<sub>3</sub> amorphous by doping with at least two of the elements such as Zn, Ga, and Sn [100]–[102], [110]–[116].

Within the context of these approaches, amorphous TCOs are produced using two different techniques. The first one is to produce a single composition sputtering target using powder metallurgy processes. This target consists of the respective composition of the relevant oxides and a single composition thin film samples are produced from this source [109], [110], [113]. However, it takes quite a long time to develop new materials (compositions) with this approach. Therefore, this method may be preferred for the production of the samples if only one well-known composition is aimed. The second method is the use of the combinatorial approach [107], [108], [117]–[119]. Figure 2.5 (a) shows the deposition geometry as an example for the use of combinatorial approach in the production of mixed ZnO-ITO thin films. The obtained samples are presented in Figure 2.5 (b). Here, in a single

experiment, a compositional gradient can be obtained among the thin film samples. This is realized by using a suitable deposition geometry. As it is obvious, these thin film samples look very different from each other. Thus, if high transmittance in the visible region is desired, only the first three compositions from the left provide this qualification. A similar evaluation can easily be carried out on each sample for electrical resistance, IR-reflectance, and thermal response so that the optimum composition can be easily specified for any specific application.

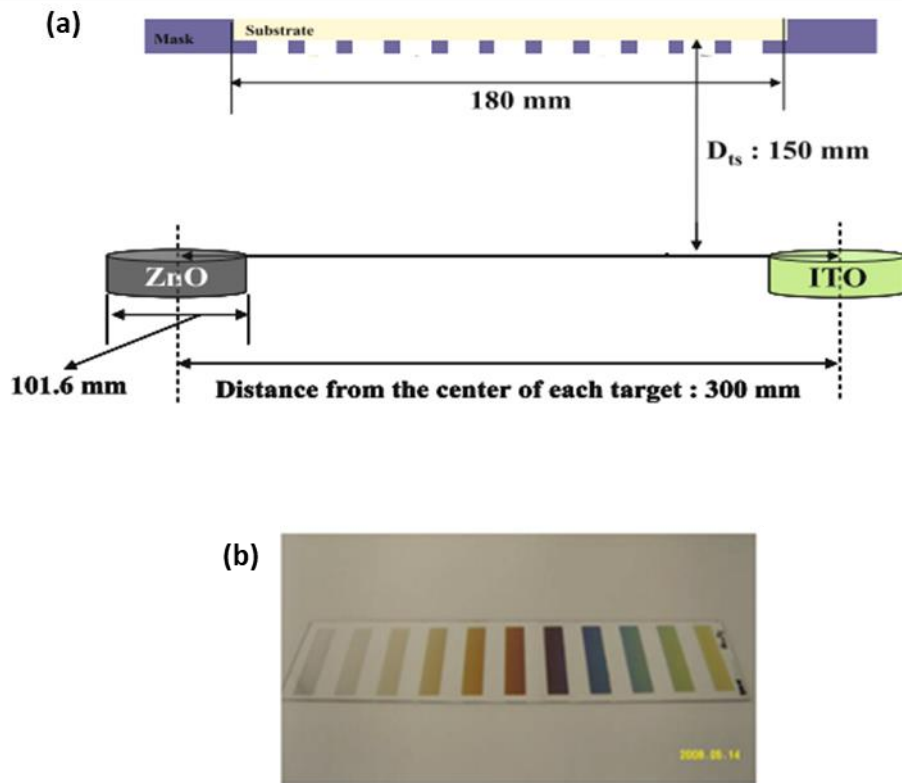


Figure 2.5 **a)** Schematic overview of the combinatorial deposition process, **b)** ZnO-ITO sample libraries obtained via using the deposition geometry given in (a) [117]

Figure 2.6 shows the compositional dependence of the structure (amorphous, crystalline, mixed) and electrical properties of the ZITO thin films obtained in another study which employed combinatorial approach [117]. Samples were deposited from two different targets on glass substrates at room temperature. As a result, thin films with atomic compositions of 17-57%  $\text{Zn}/(\text{Zn}+\text{In}+\text{Sn})$  are formed in

an amorphous structure. Throughout the range of amorphous composition, the electrical resistance exhibited almost a constant value. Here again, one of the remarkable points regarding the electrical resistance is that the lowest resistance is obtained in the amorphous+crystalline and amorphous compositional ranges. In stating this finding, the purpose is not that the Zn-doped amorphous thin films have better conductivity than pure ITO, but relatively high conductivity values can be obtained in a-TCOs depending on the composition. This finding further shows that it is possible to achieve conductivity values close to pure ITO with 10 at.% Zn contribution which means a reduction of ~30 at.% In in the relevant composition. In addition, in terms of optical properties, all samples in this study showed an average of more than 80% transmittance in the visible region.

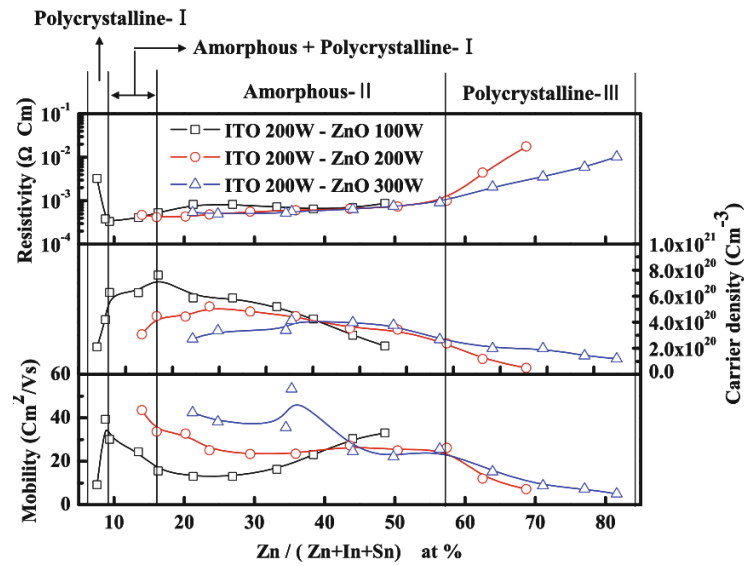


Figure 2.6 The change in the electrical resistance, carrier concentration, and mobility of ZITO thin films as a function of at. Zn % in the composition and RF power used in ZnO sputtering [117]

In a similar study, the lowest electrical resistance in ZITO thin films produced in amorphous structure by magnetron sputtering was reported as  $6.6 \times 10^{-4} \Omega \cdot \text{cm}$ , in the sample with 17% Zn atomic content. And the transmittance was 80% in the visible region [113]. It was also claimed that the films deposited, especially at low oxygen

partial pressures ( $P_{O_2}$ ), exhibited better electrical properties. Moreover, it was stated that the properties could be further improved by annealing in a reducing atmosphere after deposition. Deposition at low oxygen partial pressure increases the mobility of the charge carriers by increasing the number of oxygen vacancies; similarly, annealing in a reducing atmosphere contributes to the oxygen vacancy concentrations. These findings show that Zn-In-Sn-oxide thin films with amorphous structure can be used for the purpose of the current thesis study.

Amongst the others, the only similar deposition geometry to the geometry used in the current thesis study in terms of ZITO thin film deposition was employed by Ndione et al. (2016) [100]. In this study, amorphous ZITO thin films were obtained by using co-sputtering of  $In_2O_3$ , ZnO, and  $SnO_2$  targets [100]. Samples were deposited on  $5 \times 5 \text{ cm}^2$  substrates at room temperature. The target-to-substrate distance was 10 cm. 10 mTorr Ar was used as the sputtering gas for 20 to 30 min of deposition duration. RF power ranging between 20 to 65 W for  $In_2O_3$  and  $SnO_2$  targets and 100 W for ZnO targets were used. Films with amorphous structure have been produced with thicknesses ranging from 50 to 230 nm. Then the samples were electrically, optically, and mechanically characterized. Regardless of the composition, it was stated that all films formed in amorphous structure according to the XRD analysis and exhibited minimum 85% transmittance in the wavelength range of 400-800 nm. These finding clearly reveals that the composition does not have a dominant effect on the structure and optical properties. As a result of the examination of the mechanical properties, it was stated that the dependence of the elastic modulus on the composition was quite low, and the hardness increased with decreasing Sn amount. The obtained hardness and elastic modulus values implied that the amorphous ZITO is bendable enough to be employed in flexible devices. Moreover, since the hardness values are about twice to that of ITO and equal to or higher than that of glass, it has been stated that these thin films are stable in terms of wear resistance.

In contrast to the findings on other properties, the conductivity of a-ZITO thin films were found to be highly dependent on the composition of the film. For example, the



maximum conductivity value of  $2415 \text{ Scm}^{-1}$  was obtained for the film composition of  $\text{In}_{0.87}\text{Zn}_{0.07}\text{Sn}_{0.06}\text{O}_y$ . This composition corresponds to the range where the In/Zn ratio is 0.6-0.88, and the In/Sn ratio is 0.8-0.88. This conductivity value is comparable to crystalline ITO. The conductivity was changed from 702 to  $17 \text{ Scm}^{-1}$  for the films with compositions of  $\text{In}_{0.52}\text{Zn}_{0.38}\text{Sn}_{0.15}\text{O}_y$  and  $\text{In}_{0.08}\text{Zn}_{0.41}\text{Sn}_{0.51}\text{O}_y$ , respectively. These values clearly show the dependency of electrical conductivity on the constituent cations in the film composition.

The study further shown that the sputtering pressure has significant effect on the final conductivity of the films. The highest conductivity ( $2415 \text{ Scm}^{-1}$ ) was obtained under 10 mTorr Ar pressure, whereas for 20 mTorr Ar, it dropped to  $15 \text{ Scm}^{-1}$ . Similarly, the presence of oxygen in the chamber, i.e.,  $P_{\text{O}_2}$  of 0.1 % leads a reduced conductivity of  $145 \text{ Scm}^{-1}$ . Finally, the change in the conductivity of different compositions was attributed to change in the carrier concentration which means that the Hall mobility of the films were almost the same.

Within the scope of this study, the two aforementioned techniques for a-TCOs production were combined to achieve amorphous ZITO thin film heaters. First of all, the optimum composition was determined via the combinatorial approach. Then, a 3” sputtering target with this composition was produced by mixing and sintering the relevant oxide powders. And then, large-area samples were produced from this target and characterized in terms of structural, morphological, optical, electrical, and electrothermal properties.



## CHAPTER 3

### EXPERIMENTAL

In this section, the method and the parameters used in the production of AZO and a-ZITO thin films will be given. After that, the electrical and electrothermal property measurement systems established within the scope of this thesis will be introduced, and other general characterizations applied to the samples will be mentioned.

#### 3.1 Magnetron Sputtering of AZO/SiO<sub>2</sub> and a-ZITO thin films

All thin film samples in this study were produced using magnetron sputtering, which is also a suitable method for combinatorial approach. Figure 3.1 shows the thin-film deposition geometry used in the chamber. The substrate holder allows the use of a single circular substrate up to a diameter of 150 mm (magazine type multi-substrate carriers were used for this study), and the holder can be rotated at a speed of 30 rpm, if necessary. The system is equipped with four infrared lamps for substrate heating up to 300 °C.

The deposition process was started by placing the pre-cleaned substrates on the substrate holder; then, the vacuum pump was started. If the deposition condition requires the heating of the substrates to any temperature above RT, then the infrared lamps were turned on. When the chamber reached a vacuum level of  $1 \times 10^{-6}$  Torr, high purity argon gas was sent to the chamber with a flow rate of 20 sccm. Prior to deposition, each of the existing shutters on the sputtering targets were opened, and the pre-sputtering process was carried out for 10 min to clean the targets surfaces. During this process, the main shutter under the substrate holder was kept closed, thus preventing contamination of the samples. Afterwards, thin films were deposited until the desired film thickness was achieved. The thickness was monitored with a QCM, and when the desired thickness was achieved, the main shutter was closed, and the

sputtering process was terminated. The heated samples were always cooled down to room temperature in the vacuum environment.

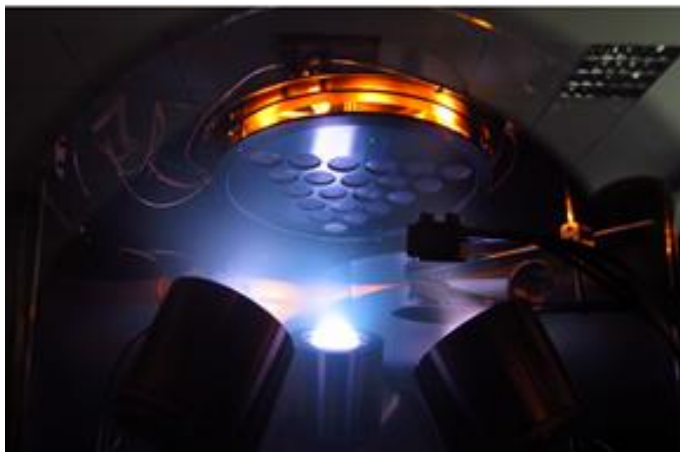


Figure 3.1 Thin-film deposition geometry used for the sample production

In this study, SiO<sub>2</sub>-capped AZO and a-ZITO thin films were produced by employing two different types of multi-substrate carrier magazine. The digital images of these carrier magazines can be seen in Figure 3.2 (a and b), which are used in the depositions of AZO/SiO<sub>2</sub> and a-ZITO thin films, respectively. AZO thin films were produced using a 2", 2 wt.% Al<sub>2</sub>O<sub>3</sub>-doped ZnO (99.99%, Kurt J. Lesker Co.) target. The position of the target and the deposition geometry can be followed from Figure 3.2 (c). The films were collected on glass substrates. In order to optimize the deposition parameters, AZO thin films were first deposited on 0.17 mm thick, 18 mm diameter glass substrates which arranged on the substrate carrier as given in Figure 3.2 (a). On the other hand, commercial soda-lime glass substrates with 5.0 cm x 7.5 cm dimensions and 3 mm thickness were used for the films tested in de-icing experiments. All substrates were cleaned with alkaline detergent, ethanol (99.5%, J.T. Baker) and deionized (DI) water for 10 minutes, respectively, in an ultrasonic bath and dried with a hot air gun before deposition. In the optimization process, substrate temperatures of RT, 100, 200, and 300 °C were used. The depositions were carried out under sputtering gas pressure of 3 mTorr Ar, 1.2 Å/s deposition rate, and

100 W RF power. In addition, films with 4 different thicknesses (250, 500, 750 and 1000 nm) were obtained to determine the optimum thickness to achieve optimal electrical and optical properties.

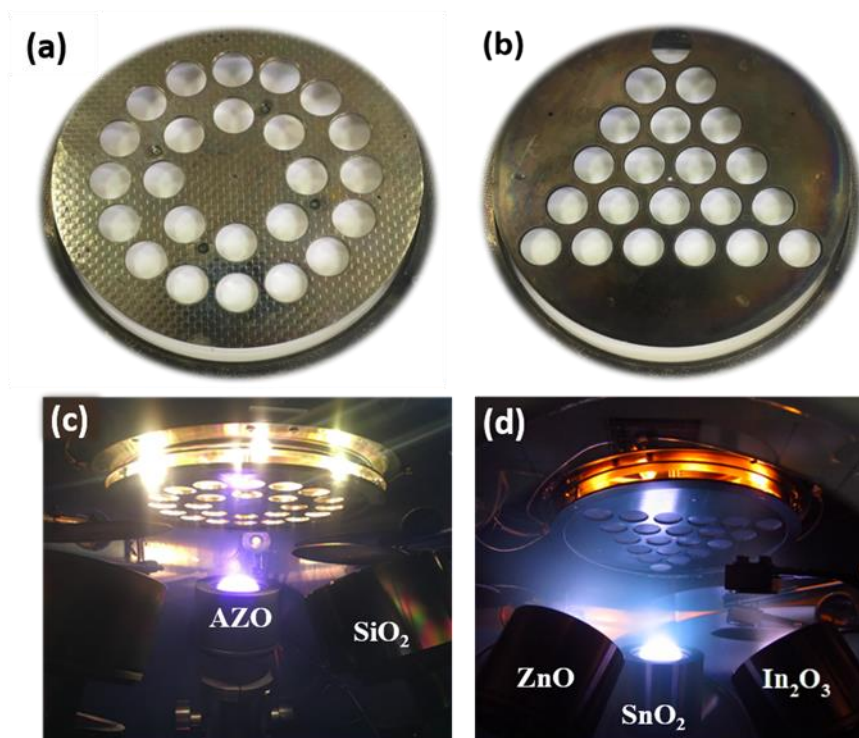


Figure 3.2 Multi-substrate carrier magazines employed in the deposition of **a)** AZO/SiO<sub>2</sub>, **b)** a-ZITO, and deposition geometries for **c)** AZO/SiO<sub>2</sub>, **d)** a-ZITO thin films. (Substrates were rotated at 8 rpm during AZO/SiO<sub>2</sub> thin film deposition)

In order to form the thin SiO<sub>2</sub> capping layer on the AZO thin films, a 2" diameter SiO<sub>2</sub> (Kurt J. Lesker Co.) target with 99.995% purity was used. This target was installed to one of the remaining two guns in the chamber, as seen in Figure 3.2. SiO<sub>2</sub> capping layer deposition process was carried out at room temperature using 75 W RF power.

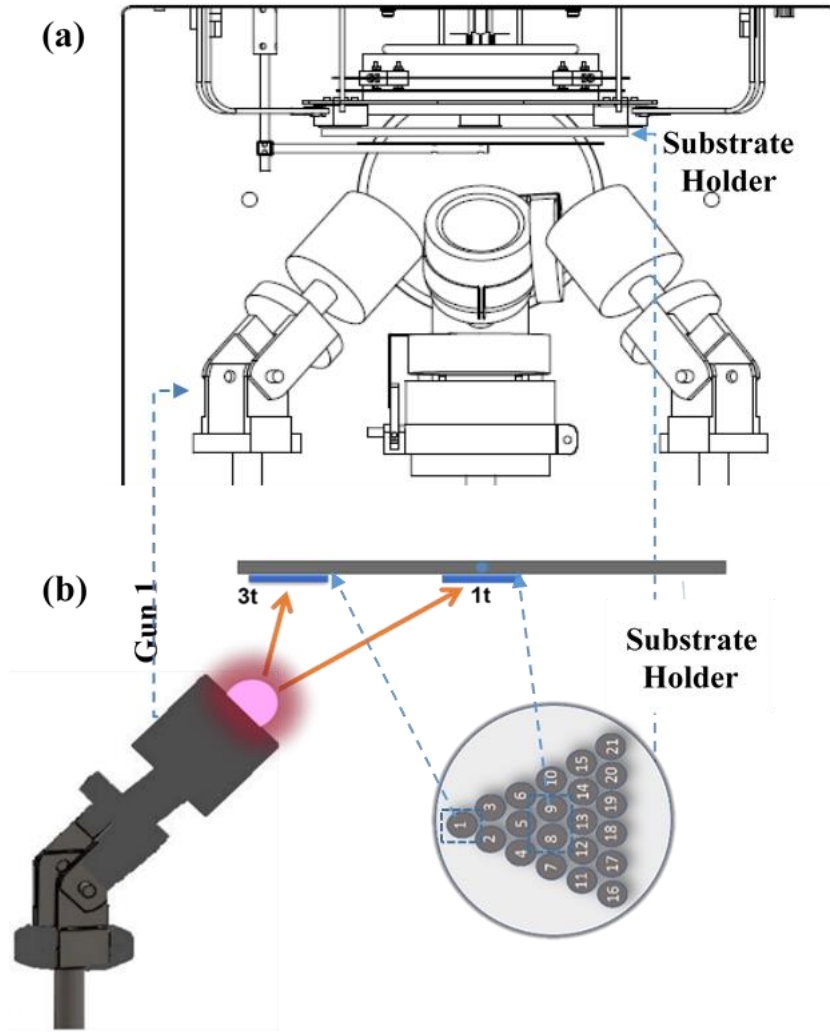


Figure 3.3 **a)** Schematic drawing of the arrangement of the components in the vacuum chamber, **b)** Schematic drawing of the deposition geometry used during the optimization step of a-ZITO thin-film production via combinatorial approach (t: the thickness of the depositing film)

a-ZITO thin films were obtained from a 3" and single composition target following an optimization step performed with 2" diameter  $\text{SnO}_2$  (99.99%),  $\text{ZnO}$  (99.99%), and  $\text{In}_2\text{O}_3$  (99.99%) (Kurt J. Lesker Co.) targets. The layout of these targets in the chamber can be seen in Figure 3.2 (d). Similar to the approach used during AZO thin film deposition, optimization of a-ZITO deposition was performed on 18 mm diameter glass substrates and a triangular type of substrate carrier magazine (see

Figure 3.3 (b)). The first set of experiments was carried out to determine optimal parameters such as sputtering powers, sputtering gun positions, and thickness-time relationships for each target. For this purpose, first, all corners of the triangular arrangement on the magazine were aligned with one of the oxide targets, as demonstrated in Figure 3.3 (a). Successive depositions (30 min each) were conducted systematically by shifting the position of the sputtering gun head on the y-axis and its angle on the z-axis. The focus of this trial-and-error depositions was to obtain a film thickness of “3t” on the corner sample, while a film thickness of “t” on the central sample as presented in Figure 3.3 (b). During the process, the thicknesses of the samples were determined by SEM measurements after each run. This approach was applied respectively for all three targets. After completing the positioning/aligning of each gun, deposition experiments were performed using a variety of sputtering powers. During these experiments, thicknesses of ~600 nm for the sample in the corner and ~200 nm for the sample in the center were monitored. The results are summarized in Table 3.1.

Table 3.1 The achieved film thicknesses after 30 min of depositions with samples #1 (corner) and #8/9 (center) as a function of sputtering power

<b>Gun 1 - SnO<sub>2</sub></b>		<b>Gun 2 - ZnO</b>		<b>Gun 3 - In<sub>2</sub>O<sub>3</sub></b>	
<b>Sample 1</b>	<b>Sample 8/9</b>	<b>Sample 1</b>	<b>Sample 8/9</b>	<b>Sample 1</b>	<b>Sample 8/9</b>
<b>80 W</b>		<b>110 W</b>		<b>85 W</b>	
1200 nm	350 nm	342 nm	95 nm	930 nm	315 nm
<b>40 W</b>		<b>130 W</b>		<b>100 W</b>	
728 nm	215 nm	410 nm	230 nm	~604 nm	~190 nm
<b>37 W</b>		<b>150 W</b>			
~608 nm	~188 nm	470 nm	260 nm		
<b>30 W</b>		<b>175 W</b>			
470 nm	150 nm	583 nm	~190 nm		

From now on, for Figure 3.1 and for the following sections, SnO<sub>2</sub>, ZnO, and In<sub>2</sub>O<sub>3</sub> targets are denoted as gun 1, gun 2, and gun 3, respectively. Following a similar labeling approach; sample 1 refers to the thin film sample which is nearest to the sputtering gun 1 (SnO<sub>2</sub> corner/gun 1), sample 16 refers to the sample which is nearest to the sputtering gun 2 (ZnO corner/gun 2), and sample 21 refers to the sample which is nearest to the sputtering gun 3 (In<sub>2</sub>O<sub>3</sub> corner/gun 3). Other sample numbers can be seen from Figure 3.3 (b). As seen from Table 3.1, the 3/1 ratio in terms of film thicknesses in the corner and the center were achieved by employing RF powers of 37 W for SnO<sub>2</sub>, 175 W for ZnO, and 100 W for In<sub>2</sub>O<sub>3</sub> deposition.

Finally, the thickness and compositional distribution on each 21 substrates were examined by co-deposition of SnO<sub>2</sub>, ZnO, and In<sub>2</sub>O<sub>3</sub> targets using these predetermined parameters. Two different sputtering pressures were applied during these experiments, i.e., 5 and 10 mTorr. Film depositions were carried out at room temperature for 15, 30, 45, and 60 minutes. Then, the obtained samples at each sputtering pressure and deposition duration were subjected to optical and electrical characterizations. Thus, the change in properties as a function of deposition parameters were determined. Finally, new sets of samples were produced under the determined optimum time and pressure values, and these thin films were subjected to structural, compositional, morphological, electrical, and optical characterization in both deposited and annealed states (see section 3.2).

After determining the optimal deposition parameters, the best composition among 21 samples which provided the optimum electrical and optical properties was transferred to a single target. This was achieved by mixing proper amounts of high purity SnO<sub>2</sub>, ZnO, and In<sub>2</sub>O<sub>3</sub> powders in appropriate proportions and sintering them into a 3" sputtering target. Then, a-ZITO thin films were produced on 5 cm x 7.5 cm glass substrates that were kept at RT, 150 °C, and 250 °C. The sputtering pressure, power, and deposition rate for each run were set to 3 mTorr, 100 W RF, and 2.2 Å/s, respectively.



### 3.2 Post-deposition annealing of thin films

Annealing processes were carried out following the deposition step in order to improve the electrical and optical properties of the thin films. In this step, different environments such as air, vacuum ( $1 \times 10^{-6}$  Torr), Oxygen (99.999%), Nitrogen ( $N_2$ ) (99.999%) or forming gas (Argon + 4%  $H_2$  by volume) were tested. In this way, the annealing medium that will provide the most superior properties has been determined. The sputtering system itself was used for annealing the samples under vacuum. On the other hand, an atmosphere-controlled furnace was used for annealing in other atmospheres. The annealing temperature was set to 300 °C or 400 °C., depending on the annealing atmosphere and capability of the heating equipments, i.e., vacuum chamber or furnace. Heating was carried out at a rate of 2 °C/min for all samples, and the existing atmospheric condition was maintained during natural cooling.

The annealing conditions used for the AZO thin films were as follows: vacuum ( $1 \times 10^{-6}$  Torr) at 300 °C, high purity Ar (99.999%) at 400 °C, and Ar + 4%  $H_2$  at 400 °C for 1 h. Similar to AZO thin film samples, annealing was carried out for a-ZITO thin films under different conditions. The a-ZITO samples produced at room temperature were annealed in air atmosphere at 400 °C, in Ar atmosphere at 300 °C and 400 °C, and in forming gas atmosphere at 400 °C for 1 h. In addition, these films were also annealed in such a way that the films were heated to 400 °C under Ar+4%  $H_2$  atmosphere, then the furnace atmosphere switched to pure Ar, and the samples were kept under this condition for 1 h. For a-ZITO samples produced at 250 °C, only Ar and Ar+4%  $H_2$  atmosphere annealings at 400 °C and 1 h were employed.

### 3.3 Characterization

The structural properties and phase distribution of the produced thin films were determined by X-ray diffraction (XRD) method. For this purpose, a Bruker D8 Advance diffractometer was used. XRD patterns were obtained using  $CuK\alpha$  radiation

with a wavelength of  $\lambda=1.5406 \text{ \AA}$  in Bragg-Brentano mode, and a step-size of  $0.02^\circ$  in the range of  $2\theta = 20\text{-}80^\circ$ . The Scherrer equation given below was used to calculate the crystallite sizes of AZO-based samples.

$$D = \frac{k\lambda}{\beta \cos \theta} \quad (3.1)$$

In this equation,  $D$ ,  $k$ ,  $\lambda$ ,  $\beta$  and  $\theta$  represents the crystallite size in the direction perpendicular to the corresponding lattice planes under consideration,  $k$  is the numerical factor (crystallite-shape factor and taken as 0.9),  $\lambda$  is the wavelength,  $\beta$  is the width (full width at half-maximum) of the XRD peak in radians, and  $\theta$  is the corresponding Bragg angle, respectively. The in-plane stress values developed during the film growth were calculated using the Equation (3.2) and the biaxial strain model [120].

$$\delta = \frac{((d - d_0)|d_0) \times [2c_{13}^2 - c_{33}(c_{11} + c_{12})]}{2c_{13}} \quad (3.2)$$

$c_{11}$ ,  $c_{12}$ ,  $c_{13}$ , and  $c_{33}$  in this equation are the elastic stiffness constants of crystalline ZnO and taken as 208.8, 119.7, 104.2, and 213.8 GPa, respectively [121]. The interplanar spacing value for (002) planes, which is denoted by “d” was calculated from XRD patterns and using the Bragg equation (Equation 3.3).

$$n\lambda = 2d\sin\theta \quad (3.3)$$

The  $d_o$  value in Equation 3.2 was taken as 5.206 Å for the (002) peak using the Joint Committee on Powder Diffraction Standards (JCPDS) Card No: 36-1451 which belongs to ZnO. In determining the lattice parameters, (Equation 3.4) was used.

$$\frac{1}{d^2} = \frac{4}{3} \left[ \frac{(h^2 + hk + k^2)}{a^2} \right] + \frac{l^2}{c^2} \quad (3.4)$$

In this equation,  $h$ ,  $k$ , and  $l$  are the miller indices of the relevant plane, and  $a$  and  $c$  are the lattice parameters in hexagonal crystals.

In the morphological examination of the the films, FEI Nova NanoSem 430 model field emission scanning electron microscope (FE-SEM) and Veeco Multi-Mode V model atomic force microscope (AFM) were used. The 3D surface topography of the samples was extracted from the AFM measurements which were conducted in non-contact mode. In determining the surface roughness values, scans were made in an area of 2 µm x 2 µm. Film thicknesses and average grain sizes were determined using SEM, AFM and *Image J* software. Energy-dispersive X-ray spectroscopy (EDX) was used to determine the elemental distribution and atomic ratios of the elements present in the films.

VWR 3100-PC model UV-Vis (ultraviolet-visible) spectrophotometer was used to determine the visible light transmittance of thin film samples. Spectra were obtained in the wavelength range of 300-1000 nm. In calculating the average light transmittance ( $T_{vis}$ ) values, the average light transmittance of the sample in the wavelength range of 400-700 nm was used. On the other hand, absorbance and reflectance values were determined by Cary 5000 model ultraviolet-visible-infrared (UV-Vis-NIR) spectrophotometer.

To calculate the band energies ( $E_g$ ) of the films, visible region transmittance, equation (3.5), and Tauc plots were used [122].

$$(\alpha hv)^2 = A(hv - E_g)^{1/2} \quad (3.5)$$

In this equation,  $A$ ,  $\alpha$ ,  $hv$ , and  $E_g$  represent a constant, absorption coefficient, photon energy, and optical bandgap energy for direct transitions, respectively. The  $E_g$  value is obtained by intersecting the tangent line from the linear portion of the  $(\alpha hv)^2$ - $hv$  curve with the x-axis.

The electrical properties of the thin films were examined in Van der Pauw configuration, either using a Nanomagnetic Instruments ezHEMS model Hall-effect measurement system or a custom-made four-point probe electrical measurement setup. In the four-probe measurement, the probes are collinear and the distance between the probes are equal. During the measurement, the current flows through the outer probes and the voltage values are recorded across the two inner probes. The general view of the latter system is given in Figure 3.4. The setup consists of a 60 V DC power supply (Tektronix PWS4602, left), a probe station, and an LCR meter (inductance, capacitance, and resistance measurement system, Hioki IM 3536, right), Figure 3.4 (a). The probe station can perform measurements on thin film samples up to substrate size of 15x15 cm<sup>2</sup>, Figure 3.4 (b). In determining the sheet resistance ( $R_s$ ,  $\Omega/\square$ ), the values of  $R_{12.34}$ ,  $R_{23.41}$ ,  $R_{34.12}$ ,  $R_{41.23}$  were recorded under 5 mA constant current, and an average value for  $R_s$  of each film was obtained by placing the corresponding values in Equation (3.6).

$$R_s = \frac{\pi}{\ln(2)} x \left( \frac{V}{I} \right)_{avg} \quad (3.6)$$

The  $(V/I)_{avg}$  value in this equation refers to the average of  $R_{12.34}$ ,  $R_{23.41}$ ,  $R_{34.12}$ ,  $R_{41.23}$ , that is the average of four different resistance values measured for each film.

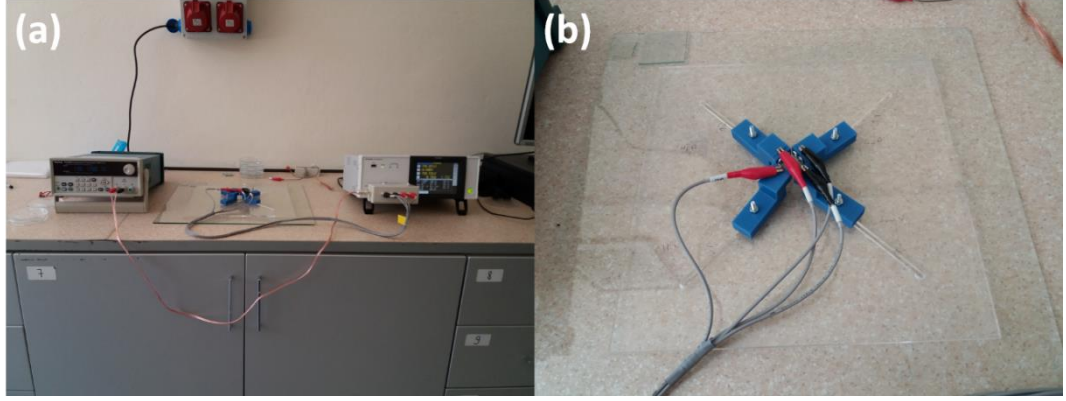


Figure 3.4 **a)** General view of the system used in the electrical property measurements of the thin films, **b)** a closer view of the probe station of the system in Van der Pauw geometry

The performance criterion (figure of merit, FOM, ( $\phi_{TC}$ )) of the deposited films were determined by the Haacke equation given below.

$$\phi_{TC} = T_{550\text{ nm}}^{10}/R_s \quad (3.7)$$

In this equation,  $T_{550}$  is the transmittance at 550 nm wavelength, and  $R_s$  ( $\Omega/\square$ ) is the sheet resistance of the corresponding thin film sample.

Transparent heater characteristics of the thin films produced within the scope of this thesis study were determined using a custom-made measurement setup presented in Figure 3.5 (a). The setup consists of an infrared camera (Optris Xi 400), a computer used for temperature recording and image processing, and a 60 V DC power supply (Tektronix PWS4602 model) used to apply voltage to the samples. The sample holder is shown in Figure 3.5 (b). The electrical connection between the power source and the film is provided by duck mouth Cu crocodiles and Ag electrodes applied to the film surface. The distance between the film surface and the camera was set to 55 cm.

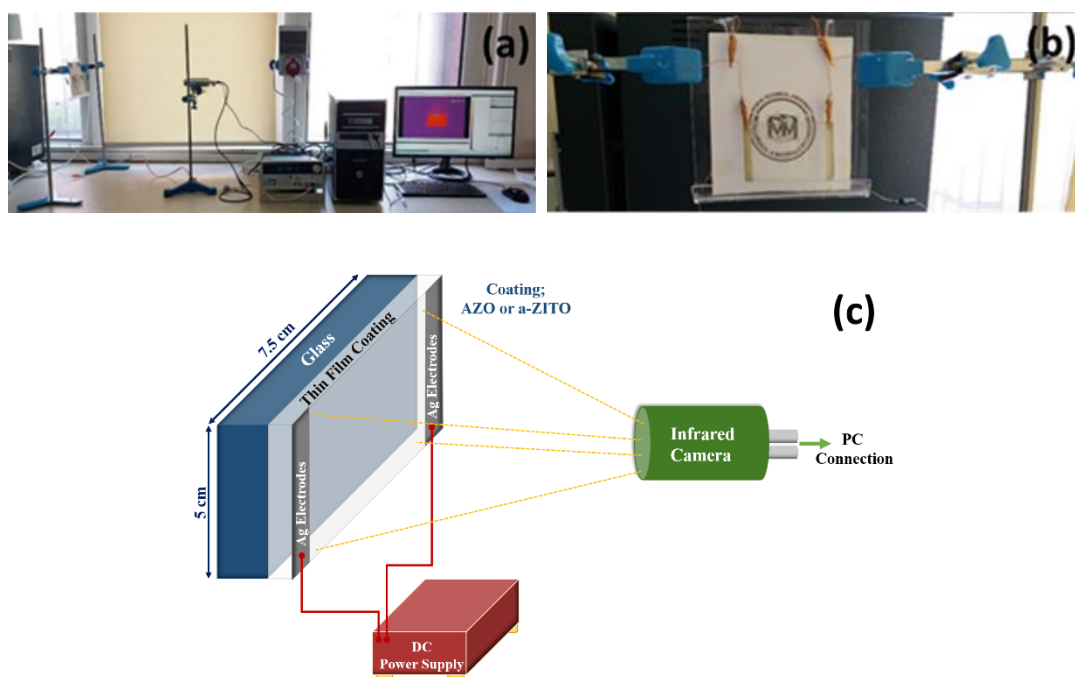


Figure 3.5 **a)** General view of the system used for electrothermal measurements, **b)** sample, **c)** schematic drawing of the system

Samples were evaluated using two different initial conditions. To determine the response time, saturation surface temperature, stability, recyclability, and thermal resistance as a function of applied voltage, all samples were subjected to various constant voltages (0-18 V) at ambient temperature. On the other hand, deicing tests were performed after cooling the samples to low temperatures for 1 h in a thermally insulated dry-ice-filled box. The deicing performance of the heaters was revealed for input voltages of 3, 6, 9, and 12 V, starting from  $-40\text{ }^{\circ}\text{C}$  sample temperature.

The response time was assumed as the required time to reach 90% of the value of surface saturation temperature for the heater under an applied constant voltage. The stability test was performed by monitoring the surface temperature of the sample for a relatively long period (e.g., 3600 s) under a certain constant voltage loading. This was used to evaluate the changes in the surface temperature over time. Equation 3.8 was employed in the determination of the surface temperature homogeneity ( $T_U$ ) of the heaters [123].

$$T_u(\%) = \left[ \frac{(T_H - T_L)}{2 T_{avg}} \right] \times 100 \quad (3.8)$$

$T_H$ ,  $T_L$ , and  $T_{vis}$  values were recorded from the surfaces of the samples during the stability measurements. As mentioned before, the sample surface temperature was recorded by an infrared camera, and if necessary, this record can be processed at any time by the camera's software. Therefore, the symbols given above represent the maximum, minimum, and average temperatures ( $^{\circ}\text{C}$ ), respectively, detected at different points on the surface of the sample with this software. Maximum and minimum temperatures were determined in the 1 mm x 1 mm measuring area, while the entire active area of the heater was used to determine the average temperature.

For cyclic electrothermal behavior, samples were examined at switching voltages of 0 and 12 V. During the measurements, the heater was first subjected to 12 V at  $25^{\circ}\text{C}$ , and then the power was turned off when the IR camera confirmed a mean surface temperature of  $100^{\circ}\text{C}$ . Then the heater was left to cool naturally to  $25^{\circ}\text{C}$  before the application of 12 V for the next heating cycle. This procedure was repeated for 25 heating/cooling cycles.

Thermal resistance and thermal resistivity are two distinct heat properties that generally confused to each other. The former is a temperature difference measurement by which a material resists to heat flow. On the other hand, the latter expresses the thermal resistance of a material per unit area and has the unit of  $\text{m}^2\text{K/W}$ . A transparent heater should exhibit a high thermal resistance value as a function of the applied electrical power. The thermal resistance of the heaters was calculated from the slope of the linear relationship between the input power vs. saturation temperature. Here, the surface saturation temperature was determined for each applied voltage value and plotted against the respective areal power densities (total electrical power/total active area). Since the relationship between them is linear, the thermal resistance of the samples was obtained from  $dT/dP$  [10].

Prior to deicing experiments, the dry-ice cooled samples were installed on the sample holder. When the IR camera indicated a mean surface temperature of -40 °C, the samples were loaded with a constant input voltage. This test was repeated under different constant voltage values (i.e., 6, 9, and 12 V), and the de-icing capacity of the samples was determined as a function of time. This time refers to the total time required for melting of all ice and evaporation of all water-based droplets from the heater surface. The evaporation of water from the surface was followed by the naked eye, and the thermal camera was used to record the temperature change on the surface during this process.

The areal power density of the heaters can be determined simply by using the basic electrical formula  $P/A$ . Here,  $A$  is the active surface area of the heater (the area between the Ag-electrodes), and  $P$  is the electrical power, and it can be deduced from the formula  $P=I^2R$  using the current ( $I$ ) passing through the sample and the resistance ( $R$ ) of the film. While the current is obtained by monitoring the value directly from the power source, the  $R=\rho(L/W_e d_k)$  equation was used to calculate the resistance of the samples. In this equation,  $\rho$  ( $\Omega\text{cm}$ ) represents the resistivity of the film and was calculated by multiplying the thickness ( $d_k$ ) of the film in “cm” with the measured sheet resistance. The film thicknesses were obtained from SEM examinations.  $L$  and  $W_e$  are the length of the heater and the distance between the two silver electrodes, respectively, both in “cm”.



## **CHAPTER 4**

### **RESULTS AND DISCUSSION**

In this thesis study, AZO/SiO<sub>2</sub> as an In-free composition and ZITO thin films with reduced In content were produced for transparent heater and heat reflecting applications. A series of optimization steps were carried out prior to production of the final thin film samples. Thus, initial sections of this chapter are devoted to the deposition optimization of AZO thin films. Then, in the following sections the results obtained on AZO/SiO<sub>2</sub> thin film heaters are presented.

#### **4.1 Optimization of Production of AZO Thin Films on Glass Substrates by Magnetron Sputter Deposition**

##### **4.1.1 Thickness optimization**

To identify the optimal layer thickness, AZO thin films with thicknesses of 250, 500, 750, and 1000 nm were deposited on glass substrates kept at RT. Structural, morphological, optical, and electrical properties of these samples were examined both in the deposited and annealed states. Figure 4.1 shows the XRD patterns of these films. In all cases, the films developed a crystalline structure and showed preferred orientation along the c-axis. Different from others, (100) and (101) peaks were appeared in the pattern of 1000 nm thick sample. Further, the intensity of (002) and (004) diffraction peaks increased with increasing film thickness. For all patterns, the peaks were indexed well with the hexagonal ZnO wurtzite crystal structure in accordance with the JCPDS Card No. 36–1451. No diffraction peaks corresponding to any metallic or oxide impurities other than AZO could be detected in the patterns.

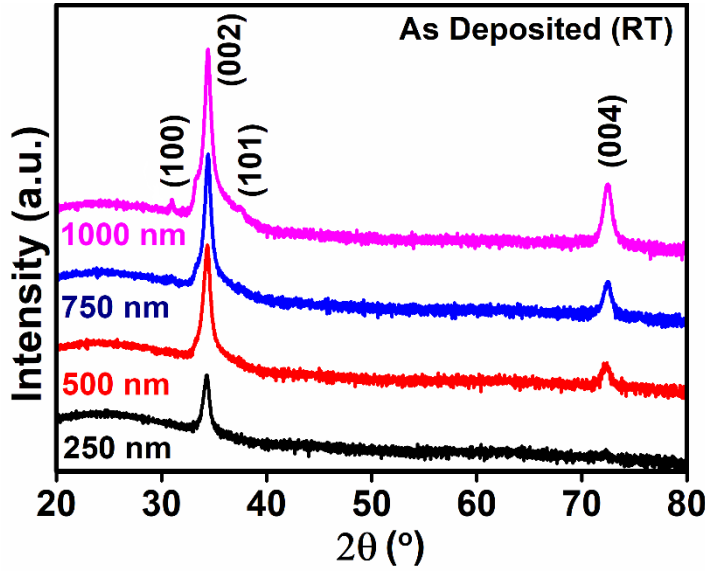


Figure 4.1 XRD patterns of AZO thin films deposited at RT and thicknesses of 250, 500, 750, and 1000 nm

Table 4.1 presents the thickness-dependent structural changes for RT deposited AZO thin films. The data of bulk ZnO are also given for comparison. The recorded  $2\theta$  value for the (002) plane at each film thickness shows a shift to lower angles compared to standard bulk ZnO. The substitution of smaller  $\text{Al}^{3+}$  (0.53 Å) ions with larger  $\text{Zn}^{2+}$  (0.74 Å) is expected to induce a contraction in the lattice. However, the  $c$ -parameter of the films decreased with the increasing film thickness. A value of 5.207 Å was calculated for 1000 nm thick film, which is equal to the  $c$ -parameter value of standard bulk ZnO. At first glance, this seems to indicate that the highest amount of  $\text{Al}^{3+}$  substitution into Zn-sites occurs for 1000 nm thick film. On the other hand, it should be noted that the large structural mismatch between the amorphous glass substrate and crystalline thin film develops significant in-plane stress in AZO layer [124]. The corresponding values of the residual stress are also listed in this table. As evident from the negative values, the stresses are all compressive. The highest stress was calculated for the film with 250 nm thickness, and the stress decreased with increasing film thickness. It is therefore clear that the observed shift in the peak positions for the films with different thicknesses both depends on the

developed stress and incorporation of Al ions into ZnO lattice and the competition between the effect of these two phenomena on lattice parameter. The crystallite sizes of the samples as a function of thin film thickness is also demonstrated in Table 4.1. It was observed that the crystallite size increased from 23 to 33 nm depending on the film thickness. This reveals that the crystal quality of the films is increasing with thickness.

Table 4.1 Thickness dependent structural properties of AZO thin films deposited at RT with various thicknesses

<b>Thickness (nm)</b>	<b><math>2\theta_{(002)}</math> (°)</b>	<b><math>2\theta_{(100)}</math> (°)</b>	<b><math>a</math> (Å)</b>	<b><math>c</math> (Å)</b>	<b><math>\delta</math> (GPa)</b>	<b>Crystallite Size (nm)</b>
<b>250</b>	34.29	-	-	5.227	-0.89	23
<b>500</b>	34.36	-	-	5.217	-0.47	24
<b>750</b>	34.41	-	-	5.210	-0.13	29
<b>1000</b>	34.42	31.76	3.25	5.207	0	33
<b>Standard ZnO</b>	34.42	31.76	3.25	5.207	-	-

Figure 4.2 (a-d) demonstrates the FE-SEM surface images of AZO thin films deposited at RT with four different thicknesses. As can be seen from these pictures, the films exhibit a hillock appearance, which is quite common in sputter-deposited AZO thin films. Among the obtained thicknesses, 750 nm thick film both has a spherical-like grain structure and exhibits a less rough surface.

Figure 4.3 (a-d) depicts the cross-sectional FE-SEM images of AZO thin films produced at RT with four different thicknesses. As seen from these micrographs, AZO thin films could be obtained almost with intended thickness due to optimized deposition conditions. In addition, one can see the formation of the columnar grains with preferred orientation. Further, these images reveal that the films were deposited in a high-density structure and were free from intergranular porosity.

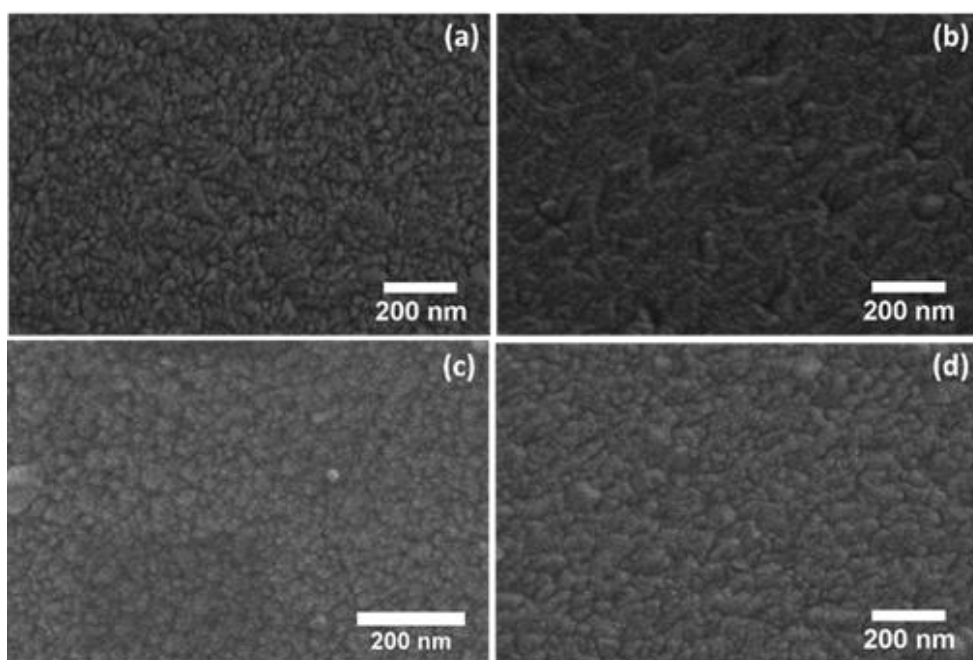


Figure 4.2 Surface SEM images of AZO thin films deposited at RT with various thicknesses; **a)** 250 nm, **b)** 500 nm, **c)** 750 nm, **d)** 1000 nm

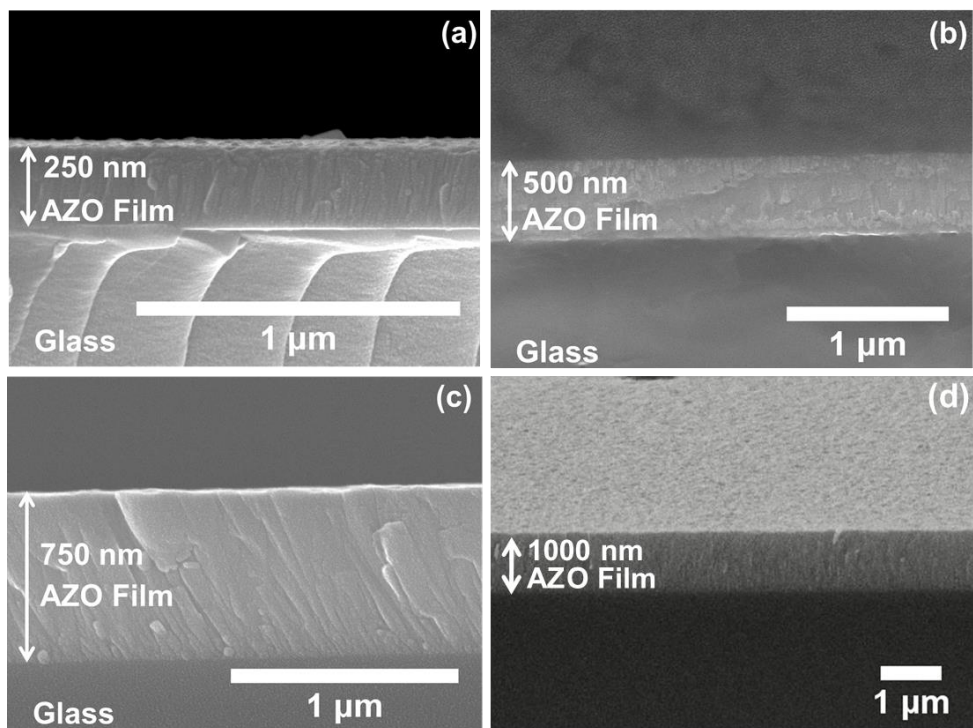


Figure 4.3 Cross-sectional SEM images of AZO thin films deposited at RT with various thicknesses; **a)** 250 nm, **b)** 500 nm, **c)** 750 nm, **d)** 1000 nm

The optical properties of RT deposited AZO thin films with various thicknesses were investigated with UV–Vis spectrophotometer. Figure 4.4 gives the transmittance spectra of these films in the wavelength range of 300 to 1000 nm. As expected, the average transmittance ( $T_{vis}$  @ 400–700 nm) in the visible region is highly dependent on thickness [125]. The  $T_{vis}$  values were calculated as 91%, 88%, 74%, and 71% for the films with 250, 500, 750, and 1000 nm thicknesses, respectively. In addition, the absorption edge at a wavelength of 340 nm for 250 nm thick film increased to 365 nm for the film with 1000 nm thickness, which reveals that transmittance in the UV region decreased. As shown as an inset in Figure 4.4, the  $E_g$  values of AZO thin films decrease from 3.65 to 3.39 eV as the film thickness increases, i.e., a red shift occurs with increasing layer thickness. This is probably due to the difference in charge carrier concentration, increasing crystallinity, and reduction of the residual stress in the films with greater thickness.

It has also been observed that the oscillatory character of the transmittance spectra of as-deposited AZO thin films varies depending on the film thickness. The interference fringe patterns arise due to multiple reflections at the interfaces (front and back interfaces) of the film and the frequency and depth of the reflectance are controlled by the film thickness and optical constants. Similar to previous studies, it is seen that the number of interference fringes increases as the thickness of the as-deposited AZO thin film increases [126], [127]. Furthermore, the presence of interference fringe pattern in the transmittance curve is generally attributed to the smoothness of the film surfaces, which is desired for transparent heater applications [128].

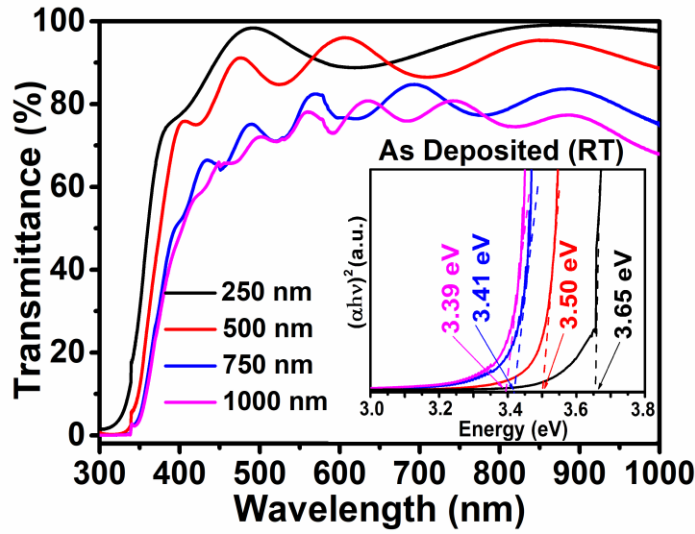


Figure 4.4 Transmittance spectra of AZO thin films deposited at RT with various thicknesses (The inset shows the estimated direct band gap energy of the films)

Figure 4.5 demonstrates the electrical properties of RT deposited AZO thin films as a function of film thickness. The  $R_s$  values of the films were measured as  $204.31 (\pm 0.204)$ ,  $57.81 (\pm 0.007)$ ,  $25.63 (\pm 0.004)$ , and  $12.96 (\pm 0.011) \Omega/\square$  for the films with 250, 500, 750 and 1000 nm thickness, respectively. This means that the  $R_s$  value is decreased by about one order of magnitude when the film thickness is increased from 250 to 1000 nm. In the same order, the resistivity values of the films were determined as  $5.11 (\pm 2.03 \times 10^{-6}) \times 10^{-3}$ ,  $2.87 (\pm 1.12 \times 10^{-6}) \times 10^{-3}$ ,  $1.92 (\pm 1.03 \times 10^{-6}) \times 10^{-3}$ , and  $1.29 (\pm 1.25 \times 10^{-6}) \times 10^{-3} \Omega \cdot \text{cm}$ , respectively, indicating a decrease in electrical resistivity. These findings imply that there is a trade-off between the electrical and optical properties since the thicker the film the higher the conductivity, but also the lower the transparency. This also dictates a limiting thickness for RT deposited AZO thin films, as the heater needs to be sufficiently transparent.

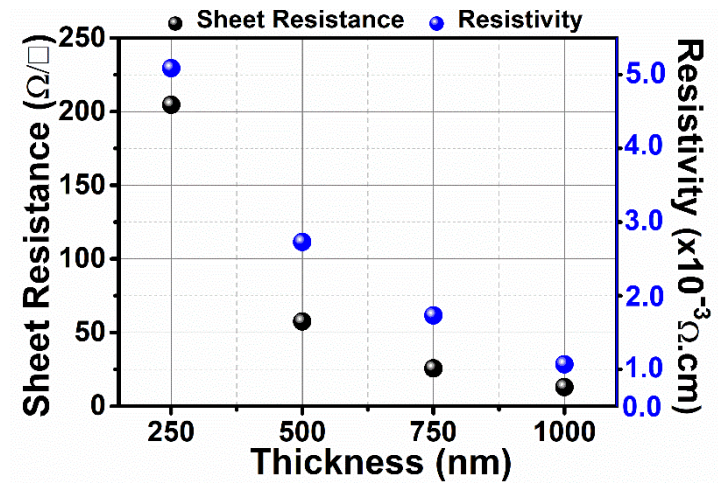


Figure 4.5 Electrical properties of AZO thin films deposited at RT with various thicknesses

#### 4.1.2 Annealing optimization

RT deposited AZO thin films with different thicknesses were annealed in various atmospheres to determine the changes in their optical and electrical properties. Figure 4.6 (a-c) presents the transmittance spectra of AZO thin films (RT deposited, 250–1000 nm) after annealing for 1 h under vacuum (300 °C,  $1 \times 10^{-6}$  Torr), high purity Ar (400 °C, 99.999%), and Ar + 4% H<sub>2</sub> (400 °C), respectively. It is seen that the optical properties of RT deposited AZO thin films vary depending on the film thickness and annealing condition. The corresponding Tauc plots are given as insets. The numerical values for each condition can be followed from Table 4.2.

As seen from these figures and the listed values in Table 4.2., independent of the annealing condition employed, the  $T_{vis}$  values of the films were decreasing as the film thickness increasing. This can be attributed to the increase in the amount of scattering, reflection, and optical absorption on the film surface with increasing thickness. In addition, the losses also increase with the increasing of volume which is interacting with the light [125]. It is seen that annealing process does not affect the  $T_{vis}$  value of thinner films (e.g. 250 nm) but changes it significantly for the thicker films such as 750 and 1000 nm.

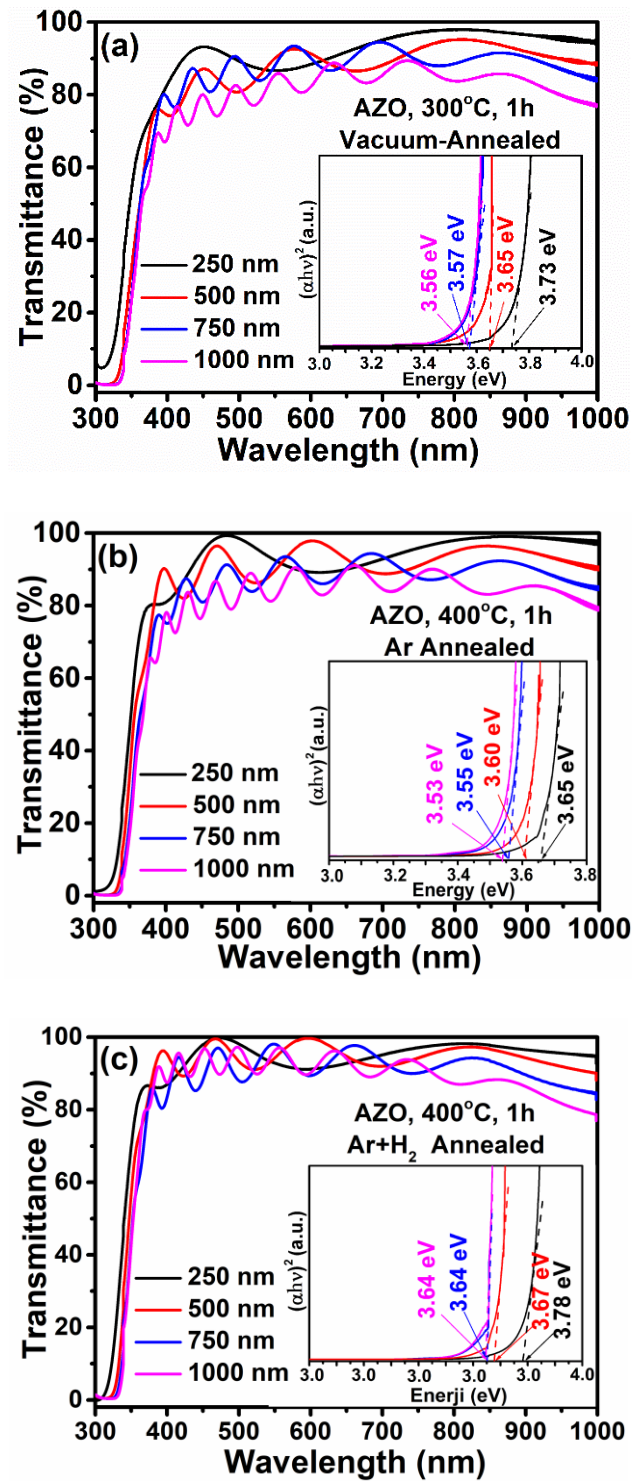


Figure 4.6 Transmittance spectra of AZO thin films (RT, 250–1000 nm) after annealing under various atmospheres for 1 h; **a)** vacuum, 300 °C, **b)** Ar, 400 °C, **c)** Ar + 4% H<sub>2</sub>, 400 °C (The insets show the estimated direct band gaps of the films for each condition)



Annealing under vacuum or Ar atmospheres yielded similar transmittance values although the annealing was performed at different temperatures, i.e., 300 °C for vacuum and 400 °C for Ar. Forming gas annealing, on the other hand, substantially improved the optical behavior of the samples. As seen from Table 4.2, the  $T_{avg}$  values of the films were measured as 96 ( $\pm 3.07$ ), 95 ( $\pm 3.13$ ), 93 ( $\pm 3.63$ ), and 93 ( $\pm 2.16$ ) % for the films with 250, 500, 750, and 1000 nm thickness, respectively after forming gas annealing. Similar observations were also reported in previous studies and this improvement is attributed to decreased defect concentration at grain boundaries with better crystallization of the films in the presence of H<sub>2</sub> [94]. Further, annealing induced a blue-shift in the absorption edge of the films compared to their as-deposited state. The highest shift was obtained in case of Ar + 4% H<sub>2</sub> annealing. This shift can be ascribed to Burstein-Moss effect [129], [130] and decrease in electron trapping sites on the surface as a result of oxygen desorption [131]. Accordingly, post-annealing deposition was increased the  $E_g$  of the films whereas the highest values were obtained again in case of forming gas annealing, Table 4.2.

Table 4.2 Optical properties depending on thickness and annealing condition in RT deposited AZO thin films

Thickness (nm)	As-deposited RT		Argon, 400 °C, 1 h		Vacuum, 300 °C, 1 h		Ar+4% H <sub>2</sub> , 400 °C, 1 h	
	$E_g$ (eV)	$T_{vis}$ (%)	$E_g$ (eV)	$T_{vis}$ (%)	$E_g$ (eV)	$T_{vis}$ (%)	$E_g$ (eV)	$T_{vis}$ (%)
<b>250</b>	3.65	91	3.65	92	3.73	90	3.78	96
<b>500</b>	3.50	88	3.60	91	3.65	86	3.67	95
<b>750</b>	3.41	74	3.55	88	3.57	88	3.64	93
<b>1000</b>	3.39	71	3.53	85	3.56	81	3.64	93

The electrical properties of RT deposited AZO thin films vary depending on the film thickness and annealing condition.

Table 4.3 Electrical properties depending on thickness and annealing condition in RT deposited AZO thin films

Thickness (nm)	As-deposited RT		Argon, 400 °C, 1 h		Vacuum, 300 °C, 1 h		Ar+ 4% H <sub>2</sub> , 400 °C, 1 h	
	$R_s$ ( $\Omega/\square$ )	$\rho \cdot 10^{-4}$ ( $\Omega \cdot \text{cm}$ )	$R_s$ ( $\Omega/\square$ )	$\rho \cdot 10^{-4}$ ( $\Omega \cdot \text{cm}$ )	$R_s$ ( $\Omega/\square$ )	$\rho \cdot 10^{-4}$ ( $\Omega \cdot \text{cm}$ )	$R_s$ ( $\Omega/\square$ )	$\rho \cdot 10^{-4}$ ( $\Omega \cdot \text{cm}$ )
<b>250</b>	204.68	51.17	83.75	20.93	71.21	17.8	38.84	9.7
<b>500</b>	57.81	28.77	30.44	15.22	33.27	16.63	23.49	11.74
<b>750</b>	25.63	19.22	16.89	12.67	15.45	11.58	11.06	8.29
<b>1000</b>	12.96	12.96	8.68	8.68	7.35	7.35	7.45	7.45

Table 4.3 shows that the sheet resistance and resistivity values of the films measured after annealing for 1 h under vacuum at 300 °C, under high purity Ar at 400 °C, and under Ar+4% H<sub>2</sub> atmospheres. It is clear from the obtained  $R_s$  values that annealing improves the electrical conductivity of AZO thin films in comparison to as-deposited state and independent from the atmosphere used during the process. On the other hand, depending on the annealing environment used, the best results were obtained after annealing under Ar + 4% H<sub>2</sub> atmosphere. Particularly, for films with 750 nm (11.06 ( $\pm$  0.013)  $\Omega/\square$ ) and 1000 nm (7.45( $\pm$  0.036)  $\Omega/\square$ ) thickness, the  $R_s$  values are approaching the  $R_s$  values of commercially available ITO thin films (8–12  $\Omega/\square$ ). The corresponding resistivity values for these films were recorded as 8.29 ( $\pm$  1.03x10<sup>-6</sup>) x10<sup>-4</sup> and 7.43 ( $\pm$  3.66x10<sup>-6</sup>) x10<sup>-4</sup>  $\Omega \cdot \text{cm}$ , respectively.

The increase of electrical conductivity in AZO thin films after annealing is well documented in literature and generally attributed to decrease in grain boundary scattering, increase in the number of oxygen vacancies, carrier concentration, and Hall mobility of the carriers, formation of metallic Zn and substitutional hydrogen impurities, and modification of surface chemistry [88], [125], [132], [133]. As the lowest  $R_s$  and the highest  $T_{550}$  values were obtained after annealing under forming gas atmosphere, the highest FOM values were also achieved under this annealing condition. The FOM values for all cases are listed in Table 4.4. As can be seen from this table, AZO thin films with 250, 500, 750, and 1000 nm thicknesses exhibited

FOM values of 0.017, 0.025, 0.043, and 0.063  $\Omega^{-1}$ , respectively. These findings imply that optical and electrical properties of RT deposited AZO thin films can be improved remarkably by post-deposition annealing under forming gas atmosphere.

Table 4.4 FOM values depending on thickness and annealing condition in RT deposited AZO thin films

Thickness (nm)	As-deposited RT	Vacuum, 300 °C, 1 h	Argon, 400 °C, 1 h	Ar+4% H <sub>2</sub> , 400 °C, 1 h
	$\phi_{TC}$ ( $\Omega^{-1}$ )	$\phi_{TC}$ ( $\Omega^{-1}$ )	$\phi_{TC}$ ( $\Omega^{-1}$ )	$\phi_{TC}$ ( $\Omega^{-1}$ )
<b>250</b>	$1.9 \times 10^{-3}$	$4.8 \times 10^{-3}$	$5.1 \times 10^{-3}$	$1.7 \times 10^{-2}$
<b>500</b>	$4.7 \times 10^{-3}$	$6.7 \times 10^{-3}$	$1.2 \times 10^{-2}$	$2.5 \times 10^{-2}$
<b>750</b>	$1.9 \times 10^{-3}$	$1.7 \times 10^{-2}$	$1.8 \times 10^{-2}$	$4.3 \times 10^{-2}$
<b>1000</b>	$2.5 \times 10^{-3}$	$1.6 \times 10^{-2}$	$1.4 \times 10^{-2}$	$6.3 \times 10^{-2}$

At this point, it is worth emphasizing that the film with a thickness of 750 nm was selected for further optimization. The idea behind this choice can be justified as follows: This study was carried out to demonstrate an optimization route to produce a high-performance transparent heater and NIR reflecting mirror based on AZO coatings via RF magnetron sputtering. As seen from the achieved values given above, the optical transmittance of all films was above 90% after forming gas annealing which is quite sufficient for transparent heater applications. On the other hand, considering the lowest  $R_s$  and highest FOM values, among all film thicknesses, only two films (750 and 1000 nm) look suitable for transparent heater applications. However, when very large-area depositions for industrial applications are considered, the 1000 nm thick film requires longer deposition times and ~ 33% more material consumption compared to 750 nm thick film. And since the 750 nm also demonstrated satisfactory optoelectronic behavior, an optimal thickness of 750 nm was chosen for deposition temperature optimization experiments.

### 4.1.3 Deposition temperature optimization

750 nm thick AZO thin films were deposited at three different substrate temperatures, i.e., 100, 200, and 300 °C, to determine the optimal deposition temperature. XRD patterns of these samples are shown in Figure 4.7. These films revealed strong preference for orientation along the *c*-axis (the strongest for 200 °C deposited), just as those deposited at RT. Similar intensity evolution as a function of substrate temperature was previously reported for AZO thin films deposited under similar conditions [134]. This may be owing to the difference between the temperature dependency of aluminum, zinc, or oxygen adatom diffusion coefficients. Furthermore, the sticking coefficients of these atoms are also temperature dependent [135]. Structural data for these samples are presented in Table 4.5. In contrast to the observed peak positions of RT deposited AZO thin films, the (002) peaks here are all shifted to higher angles, indicating a shrinkage in the *c*-parameter. The highest shift ( $2\theta = 34.53^\circ$ ) (compared to the standard (002) peak position of ZnO,  $2\theta = 34.42^\circ$ ) was observed for the films deposited at 200 °C, Table 4.5.

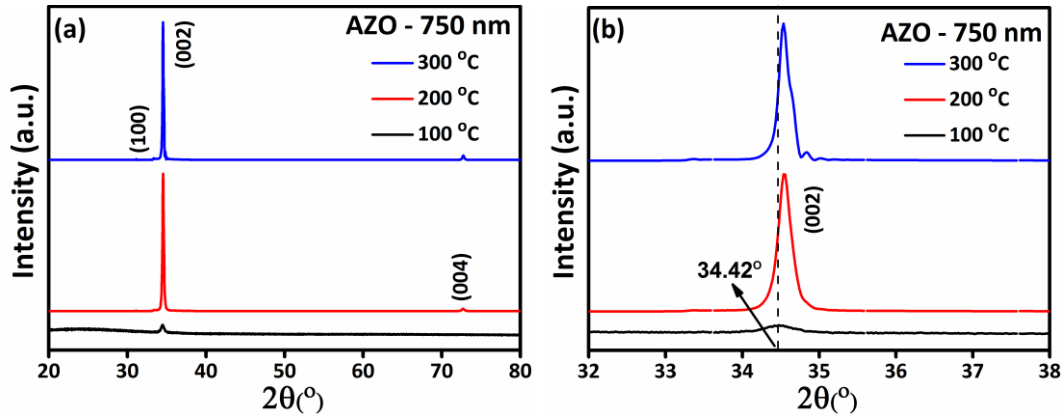


Figure 4.7 XRD patterns of 750 nm thick AZO thin films deposited at 100, 200, and 300 °C substrate temperatures

The calculated stresses all have positive values in relation with the shrinkage in the *c*-parameter, indicating that all samples are under tensile stress. The thermal

expansion coefficients of the substrate and the crystallographic planes parallel to the *c*-axis in ZnO can be assumed to be similar ( $\sim 3 \times 10^{-6} \text{ }^{\circ}\text{C}^{-1}$ ), up to a temperature of 300 °C [136]. On the other hand, the thermal expansion coefficient of the planes perpendicular to the *c*-axis in ZnO was reported as  $4.7 \times 10^{-6} \text{ }^{\circ}\text{C}^{-1}$ . Thus, the planes vertical to the *c*-axis in the film have higher thermal expansion coefficient than the substrate. This mismatch involves much greater contraction along these planes during heating/cooling, which might result in the development of tensile stresses on the deposited coatings. The amount of stress was increased than two folds with the increase of substrate temperature from 100 °C (0.327 GPa) to 200 °C (0.719 GPa) and then decreased slightly for the films deposited at 300 °C (0.588 GPa). This may be due to transition of stress mode from tensile to compression at higher deposition temperatures [137]. Furthermore, the films formed at 200 °C yielded the largest crystallite size (48 nm), indicating a higher crystallization rate than the others.

Table 4.5 Structural properties of 750 nm thick AZO films produced at substrate temperatures of 100, 200 and 300 °C

Substrate Temperature (°C)	$2\theta_{(002)}$ (°)	$2\theta_{(100)}$ (°)	<i>a</i> (Å)	<i>c</i> (Å)	$\sigma$ (GPa)	Crystallite Size (nm)
<b>ZnO</b>	34.42	31.76	3.25	5.207	-	-
<b>100</b>	34.47	-	-	5.199	0.327	31
<b>200</b>	34.53	31.13	3.31	5.190	0.719	48
<b>300</b>	34.51	31.12	3.31	5.193	0.588	44

Figure 4.8 (a and b) shows the optical and electrical properties of these films, respectively.  $T_{vis}$  values were found to be 81, 84, and 87 for the films deposited at substrate temperatures of 100, 200, and 300 °C, respectively. These values were higher when compared to the  $T_{vis}$  value of RT deposited 750 nm thick AZO thin film, but lower than those measured after annealing under various atmospheres. It is obvious that when the deposition temperature increases, the optical transmittance rises as well. Further, the films present remarkable absorption in the UV region, with the highest absorption edge (347 nm) measured for the film produced at 200 °C.

Moreover, more frequent interference fringe patterns for the films deposited at 200 °C and 300 °C suggests that these films had a lower surface roughness compared to the films deposited at 100 °C. The corresponding  $(ahv)^2-hv$  plots are given as inset of Figure 4.8 (a). As can be seen from the calculated  $E_g$  values, the highest redshift was observed for the film deposited at a substrate temperature of 200 °C. This is probably due to higher amount of Al-Zn substitution at this temperature when compared to others.

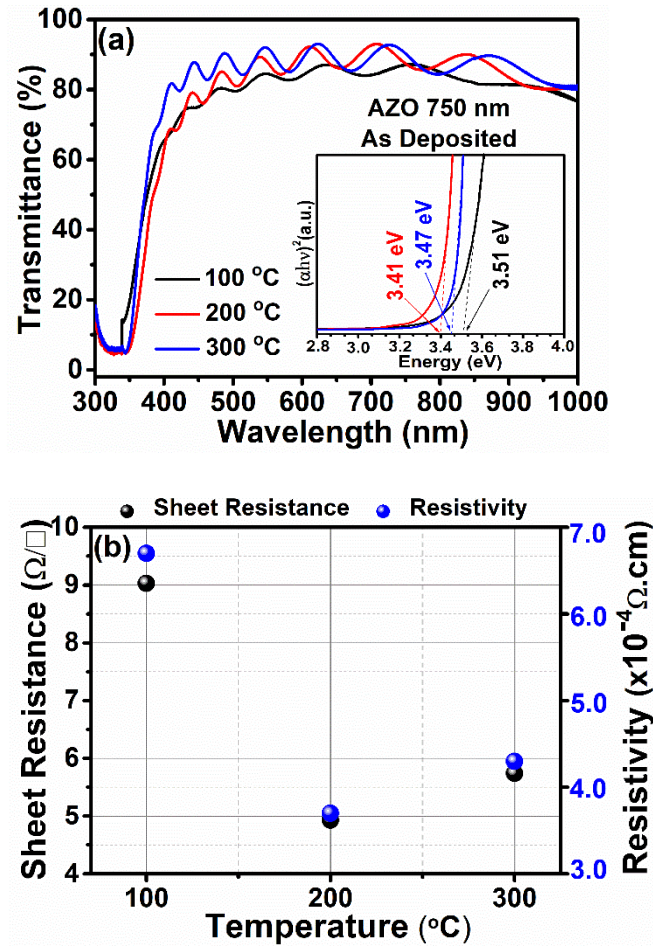


Figure 4.8 **a)** Transmittance spectra and **b)** electrical properties of 750 nm thick AZO thin films as a function of substrate temperature (The inset in (a) show the estimated direct band gaps of the films)

The electrical properties as a function of substrate temperature in 750 nm thick AZO thin films are shown in Figure 4.8 (b). The  $R_s$  values were measured as  $9.03 (\pm 2.33 \times 10^{-5})$ ,  $4.93 (\pm 3.30 \times 10^{-5})$ , and  $5.74 (\pm 1.43 \times 10^{-5}) \Omega/\square$  for the films deposited at 100, 200, and 300 °C, respectively, Table 4.6. These values were lower than those measured for RT deposited and Ar + 4% H<sub>2</sub> annealed 750 nm thick AZO thin films. Accordingly, the resistivity values were calculated to be  $6.77 (\pm 1.87 \times 10^{-9}) \times 10^{-4}$ ,  $3.70 (\pm 2.49 \times 10^{-9}) \times 10^{-4}$ , and  $4.30 (\pm 1.49 \times 10^{-9}) \times 10^{-4} \Omega.cm$ , respectively. According to these values, the highest conductivity could be obtained with the films deposited at a substrate temperature of 200 °C.

Table 4.6 Electrical properties of 750 nm thick AZO thin films produced at different substrate temperatures

Substrate Temperature (°C)	$R_s$ ( $\Omega/\square$ )	$\rho \times 10^{-4}$ ( $\Omega.cm$ )
100	9.03	6.77
200	4.93	3.70
300	5.74	4.30

In order to examine the effect of post-deposition annealing on the electrical and optical properties, 200 °C deposited sample was further processed under various annealing atmospheres. Figure 4.9 (a and b) presents the transmittance spectra and direct band gap values of AZO thin films, respectively after annealing in vacuum, Ar and Ar+4% H<sub>2</sub> atmospheres.

As it is clearly seen from the spectrum given in Figure 4.9 (a) with blue color, in comparison to as-deposited state, the highest improvement in the visible region transmittance can be obtained by forming gas annealing of the sample. In this case, the corresponding band gap was estimated as 3.57 eV, Figure 4.9 (b). In order to compare the optical properties of this sample with the others, the corresponding optical values of 100, 200, and 300 °C deposited and post-deposition annealed AZO thin films are summarized in Table 4.7.

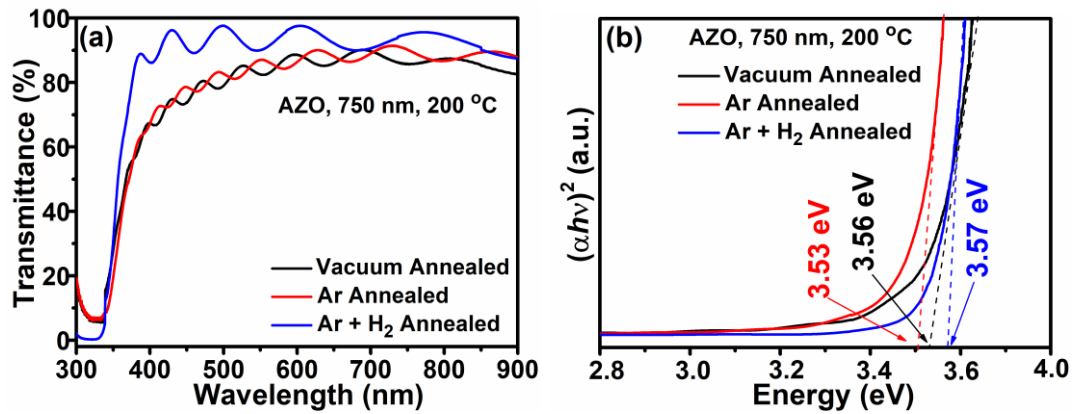


Figure 4.9 **a)** Transmittance spectra, **b)** Tauc plots and direct band gap values of 750 nm thick AZO thin film deposited at 200 °C and annealed under various atmospheres

As seen from the listed transmittance and band gap values, among others, the highest visible light transmittance (93%) was demonstrated by the sample deposited at the substrate temperature of 200 °C and then annealed under forming gas atmosphere at 400 °C for a duration of 1 h. As to remind, this sample exhibited a higher crystallite size than that of 100 and 300 °C deposited thin films (in as-deposited state). Therefore, higher visible transmittance of this thin film may be attributed to improved crystallization, a higher crystallite size and decrease in the optical scattering after post-deposition annealing.

Table 4.7 Comparison of the optical properties of 750 nm thick AZO thin films in as-deposited state and after annealing under various atmospheres

Substrate Temperature (°C)	As Deposited RT		Vacuum, 300 °C, 1 h		Ar, 400 °C, 1 h		Ar+4% H <sub>2</sub> , 400 °C, 1 h	
	$E_g$ (eV)	$T_{vis}$ (%)	$E_g$ (eV)	$T_{vis}$ (%)	$E_g$ (eV)	$T_{vis}$ (%)	$E_g$ (eV)	$T_{vis}$ (%)
100	3.51	81.14	3.55	88.06	3.55	83.78	3.65	87.92
200	3.41	84.03	3.56	82.30	3.53	83.09	3.57	93.00
300	3.47	87.03	3.53	87.58	3.55	87.06	3.61	88.05



The electrical properties of AZO thin films vary depending on the deposition temperature and annealing atmosphere. Table 4.8 presents the corresponding electrical values of AZO thin films deposited on substrates at 100, 200, and 300 °C and then annealed for 1 h and 300 °C under vacuum, 400 °C under Ar, and 400 °C under Ar+4% H<sub>2</sub> atmospheres.

Table 4.8 Comparison of the electrical properties of 750 nm thick AZO thin films in as-deposited state and after annealing under various atmospheres

Substrate Temperature (°C)	As-deposited RT		Vacuum, 300 °C, 1 h		Ar, 400 °C, 1 h		Ar+4% H <sub>2</sub> , 400 °C, 1 h	
	$R_s$ (Ω/□)	$\rho \cdot 10^{-4}$ (Ωcm)	$R_s$ (Ω/□)	$\rho \cdot 10^{-4}$ (Ωcm)	$R_s$ (Ω/□)	$\rho \cdot 10^{-4}$ (Ωcm)	$R_s$ (Ω/□)	$\rho \cdot 10^{-4}$ (Ωcm)
<b>100</b>	9.03	6.77	8.65	6.48	8.42	6.31	6.78	5.08
<b>200</b>	4.93	3.70	6.20	4.65	6.22	4.66	4.85	3.63
<b>300</b>	5.74	4.30	6.78	3.67	6.90	5.17	4.90	3.67

According to the values given in this table, the thin film deposited at 200 °C is more conductive than the others, both in deposited and annealed states. The lowest sheet resistance and resistivity values were obtained after forming gas annealing as 4.85 Ω/□ and  $3.63 \times 10^{-4}$  Ω.cm, respectively. In addition, this film outperformed all other RT deposited films in terms of electrical characteristics. This may be attributed to the effect of higher substrate temperatures on the crystallinity and doping efficiency of Al atoms in the ZnO lattice.

The FOM (Ω<sup>-1</sup>) values of 750 nm thick AZO thin films deposited at different substrate temperatures and annealed under various conditions are demonstrated in Table 4.9. Once more, this table proves the superiority of 200 °C deposited sample to others in terms of optoelectronic properties. The highest FOM value among all samples was obtained with the sample after deposition at 200 °C substrate temperature and then post-annealed under Ar+4% H<sub>2</sub> atmosphere. The FOM value

of this thin film was calculated as  $28.4 \times 10^{-2} \Omega^{-1}$  using a transmittance value of ~90% at 550 nm wavelength and sheet resistance of  $4.85 \Omega/\square$ .

Table 4.9 Comparison of the FOM values of 750 nm thick AZO thin films in as-deposited state and after annealing under various atmospheres

Substrate Temperature (°C)	As-deposited RT	Vacuum, 300 °C, 1 h	Argon, 400 °C, 1 h	Ar+%4 H <sub>2</sub> , 400 °C, 1 h
	$\phi_{TC} (\Omega^{-1})$	$\phi_{TC} (\Omega^{-1})$	$\phi_{TC} (\Omega^{-1})$	$\phi_{TC} (\Omega^{-1})$
<b>100</b>	$1.99 \times 10^{-2}$	$3.05 \times 10^{-2}$	$1.73 \times 10^{-2}$	$3.26 \times 10^{-2}$
<b>200</b>	$5.49 \times 10^{-2}$	$2.35 \times 10^{-2}$	$4.00 \times 10^{-2}$	$28.4 \times 10^{-2}$
<b>300</b>	$7.43 \times 10^{-2}$	$5.60 \times 10^{-2}$	$6.61 \times 10^{-2}$	$8.86 \times 10^{-2}$

These findings clearly reveal that the optimum processing conditions for the AZO thin film coatings are layer thickness of 750 nm and deposition at a substrate temperature of 200 °C followed by annealing in an Ar+4% H<sub>2</sub> atmosphere. Thus, the final AZO/SiO<sub>2</sub> thin films were produced using these parameters for the AZO layer.

## 4.2 Production of AZO/SiO<sub>2</sub> thin films

AZO/SiO<sub>2</sub> thin films were produced on 50x75 mm<sup>2</sup> glass substrates. Prior to deposition, the substrates were heated to 200 °C in the vacuum chamber and AZO layer deposition was performed at a fixed substrate geometry, i.e., without substrate rotation. After the deposition completed, the thin films were cooled down to room temperature and removed from the sputtering system. The edges of the AZO layer were covered with a polymeric coating (Figure 4.10 (a)) and then installed back into the vacuum system. SiO<sub>2</sub> top layer deposition was performed at RT on these samples and the substrates were rotated at 8 rpm during the deposition process. The sample was then annealed for one hour at 400 °C in Ar+4% H<sub>2</sub> atmosphere. The digital image of this sample is given in Figure 4.10 (b), showing the film is highly transparent.

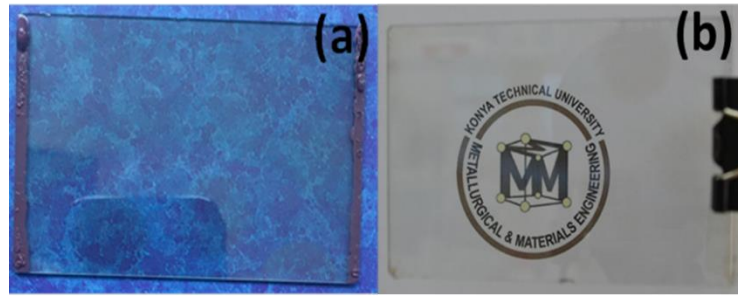


Figure 4.10 Digital images of 750 nm thick AZO/SiO<sub>2</sub> thin film **a)** deposited at 200 °C, **b)** after annealing under Ar+4% H<sub>2</sub> atmosphere for 1 h at 400 °C

#### 4.2.1 Structural analysis of AZO/SiO<sub>2</sub> thin films

Figure 4.11 (a) presents the XRD patterns of AZO samples deposited at 200 °C, then capped with SiO<sub>2</sub> after cooling, and then annealed for 1 h at 400 °C in an Ar+4% H<sub>2</sub> atmosphere. For comparison, the pattern of single layer AZO thin film is shown at the bottom. The detailed view of (002) peaks in this patterns are demonstrated in Figure 4.11 (b).

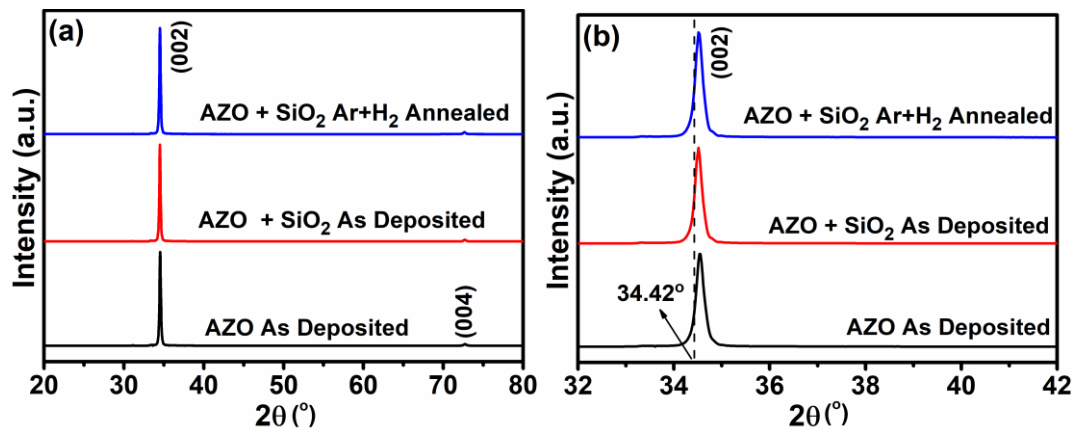


Figure 4.11 **a)** XRD patterns of AZO and AZO/SiO<sub>2</sub> thin films deposited at substrate temperature of 200 °C, along with annealed AZO/SiO<sub>2</sub> thin film **b)** Magnified view of the (002) peaks for the given pattern (a)

As it is seen from the patterns, SiO<sub>2</sub> capping layer formed in amorphous structure. There is no sign of crystallization for this layer after annealing. Further, the pattern belongs to annealed sample did not provide any evidence for the formation of any crystalline phase as a result of any reaction between the SiO<sub>2</sub> and AZO layers. As can be remembered from the discussions given on Figure 4.7 (b), with the heating of the substrate, the peak positions shifted to right for AZO in comparison to the peak positions of standard ZnO reported in JCPDS Card No.36-1451. This is also valid for the sample that was deposited at 200 °C and then capped with SiO<sub>2</sub> layer Figure 4.11 (b). With annealing, there was no further change in the peak positions. The XRD pattern obtained after annealing showed a minor increase in the intensity of the (002) and (004) peaks rather than a change in their positions. This result might be interpreted as an increase in the crystallinity of the thin film due to annealing.

#### 4.2.2 Morphological analysis of AZO/SiO<sub>2</sub> thin films

Figure 4.12 (a and b) demonstrates the 2D AFM surface images of AZO thin films that were produced at a substrate temperature of 200 °C, cooled down to RT, and then coated with a thin SiO<sub>2</sub> layer. These images suggest that AZO and AZO/SiO<sub>2</sub> thin films exhibit equiaxed grains (due to the *c*-axis preferred orientation for AZO thin films), but the grains appear finer in case of SiO<sub>2</sub> top layer. The average grain size of AZO thin film formed at 200 °C substrate temperature was calculated to be 71 nm using *Image J* software. This analysis was conducted on 1 µm x 1 µm area using at least 30 different grains. This value (71 nm) is greater than the crystallite size obtained from XRD data (48 nm). The larger size obtained from the AFM image can be explained by the fact that the coarser grains in AZO thin films are formed by the aggregation of small crystallites with identical orientations [138], [139]. On the other hand, the difference between the obtained sizes could be due to the low resolution of the AFM images, where the combination of numerous small crystallites might be thought as one grain. However, under all circumstances, investigations show that AZO thin films deposited at a substrate temperature of 200 °C have grains

finer than 100 nm. Figure 4.12 (a) also demonstrates that the film is highly dense, crack-free, and has a certain level of roughness

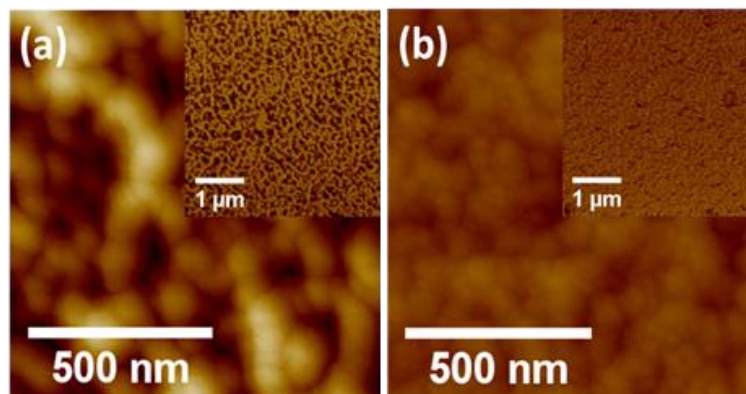


Figure 4.12 AFM surface images of AZO and AZO/SiO<sub>2</sub> thin films **a)** deposited at 200 °C, **b)** SiO<sub>2</sub> top layer coated at RT following the deposition at 200 °C (inset images (a) and (b) provide a general view of the surface)

The SiO<sub>2</sub> coated surface has considerably finer particles compared to the that of uncoated AZO surface, Figure 4.12 (b). Although the SiO<sub>2</sub> layer was found to be amorphous from the XRD measurements, we have also conducted crystallite size calculation on this sample, due to grainy appearance on the surface. The average size was found to be 53 nm. When the final sizes and the inset images for both samples compared, AFM results imply a finer and less rough surface after SiO<sub>2</sub> capping.

Figure 4.13 (a) and (b) shows three-dimensional topographies of AZO and AZO/SiO<sub>2</sub> thin films. These images were generated using a 2 μm x 2 μm surface area. The maximum height on the y axis is 200 nm. As can be seen, for both samples, the surfaces are uniform, dense, and free of cracks/voids. On the other hand, the surface without the SiO<sub>2</sub> capping layer appears rougher. This statement is in accordance with the estimated root mean square roughness (RMS) values using these images. The RMS roughness of the AZO and AZO/SiO<sub>2</sub> thin films were measured to be 21.7±0.90 nm and 6.29±0.26 nm, respectively. This indicates that a thin SiO<sub>2</sub> capping layer can significantly reduce the roughness of as-deposited AZO thin films. This property is especially important for reducing mechanical wear and chemical

reactivity of any transparent heater which will be exposed to environmental conditions.

Figure 4.13 (c) and (d) shows FE-SEM surface images of AZO (as-deposited, 200 °C, 750 nm thick) and AZO/SiO<sub>2</sub> (annealed, Ar+4% H<sub>2</sub>, 400 °C, and 1 h) thin films. The surface topography of AZO thin film in its as-deposited state is relatively rough, with hills and valleys, but uniform and compact, with no cracks. This agrees well with the AFM topography results. This is a fairly common appearance for sputtered AZO thin films on glass substrates at a deposition temperature of 200 °C [140], [141]. The inset provides for a larger scale analysis of the morphology and shows the film's homogeneity. In the case of annealed films with a SiO<sub>2</sub> capping layer, the hill/valley morphology was replaced with a smoother surface. The inset presents the through thickness fracture surface image of this film.

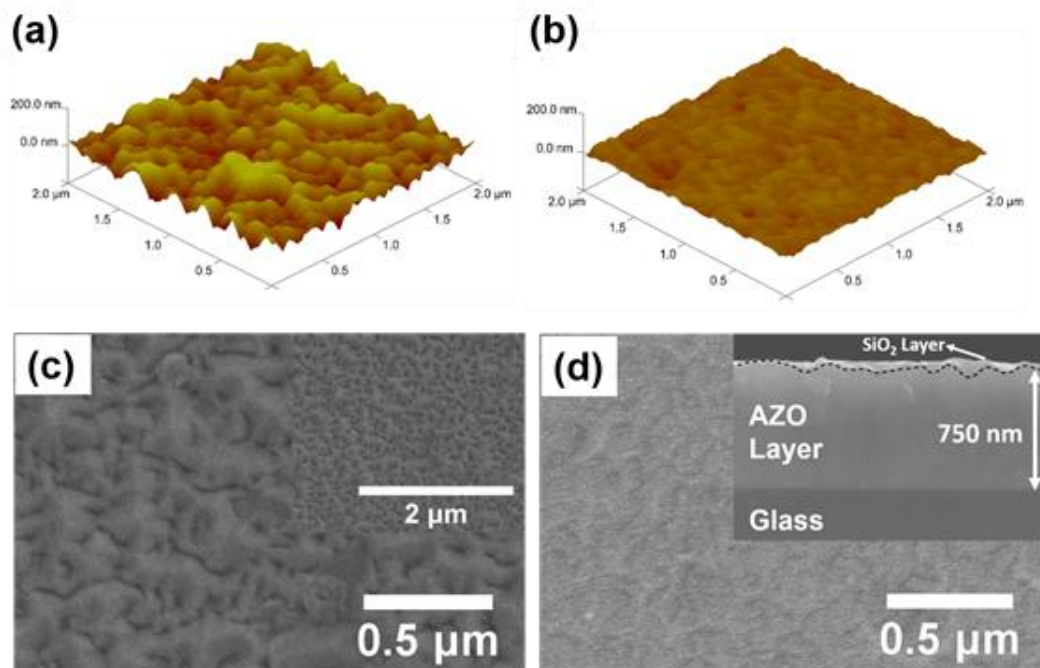


Figure 4.13 AFM surface topography of **a)** 200 °C as-deposited AZO, **b)** SiO<sub>2</sub> capped as-deposited AZO, and FE-SEM surface images of **c)** 200 °C as-deposited AZO, **d)** Ar+4% H<sub>2</sub> annealed AZO/SiO<sub>2</sub> (the insets given in (c) shows the general view of the surface of as deposited AZO and (d) cross-section FE-SEM image of Ar + 4% H<sub>2</sub> annealed AZO/SiO<sub>2</sub> sample)

The thin SiO<sub>2</sub> layer on the surface was barely visible, therefore the boundary between the two layers is separated by the dashed line as a guide for the eye. An increase in grain size and a more textured surface morphology have previously been discussed in the literature for AZO thin films annealed in an Ar+H<sub>2</sub> atmosphere [142], [143]. However, there are several inconsistencies in the effect of post-deposition annealing on the grain size and roughness of AZO thin films [141], [144], [145].

According to the XRD data, the crystallite size of the as-deposited AZO/SiO<sub>2</sub> thin film increased from 48 nm to 51 nm after annealing in an Ar+4% H<sub>2</sub> environment. These results indicate that annealing of AZO thin films with a SiO<sub>2</sub> capping layer improved both crystallinity and surface characteristics.

### **4.2.3 Optical analysis of AZO/SiO<sub>2</sub> thin films**

#### **4.2.3.1 Visible region**

Following the structural and morphological analysis, the optical characteristics of AZO/SiO<sub>2</sub> thin films were studied using UV-Vis and UV-Vis-NIR spectrophotometers. Figure 4.14 (a) shows the transmittance spectra of AZO, SiO<sub>2</sub> coated AZO, and annealed AZO/SiO<sub>2</sub> thin films for the wavelength range of 350 to 900 nm. As seen in the figure, the SiO<sub>2</sub> capped sample does not provide a significant improvement in transparency compared to the uncoated sample in the visible region. The  $T_{vis}$  values of these samples between 400 and 700 nm were calculated to be 84 and 85%, respectively. On the other hand, annealing considerably affected the average light transmittance of SiO<sub>2</sub> capped sample. By annealing this sample, transmittance could be improved to 96%. As previously discussed,  $T_{vis}$  of AZO thin films made without SiO<sub>2</sub> coating can be increased by up to 93% using forming gas annealing. When the absorption edges of the samples are evaluated, an increasing blue-shift can be observed in the spectra in the order of AZO, AZO/SiO<sub>2</sub>, and annealed AZO/SiO<sub>2</sub>. These findings imply that the transmittance of AZO thin films can be improved further by using a capping layer like SiO<sub>2</sub>.

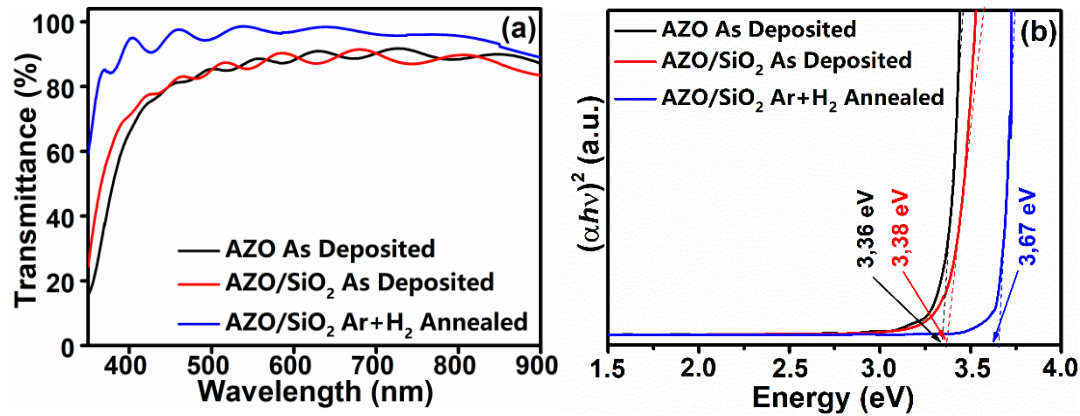


Figure 4.14 a) Transmittance spectra and b) Tauc's plots of as-deposited AZO, SiO<sub>2</sub> capped as-deposited AZO, and Ar+4% H<sub>2</sub> annealed AZO/SiO<sub>2</sub> thin films

The calculated band gap values of these films can be seen in Figure 4.14 (b). The band gap increased slightly with the SiO<sub>2</sub> coating compared to the uncoated sample (3.36 eV to 3.38 eV). As given above, SiO<sub>2</sub> capping layer led an increase of only 1% on the transmittance. On the other hand, the broadening of band gap is much more obvious for the annealed sample and band gap energy of this sample was found to be 3.67 eV.

#### 4.2.3.2 Near-Infrared Region

UV–Vis–NIR spectroscopy was used to investigate the NIR reflection behavior of as-deposited AZO, AZO/SiO<sub>2</sub>, and annealed AZO/SiO<sub>2</sub> thin films up to a wavelength of 2.5  $\mu\text{m}$ . Figure 4.15 depicts the reflectance spectra of these samples. In the as-deposited condition, AZO thin films exhibited very low NIR reflection, with only 16.5% at 2.5  $\mu\text{m}$ . NIR reflectance was greatly enhanced after SiO<sub>2</sub> capping. Reflection started to increase for this film at a wavelength of 1520 nm, reached 30% at 2.2  $\mu\text{m}$ , and reached a maximum of 47% at a wavelength of 2.5  $\mu\text{m}$ . This implies that the reflection of the sample at NIR-region can be improved via a capping layer.



On the hand, heat reflecting behaviour was essentially improved after annealing of the sample. In case of post-deposition annealed AZO/SiO<sub>2</sub> thin film, the reflectance starts to increase at 1475 nm and reached 30% at 1.8  $\mu\text{m}$ . As seen from the blue colored spectrum in the figure, the reflectance of the film increased further with the increasing wavelength and reached a value of 73% at a wavelength of 2.5  $\mu\text{m}$ .

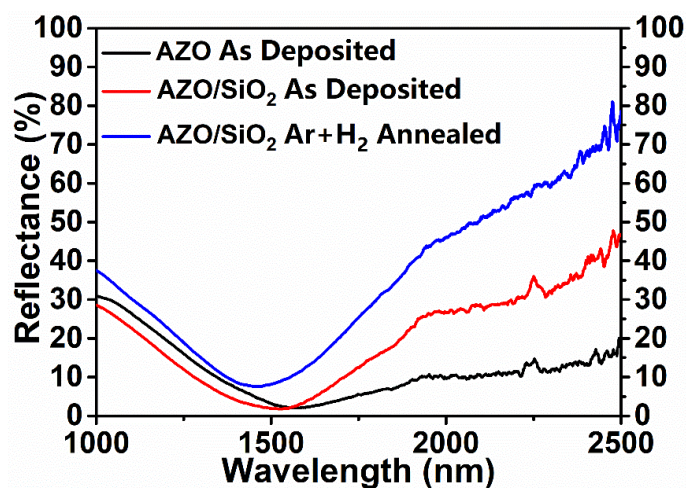


Figure 4.15 Reflectance spectra of as-deposited AZO, SiO<sub>2</sub> capped as-deposited AZO, and Ar+4% H<sub>2</sub> annealed AZO/SiO<sub>2</sub> thin films

The ability to adjust optical transmittance and reflectivity by determining an appropriate sheet resistance for the AZO coatings is well documented in the literature [146]. As a result, the improvement in reflection can be attributed to an increase in the carrier concentration of AZO thin films with annealing and also to the boundary effect observed in semiconductor/insulator multilayer thin films. This statement will be supported by Hall measurements in the following sections [73].

As will be remembered from the introduction section, one of the aims of this study is to develop an In-free transparent heater and heat reflecting coating composition. Therefore, it is worth to mention that the value of 73% reflectance obtained by AZO/SiO<sub>2</sub> thin films at 2.5  $\mu\text{m}$  is almost 3.5 times higher than the value of 20 % reflectance which was reported for commercial ITO coatings for this wavelength [147]. The data presented here for SiO<sub>2</sub> capped AZO thin films is quite encouraging

when compared to other values reported in literature. As an example, Miao et al. used Ar annealing to improve the reflectivity of sputter-deposited AZO thin films, and achieved only 20% reflectance at 2.5  $\mu\text{m}$  [67]. Ghosh et al. recently used Zn deposited glass as a blanket during the annealing of AZO thin films in Ar+H<sub>2</sub> environment. The annealing process was conducted at a higher temperature than 400 °C, i.e., 550 °C. At a wavelength of 2.5  $\mu\text{m}$ , the films had a maximum reflectance of roughly 50%. Most of the IR-reflective AZO and AZO/Cu/AZO thin films had much lower values [70], [77], [86], [148], [149]. On the other hand, reflectance values above 70% were mostly obtained in composite films, such as when a silver interlayer was used in between the two AZO layers [70], [150]. Furthermore, following the annealing step, the SiO<sub>2</sub> capping layer considerably improved the film's transmittance in the visible region, as seen in Figure 4.14 (a). Chen et al. showed similar changes in optical characteristics, which attributed to the protective effect of a dense SiO<sub>2</sub> layer after hydrogen annealing [65].

#### 4.2.4 Electrical analysis of AZO/SiO<sub>2</sub> thin films

The electrical properties were determined using Hall effect measurements. I-V measurements were conducted at RT, in Van der Pauw geometry, under 10 mA current, and were repeated three times. Table 4.10 shows the values obtained for as-deposited and annealed AZO/SiO<sub>2</sub> samples. As can be seen, the as-deposited sample displayed relatively consistent values for each parameter throughout all measurements. This reveals the formation of very homogenous thin film deposits via the employed deposition process. The average of the values obtained in each experiment are presented as  $\rho = 2.65 \times 10^{-4} \Omega \cdot \text{cm}$  for resistivity,  $R_s = 4.93 \Omega/\square$  for sheet resistance,  $n = 1 \times 10^{21} \text{ cm}^{-3}$  for the carrier concentration, and  $\mu = 16.72 \text{ cm}^2/\text{V s}$  for the carrier mobility in the 4<sup>th</sup> row of this table. Moreover, these values were further improved by annealing of this thin film at 400 °C for 1 h in Ar+4% H<sub>2</sub> atmosphere. The average values were obtained as  $\rho = 3.7 \times 10^{-4} \Omega \cdot \text{cm}$  for resistivity,  $R_s = 3.53 \Omega/\square$  for sheet resistance,  $n = 1.146 \times 10^{21} \text{ cm}^{-3}$  for the carrier concentration, and

$\mu=20.47 \text{ cm}^2/\text{V s}$  for the carrier mobility, after annealing. These findings imply that the improvement in the electrical conductivity of thin film with annealing is slightly related with increase in carrier concentration but strongly related with increase in carrier mobility. Thus, it can be stated that annealing of AZO/SiO<sub>2</sub> thin films promotes the displacement of Al<sup>3+</sup> and Zn<sup>2+</sup> ions while minimizing scattering by increasing grain growth, oxygen desorption, and reducing surface roughness.

Table 4.10 Electrical properties Measurements of as-deposited and annealed AZO/SiO<sub>2</sub> thin films

Sample	Measurement	$\rho \cdot 10^{-4}$ ( $\Omega \cdot \text{cm}$ )	$R_s$ ( $\Omega/\square$ )	$\eta \cdot 10^{21}$ ( $\text{cm}^{-3}$ )	$\mu$ ( $\text{cm}^2/\text{V s}$ )
Deposited at 200 °C	1	3.70	4.93	1.00	16.72
	2	3.70	4.93	1.00	16.72
	3	3.70	4.93	1.00	16.72
	<b>Average Values</b>	<b>3.70</b>	<b>4.93</b>	<b>1.00</b>	<b>16.72</b>
Annealed in Ar +4% H <sub>2</sub> atmosphere at 400 °C for 1h	1	2.65	3.53	1.15	20.45
	2	2.65	3.53	1.14	20.57
	3	2.65	3.53	1.15	20.41
	<b>Average Values</b>	<b>2.65</b>	<b>3.53</b>	<b>1.146</b>	<b>20.47</b>

#### 4.2.5 Electro-thermal performance of AZO/SiO<sub>2</sub> transparent heaters

The electro-thermal performance of 50x75 mm<sup>2</sup> sized AZO/SiO<sub>2</sub> thin films were investigated by applying various input voltages to the samples kept at room temperature. The results are shown in Figure 4.16 (a-e). The response of the heater to the applied voltage was investigated between 1 and 12 V, Figure 4.16 (a). In this test, the voltage was increased in 1 V increments at each 60 s, and the temperature increase was measured/recorded with an infrared camera. The insets refer to the captured images of the sample at the time prior to each voltage increment. The mean

surface temperature was increased almost linearly with the applied voltage over 3 V. A maximum of 150 °C was recorded for the surface temperature after applying 12 V to the sample.

Figure 4.16 (b) displays the saturation temperature and response time of the heater at 3, 6, 9, and 12 V applied potentials. The insets in the figure are the images of the samples taken with an infrared camera at the obtained steady state temperature for each condition. Temperatures of 38, 69.5, 109, and 161 °C were recorded at the applied potentials of 3, 6, 9, and 12 V, respectively. These values represent the average temperature of the entire sample surface, excluding the Ag-coated regions. In the same order, the response time, which defines the time to reach the plateau, was recorded as 65, 67, 67, and 65 s, which is almost equal in all cases, indicating that the maximum temperature is mostly influenced by the input power.

Power density ( $W$  (Watts/m<sup>2</sup>)) is one of the most essential metrics to consider while designing a transparent heater [2]. Thus, the power densities for each voltage input were determined and plotted against the associated saturation temperatures, Figure 4.16 (c). Then, the thermal resistance ( $\Delta T/\Delta W$ ) of the transparent heater was calculated using this plot.

As shown in Figure 4.16 (c), the relationship between the surface saturation temperatures and corresponding power densities are nearly linear. The thermal resistance of the transparent heater was calculated using a linear fit and was found to be 219 °C cm<sup>2</sup> /Watt. Thus thermal resistance of the heater is comparable (80 cm<sup>2</sup> Ag mesh, 255 °C cm<sup>2</sup>/Watts, 0.77 cm<sup>2</sup> Pt mesh, 258 °C cm<sup>2</sup>/Watts, 50 cm<sup>2</sup> CuS nanosheet network, 197 °C cm<sup>2</sup>/Watts, 4 cm<sup>2</sup> graphene, 163 °C cm<sup>2</sup>/ Watts) to various types of transparent heaters reported in literature [15], [151]–[153]. The sample can provide a power density of 5981 Watt/m<sup>2</sup> under an applied potential of 12 V. In comparison, the power density of ITO-based commercial transparent heaters was stated to be between 155–7750 Watts/m<sup>2</sup>. This indicates that the AZO/SiO<sub>2</sub> thin films presented here have heater properties comparable to other commercial or research-based products.

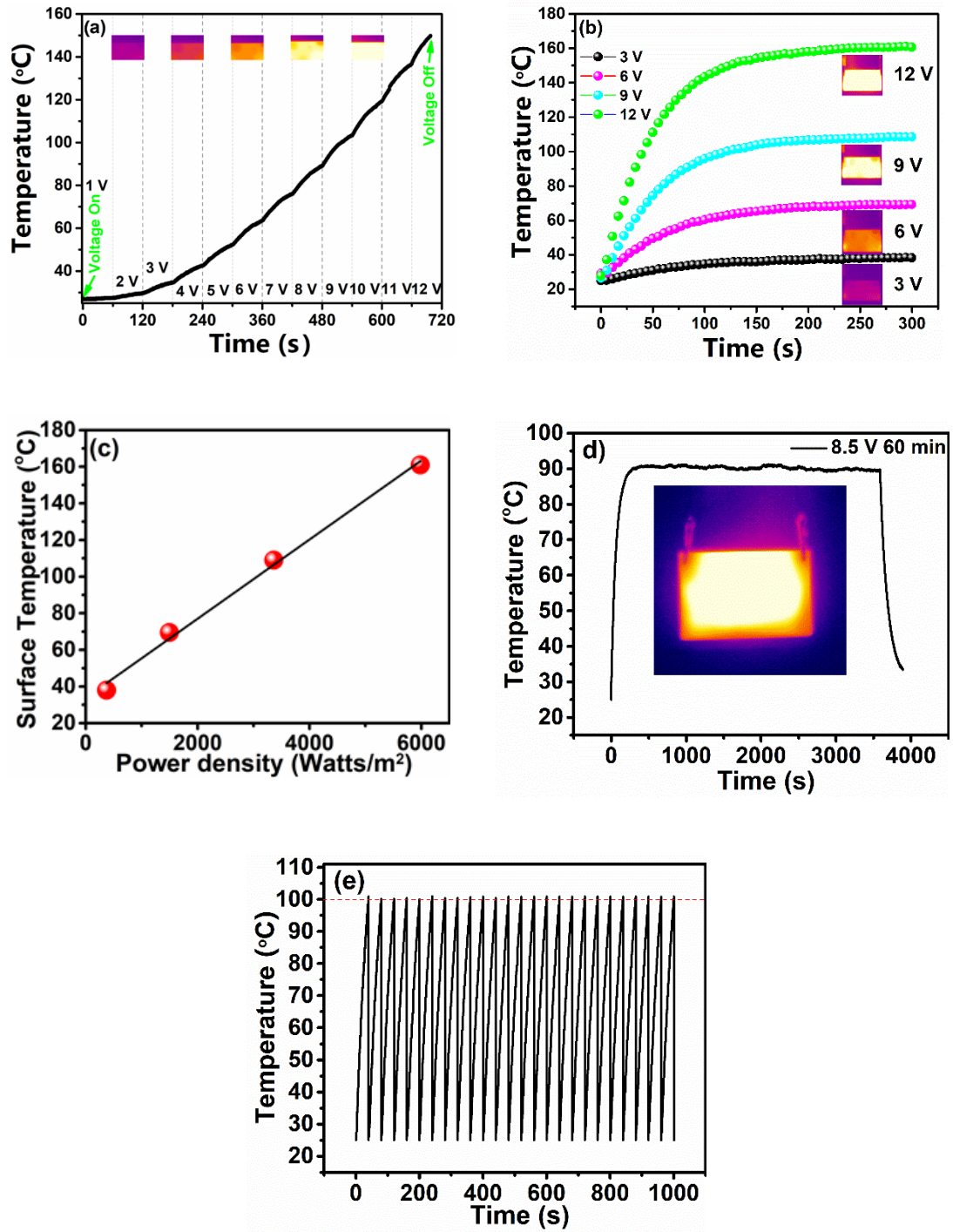


Figure 4.16 Electro-thermal response of AZO/SiO<sub>2</sub> transparent heater; **a)** thermal response of the heater to incremental input voltage increase, **b)** heating behavior under different applied voltages, **c)** surface temperature vs power density plot, **d)** long term loading stability, **e)** cyclic loading performance of the heater (the insets in a, b, and d refer to thermal camera images of the sample at the relevant temperature)

The surface temperature of the sample was evaluated as a function of time under a constant input voltage of 8.5 V to investigate the stability of the AZO/SiO<sub>2</sub> transparent heater (Figure 4.16 (d)). The surface of the sample reached a saturation temperature of 91 °C. The heating behavior was monitored for 3600 s. The temperature variation of the surface over the entire duration was observed to be insignificant, i.e.,  $\pm 1.0$  °C. The inset given in this figure denotes the IR camera image of the film and reveals the homogeneity of heat distribution on the surface.

Using this inset and Equation (3.8), the temperature homogeneity of the AZO/SiO<sub>2</sub> transparent heater was determined to be 13.66 %. This value is better than nano-wire-based defrosters used in car windows [154]. Hudaya et al. (2015) demonstrated that the temperature homogeneity in metal/FTO transparent heaters coated with a metal quantum nanoparticle layer is 14.65 % for Cr/FTO, 19.2 % for NiCr/FTO, 30% for Ni/FTO, and 19.7 % for monolayer of FTO [123]. Therefore, the surface temperature homogeneity of the AZO/SiO<sub>2</sub> transparent heater produced in this study can be considered to be quite good.

The thermal stability of the AZO/SiO<sub>2</sub> transparent heater was further investigated by cyclic loading (25 cycles) of the sample. During this test, 12 V was applied first and then switched to 0 V when the surface mean temperature reached a value of 100 °C, Figure 4.16 (e). The graph demonstrates that the peak temperature was routinely reached at around 40 s and the scattering of maximum temperature was negligible. These findings indicate that the optimized AZO/SiO<sub>2</sub> heater has remarkable heating stability and reproducibility under constant or cyclic loadings.

The deicing performance of the AZO/SiO<sub>2</sub> transparent heaters was evaluated after cooling the samples to low temperatures for 1 h in a thermally insulated box filled with dry ice. The cooled sample was then placed in the measurement setup, and the DC source was turned on when the IR-camera revealed a mean temperature of -40 °C on the surface of the heater. The tests were terminated by the removal of all water-based residues from the surface. Figure 4.17 (a) displays the sample's deicing performance at various input voltages, e.g., 6, 9, and 12 V. As seen from the inset

values next to each heating curve, the temperature of the surface reached a different maximum value depending on the applied voltage. As a result, 53 °C for 6 V, 84 °C for 9 V, and 109 °C for 12 V were achieved. This once more proves that the heating and deicing performance of the samples depends on the input power.

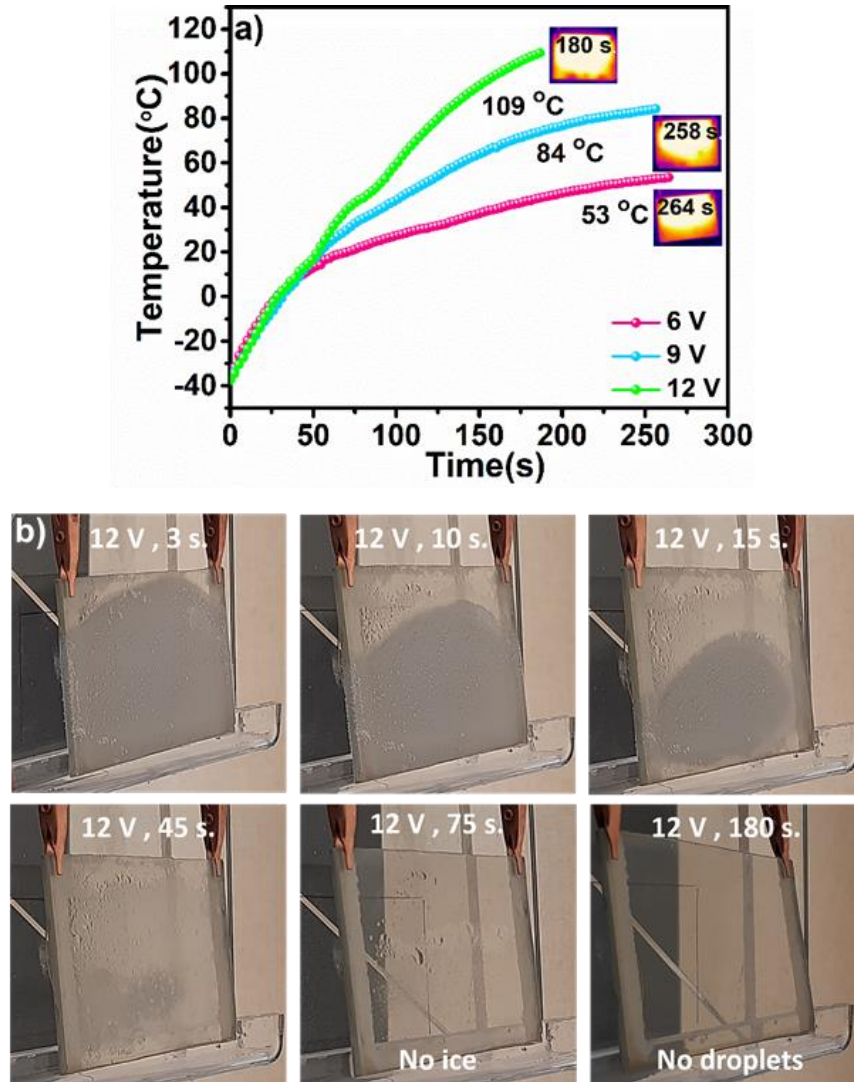


Figure 4.17 **a)** Deicing performance and heating curves of dry-ice cooled AZO/SiO<sub>2</sub> transparent heater with various input voltages, **b)** digital images showing the course of deicing on 5.0 x 7.5 mm<sup>2</sup> AZO/SiO<sub>2</sub> transparent heater under 12

During deicing, the ice began to melt (Figure 4.17(b)), and the frosted appearance was turned into water droplets on the surface. The drops get smaller and eventually vanished from the film surface. With increasing input voltage, the time required for the last droplet to disappear was decreased. The digital images Figure 4.17 (b) belongs to sample loaded with 12 V. It is apparent that the heat produced by the Joule effect was initially consumed to melt the ice and heat the substrate. Therefore, the average temperature of the sample did not rise above  $\sim 30\text{ }^{\circ}\text{C}$  during the first minute. However, as soon as the ice melted entirely and water droplets began to form on the surface, the temperature rapidly climbed up to  $80\text{ }^{\circ}\text{C}$ , and all droplets were evaporated at an average surface temperature of  $109\text{ }^{\circ}\text{C}$  after 3 min. In case of lower input voltages, a similar pattern was observed, just with lower maximum final temperatures and longer durations. This demonstrates that the optimized AZO/SiO<sub>2</sub> transparent heaters are tunable and can remove ice/water from the glass surface even at very low input voltages, such as 6 V. For practical applications, at very low ambient temperatures, the condensed ice may be melted first using a higher, e.g., 12 V input voltage, and then the nucleation of new ice crystals may be prevented by applying lower input voltages.

As mentioned in the introduction section, the performance of AZO transparent heaters has generally been reported for samples with considerably smaller active surfaces than our sample. Due to the possibility of increase in the concentration of defects (e.g., porosity, cracks, and so on) with increasing film size and considering the negative impact of these defects on conductivity, the results provided here for heaters with  $37.5\text{ cm}^2$  active area highlights the quality of the produced functional thin film coatings.



### 4.3 Optimization of amorphous ZITO thin film production

#### 4.3.1 Deposition time and sputtering pressure optimization

The combinatorial approach was utilized to determine the a-ZITO composition with the best optical and electrical properties. Thin films were produced using the deposition geometry and multi-substrate carrier magazine given in Figure 4.18 (a and b). First, the effects of sputtering pressure (high purity Ar) and time on the properties of thin films were examined. The tests were started with 5 mTorr pressure. The films were reproduced for four different deposition time, i.e., 15, 30, 45, and 60 min, on glass substrates kept at RT. The digital images of these ZITO thin films are presented in Figure 4.18 (a-d), respectively.

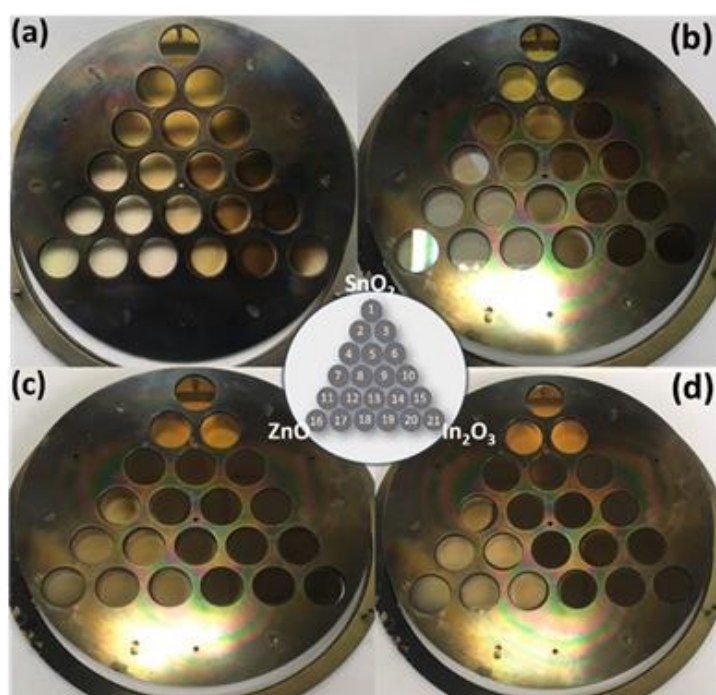


Figure 4.18 Digital images of ZITO thin films deposited at 5 mTorr sputtering pressure for various deposition time **a)** 15 min, **b)** 30 min, **c)** 45 min, and **d)** 60 min (the center schematic drawing shows the arrangement of the substrates on the carrier magazine with reference to gun 1, 2, and 3)

As can be seen in the images, the samples 1, 2, and 3 (close to gun 1) and the samples 7, 11, 12, 16, 17, and 18 (close to gun 2) appears to be transparent for all deposition conditions. Similarly, samples 6, 9, 10, 14, 15, 20, and 21, which are close to gun 3 and SnO<sub>2</sub>-In<sub>2</sub>O<sub>3</sub> line are almost opaque. After being visually examined, these thin films were electrically characterized. The results are demonstrated in Figure 4.19. The *x*-axis in this figure shows the sample numbers based on the location of the sample on the substrate holder. In addition, the *y*-axis is given in logarithmic scale, because some samples presented very high and the others very low sheet resistance values. A sheet resistance of 100  $\Omega/\square$  was accepted as a limit in terms of the highest sheet resistance, and this limit is indicated with a dashed red line in the figure.

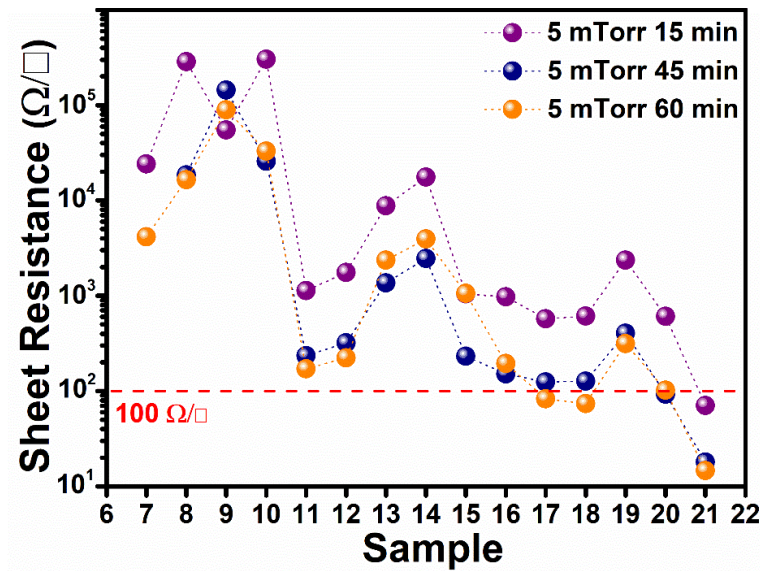


Figure 4.19 Sheet resistance of ZITO thin films deposited at 5 mTorr sputtering pressure for 15, 45, and 60 min

Independent of deposition time, no conductivity was obtained for samples 1-6. This is due to the fact that the resistance values of these samples are probably beyond the measurement range of the 4-point probe electrical measurement system utilized. In addition, for all deposition times, there is a decreasing trend in the sheet resistance values with increasing sample number. Further, this is also the case for increasing deposition time probably due to increasing film thickness. According to the data

points given in this figure, only one sample (sample 21;  $70 \Omega/\square$ ) at 15 min, two samples (samples 20 and 21;  $92$  and  $18 \Omega/\square$ ) at 45 min, and four samples (sample 17, 18, 20, and 21;  $83$ ,  $74$ ,  $100$ , and  $14 \Omega/\square$ ) at 60 min deposition time exhibited  $R_s$  values below the limit value of  $100 \Omega/\square$ . This finding suggests that for shorter deposition time, the films with In-rich compositions exhibit higher electrical conductivity and in case of longer deposition times, shifting of this behaviour to the films which are In and Zn-rich in their compositions.

Although the electrical measurements revealed an increase in the conductivity of the films for 60 min deposition, visual inspection showed that the optical properties are deteriorating with increasing deposition time. Thus, for further experiments, it was decided to examine 45- and 60-min deposition times. Figure 4.20 (a and b) shows the digital images of ZITO samples deposited at 10 mTorr sputtering pressure for 45 and 60 min, respectively.

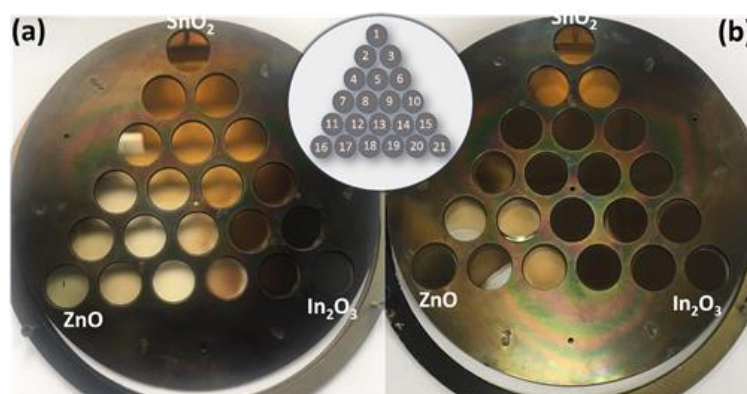


Figure 4.20 Digital images of ZITO thin films deposited at 10 mTorr sputtering pressure a) 45 min, b) 60 min

If the films in Figure 4.20 are compared in terms of their transparency with the films given in Figure 4.18 (c, 5 mTorr, 45 min), one can see that the samples (1,2, and 3) which are close to gun 1 and samples (7, 11, 12, 16, 17, and 18) that are close to gun 2 appears similar, but the transparency is much more obvious for the films deposited at 10 mTorr Ar pressure. This might be ascribed to the decrease in the thickness of

the films for the latter case due to decrease in the deposition rate at higher sputtering pressures. When a similar comparison was carried out between the films deposited under 10 mTorr Ar pressure for 45 and 60 min, it is clear that all samples are colored in the case of 60 min deposition, (see Figure 4.20 (a and b)). Further, all samples are opaque for this deposition time, except the samples 1, 2, 3, 11, 12, and 18. On the other hand, only 5 samples exhibited opaque appearance for 45 min deposition. These were the samples 10, 14, 15, 20, and 21 which are located close to gun 3.

Figure 4.21 (a) compares the sheet resistance of ZITO samples deposited for 45 and 60 min at 10 mTorr Ar pressure. Among the samples deposited for 45 min, 7,8,10,13,14,17,18, and 19 exhibited lower sheet resistance values than that of the films obtained after 60 min. Thereby, samples 11, 15, 16, 20, and 21 were found to have higher electrical conductivity after 60 min of deposition. In each case four samples were recorded with  $R_s$  value lower than  $100 \Omega/\square$ . These are the samples 16, 17, 18, and 21 ( $51, 76, 68,$  and  $22 \Omega/\square$ ) and samples 15, 16, 20 and 21 ( $98, 46, 98,$  and  $20 \Omega/\square$ ) which were obtained after 45- and 60-min deposition, respectively. Among these, sample 21 displayed the lowest  $R_s$  for each deposition time. This sample is the nearest sample to gun 3 and its composition can be expected to be very close to  $\text{In}_2\text{O}_3$ . However, these thin films are completely opaque for both deposition time.

Figure 4.21 (b) compares the sheet resistances of ZITO thin films deposited for 45 min at 5 and 10 mTorr sputtering pressures. As can be seen from the data points in the figure, all thin films except the samples 10, 19, 20, and 21 showed lower  $R_s$  values after being produced with a sputtering pressure of 10 mTorr. Furthermore, only the two samples (20 and 21;  $92$  and  $18 \Omega/\square$ ) deposited at 5 mTorr sputtering pressure have provided sheet resistance values below the  $100 \Omega/\square$  limit, whereas the number of samples increased to four, for 10 mTorr sputtering pressure. As a result of these findings, it was decided to use a sputtering pressure of 10 mTorr and 45 min deposition time to determine the final a-ZITO composition. In addition, it is worth to mention as a pre-assessment that the samples 16, 17, and 18 are promising for the purpose of this thesis study in terms of both transparency and conductivity.

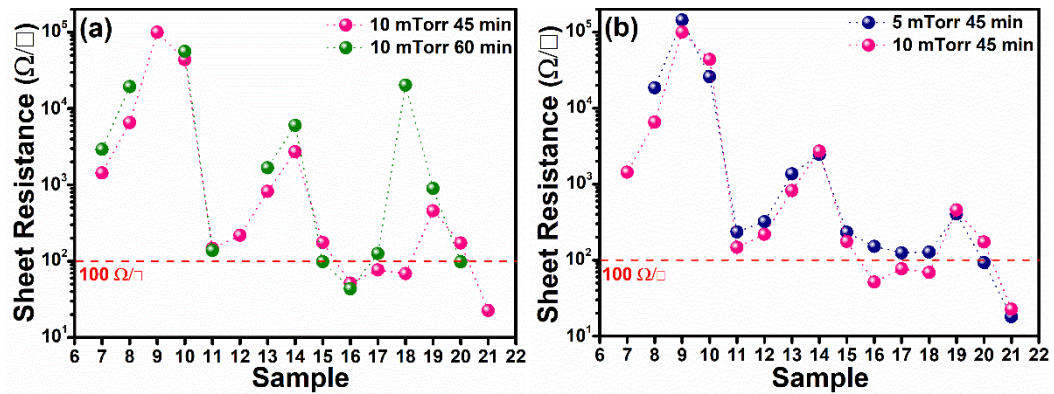


Figure 4.21 Sheet resistance of ZITO thin films a) deposited at 10 mTorr sputtering pressure for 45 and 60 min, b) deposited at 5 mTorr and 10 mTorr sputtering pressures for 45 min

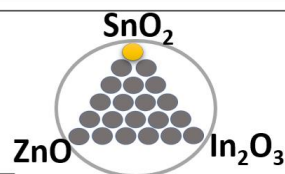
Following the optical and electrical characterization, the samples 1, 16, and 21 nearest to gun 1, 2, and 3, and samples 5, 9, and 13 that are located roughly in the center were subjected to EDX analysis. The data obtained from these measurements are shown in Table 4.11 and Figure 4.22.

The data in Table 4.11 and Figure 4.22 reveals that the composition of the thin films, which are located at the corners of the sample holder, includes almost 90% of cation atoms belongs to the nearest target material.

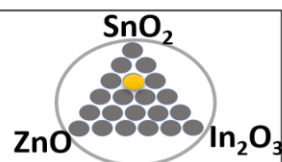
Table 4.11 EDX results belongs to ZITO thin film samples 1, 5, 9, 13, 16, and 21 deposited for 45 min at a sputtering pressure of 10 mTorr

Sample	Composition
1 (gun 1, $\text{SnO}_2$ corner)	$\text{Zn}_{0.054}\text{In}_{0.058}\text{Sn}_{0.887}\text{O}_x$
5	$\text{Zn}_{0.322}\text{In}_{0.205}\text{Sn}_{0.471}\text{O}_x$
9	$\text{Zn}_{0.328}\text{In}_{0.340}\text{Sn}_{0.330}\text{O}_x$
13	$\text{Zn}_{0.447}\text{In}_{0.355}\text{Sn}_{0.196}\text{O}_x$
16 (gun 2, $\text{ZnO}$ corner)	$\text{Zn}_{0.915}\text{In}_{0.044}\text{Sn}_{0.040}\text{O}_x$
21 (gun 3, $\text{In}_2\text{O}_3$ corner)	$\text{Zn}_{0.077}\text{In}_{0.901}\text{Sn}_{0.021}\text{O}_x$

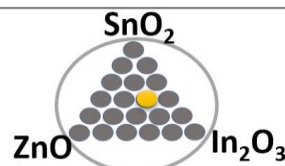
Sample 1						
EDAX ZAF Quantification (Standardless)						
Element Normalized						
SEC Table : Default						
Element	Wt %	At %	K-Ratio	Z	A	F
InL	5.80	5.84	0.0573	1.0089	0.9783	1.0000
SnL	91.11	88.70	0.9050	0.9952	0.9982	1.0000
ZnK	3.09	5.46	0.0326	1.1390	0.9258	1.0000
Total	100.00	100.00				
Element	Net Inte.	Bkgd Inte.	Inte. Error	P/B		
InL	111.31	90.89	2.29	1.22		
SnL	1676.69	86.53	0.38	19.38		
ZnK	33.57	40.31	4.74	0.83		



Sample 5						
EDAX ZAF Quantification (Standardless)						
Element Normalized						
SEC Table : Default						
Element	Wt %	At %	K-Ratio	Z	A	F
InL	23.48	20.58	0.2267	0.9840	0.9813	1.0000
SnL	55.56	47.12	0.5352	0.9708	0.9923	1.0000
ZnK	20.97	32.29	0.2252	1.1059	0.9711	1.0000
Total	100.00	100.00				



Sample 9						
EDAX ZAF Quantification (Standardless)						
Element Normalized						
SEC Table : Default						
Element	Wt %	At %	K-Ratio	Z	A	F
InL	39.20	34.09	0.3736	0.9813	0.9713	1.0000
SnL	39.29	33.05	0.3762	0.9682	0.9890	1.0000
ZnK	21.51	32.86	0.2259	1.1026	0.9523	1.0000
Total	100.00	100.00				
Element	Net Inte.	Bkgd Inte.	Inte. Error	P/B		
InL	753.19	77.33	0.60	9.74		
SnL	721.07	74.33	0.61	9.70		
ZnK	229.76	29.22	1.10	7.86		





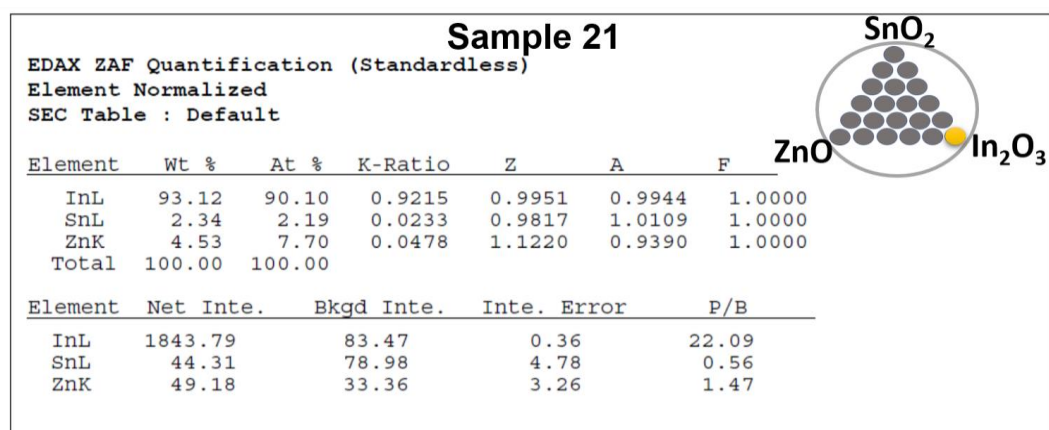
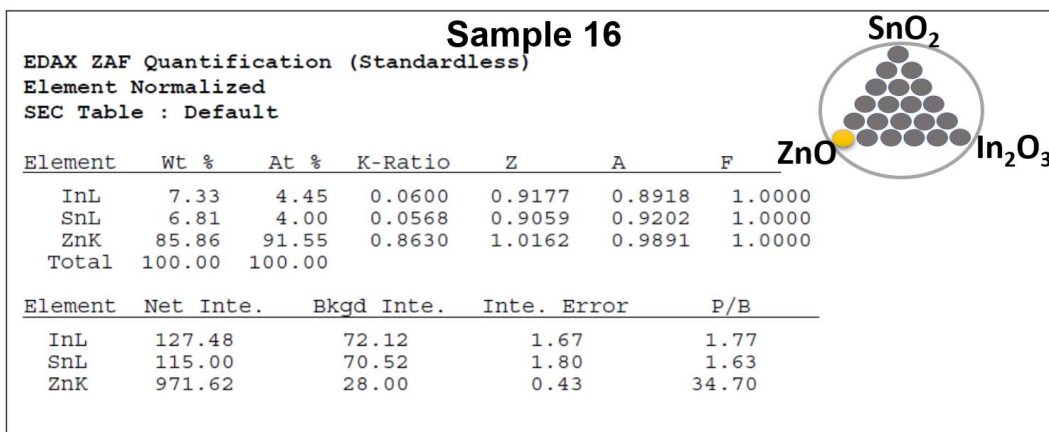
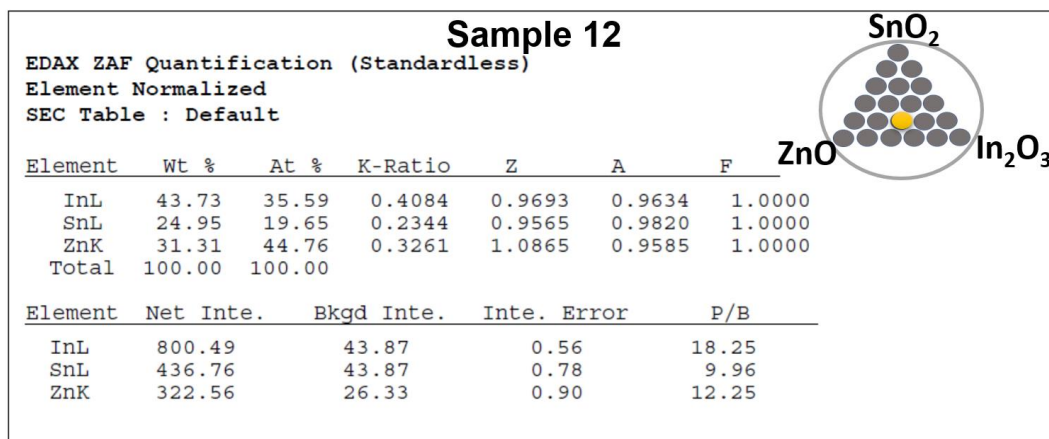


Figure 4.22 EDX results of samples 1, 5, 9, 13, 16, and 21 deposited for 45 min at 10 mTorr sputtering pressure (relevant sample numbers and their location on the sample holder are given as insets)

Figure 4.23 shows the XRD patterns of ZITO samples deposited for 45 min under 10 mTorr sputtering pressure. When the patterns in this figure are analyzed, a noticeable crystallization can be seen for samples 11, 16, 17, and 21. Other samples formed in amorphous structure, as aimed for this thesis study. Among these crystallized samples, number 16 is the nearest sample with respect to gun 2 and 11 and 17 are the samples located on the line just below this thin film. In addition, sample 21 is the nearest sample to gun 3. So, it is clear that the crystallization tendency was increased for the samples with compositions closer to pure  $\text{In}_2\text{O}_3$  or  $\text{ZnO}$ . The peaks in the XRD pattern of sample 16 are all matching with the peaks belong to (100), (002), (101), (103), and (004) planes in bulk  $\text{ZnO}$  and showed (002) preferred orientation. Similar peak matching can be practiced for the patterns of 11 and 17, but with a slight shift to lower angles in the line positions. This is probably due to the effect of  $\text{In}^{3+}$  and  $\text{Sn}^{4+}$  ions which have solubility in the lattice of  $\text{ZnO}$  [155], [156]. Finally, the XRD pattern of sample 21 showed only two detectable peaks which belongs to (222) and (440) planes of  $\text{In}_2\text{O}_3$ . In fact, it is clear that the majority of the compositions could be obtained in amorphous structure and therefore, these films will be referred to as a-ZITO in the following sections.

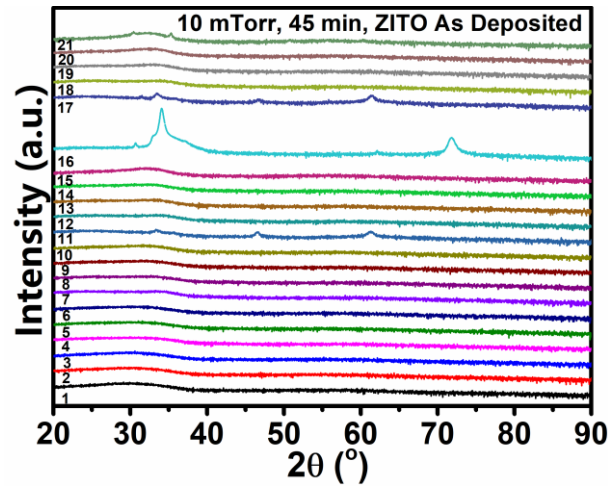


Figure 4.23 XRD patterns of ZITO thin films deposited at 10 mTorr sputtering pressure for 45 min



Figure 4.24 (a and b) demonstrates the transmittance spectra and Tauc's plots of a-ZITO thin films, respectively. The targeted optical transmittance window ( $\geq 75\%$  @ 400-700 nm) is denoted with a shaded area in Figure 4.24 (a). As it is seen, three samples provided sufficiently high transmittance values, but only in the wavelength range of about 600-700 nm. These are the samples 1, 2, and 3 which are the nearest samples to gun 1. All other samples revealed transmittance values below 75% for all visible wavelengths.

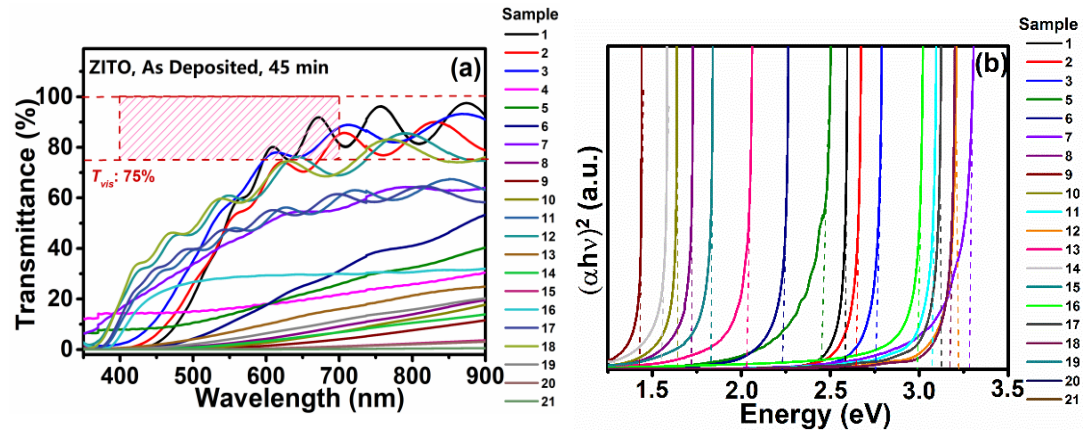


Figure 4.24 **a)** Transmittance spectra, **b)** Tauc's plots of a-ZITO thin films deposited for 45 min at 10 mTorr sputtering pressure

Table 4.12 emphasizes the optical properties of these samples. When Figure 4.24 and Table 4.12 are considered together, it is seen that the samples 7, 11, 12, 17, and 18 had slightly higher  $T_{vis}$  and  $E_g$  values compared to others. These are the samples that appear to be the most transparent in the digital photo shown in Figure 4.20 (a). In addition, samples 1, 2, and 3 have relatively high average light transmittance as well, but their  $E_g$  values are less than 3.0 eV due to their absorption edges greater than 400 nm. Sample 16, which contains more than 91% Zn by atomic ratio, appears relatively transparent in the digital image of Figure 4.20 (a), albeit with some coloring. However, it can be seen from Table 4.12 that the  $T_{vis}$  and  $E_g$  values of this sample are calculated as 26% and 2.99 eV, respectively. Further, samples 9, 15, 20, and 21 were obtained as opaque. Among these, 15, 20, and 21 are the nearest samples to gun 3 and have relatively higher amount of In in their compositions. On the other

hand, sample 9 was located close to the center of the carrier magazine which includes almost equal amounts of In, Zn, and Sn in its composition. Finally, it is worth to mention that the  $E_g$  value of the samples showed a decrease in comparison to the  $E_g$  of pure oxides, with the increase of the second and third cations in the composition. This is in accordance with the literature findings on the band gap of  $\text{In}_2\text{O}_3$ -ZnO and Sn-doped  $\text{In}_2\text{O}_3$ -ZnO thin films [157], [158].

Table 4.12 Optical properties of a-ZITO thin films deposited at 10 mTorr sputtering pressure for 45 min

Sample	$T_{vis}$ (%)	$E_g$ (eV)
1	46	2.58
2	43	2.65
3	50	2.76
4	17	-
5	15	2.46
6	12	2.23
7	40	3.28
8	3	1.71
9	1	1.43
10	2	1.64
11	42	3.07
12	55	3.22
13	8	2.03
14	3	1.55
15	<1	-
16	26	2.99
17	37	3.12
18	56	3.17
19	5	1.82
20	<1	-
21	<1	-

#### 4.3.2 Deposition temperature optimization

As mentioned above, among the samples produced at room temperature (10 mTorr sputtering pressure, 45 min), only four samples (16, 17, 18, and 21) displayed sheet resistance values less than  $100 \Omega/\square$ . These samples are all located on the ZnO- $\text{In}_2\text{O}_3$  binary equilibrium line and exhibited  $T_{vis}$  values of 27%, 37%, 56%, and less than

1% in the visible region, respectively. In other words, none of them accomplished the objectives of this thesis study. Therefore, in order to examine the effect of deposition temperature on optical properties, coatings were produced under the same deposition conditions but at a substrate temperature of 250 °C.

Figure 4.25 (a) illustrates the digital photos of these samples on the carrier magazine in comparison with the ones deposited at room temperature,

Figure 4.25 (b). When these images are compared to each other, once can see that the increase in substrate temperature improves to the transmittance of the samples, which are located closely to the center (e.g. 8, 9, and 13), rather than the films close to the corners.

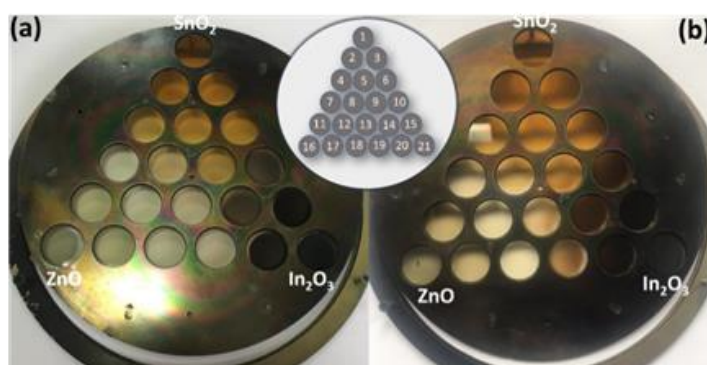


Figure 4.25 The digital images of a-ZITO thin films deposited at 10 mTorr sputtering pressure for 45 min at different substrate temperatures, **a)** 250 °C, **b)** RT (given as comparison)

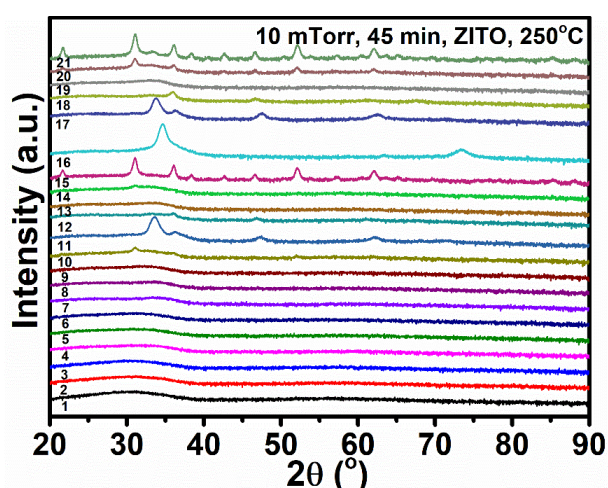


Figure 4.26 XRD patterns of a-ZITO thin films deposited for 45 min at a sputtering pressure of 10 mTorr and a substrate temperature of 250 °C

Figure 4.26 shows the XRD patterns of a-ZITO thin films deposited for 45 min at a sputtering pressure of 10 mTorr and a substrate temperature of 250 °C. When compared to the patterns of the samples deposited at RT (Figure 4.23 (a)), it is seen that higher number of samples showed crystallization during deposition at 250 °C, as expected. These are the samples 10, 11, 12, 15, 16, 17, 18, 20, and 21. In this case, pattern of sample 16 displayed only (002) and (004) peaks and exhibited complete preferred orientation along the *c*-axis. On the other hand, the peaks on the patterns of the samples 14, 15, 20, and 21 can be indexed as In<sub>2</sub>O<sub>3</sub> according to JCPDS Card No: 06-0416. The (222) peak of In<sub>2</sub>O<sub>3</sub> is clearly visible in the pattern of sample 10. This sample is located on SnO<sub>2</sub>- In<sub>2</sub>O<sub>3</sub> binary equilibrium line and contains 42 at. % In in its composition. The peaks in the patterns of sample 11 and 17 are well matching with the peaks of bulk ZnO, but with a slight shift at peak positions, as mentioned previously for the patterns of these films deposited at RT. Finally, samples 12 and 18 presented peaks matching to ZnO. However, for these samples, the preferred orientation along the *c*-axis which is valid for sample 16 was completely deteriorated and the peaks of (101), (102), and (103) planes were recorded. These samples are located next to each other on the substrate carrier magazine and can be expected to possess similar compositions. Thus, these samples contain higher amount of In and Sn in their compositions compared to that of 11, 16, and 17. Accordingly, the preferred orientation changed in these samples similar to other studies reported in literature [159].

Figure 4.27 (a) shows the transmittance spectra of a-ZITO thin films (10 mTorr, 250 °C, and 45 min) in the wavelength range of 350-900 nm. As can be seen, higher number of samples now can provide visible region transmittance in the desired range compared to the ones deposited at RT temperature (see Figure 4.24 (a)). However, only sample 18, among them exhibited 75% transmittance at around 470 nm wavelength, and then at ~500 nm, samples 7 and 12 reached to the lowest limit, and their transmittance increased with an increasing slope up to 700 nm. As will be mentioned in the annealing section below, when the samples (RT deposited samples) are annealed under Ar atmosphere at 400 °C, all samples intersect with this region

except samples 15, 16, 20 and 21. Therefore, improved transmittance is an expected result under Ar gas sputtering and substrate heating conditions. Figure 4.27 (b) gives the corresponding Tauc's plots of these samples and Table 4.14 presents their optical properties in numerical values.

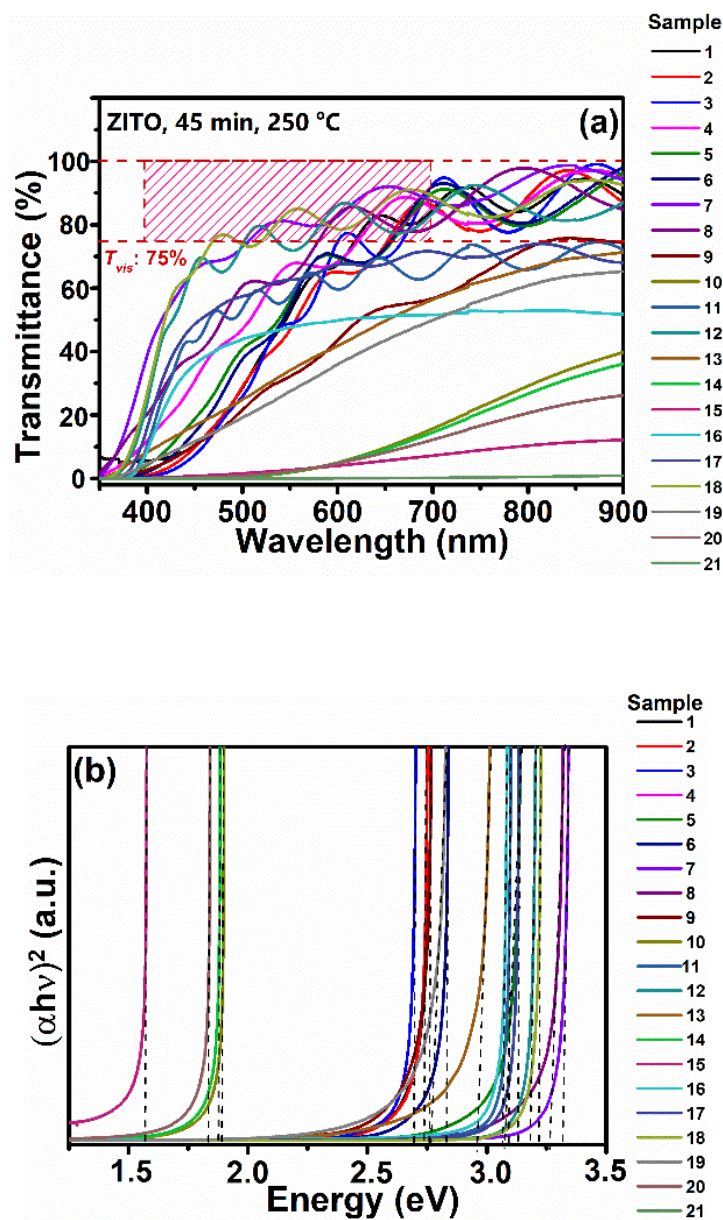


Figure 4.27 **a)** Transmittance spectra, **b)** Tauc's plots of a-ZITO thin films deposited at 10 mTorr sputtering pressure and 250 °C substrate temperature for 45 min

Table 4.13 Optical properties of a-ZITO thin films deposited at 10 mTorr sputtering pressure and 250 °C substrate temperature for 45 min

Sample	$T_{vis}$ (%)	$E_g$ (eV)
1	48	-
2	45	2.73
3	45	2.69
4	58	-
5	51	3.13
6	49	2.83
7	77	3.31
8	63	3.26
9	32	2.73
10	4	1.88
11	55	3.09
12	72	3.18
13	33	2.96
14	4	1.87
15	3	1.56
16	44	3.06
17	59	3.07
18	76	3.21
19	27	2.76
20	4	1.83
21	<1	-

When Figure 4.27 and Table 4.13 are evaluated together, one can see that the samples of 5, 7, 8, 11, 12, 16, 17, and 18 demonstrated higher  $T_{vis}$  values compared to the others. In addition, the band gaps are above 3.0 eV for these samples. Among them, only samples 7 and 18 provided sufficiently high  $T_{vis}$  values, i.e., 77% and 76%, respectively. The band gap of these thin films was estimated as 3.31 and 3.21 eV, as in the same order. It is also worth to mention that sample 12 also exhibited good optical behavior with 72% average transmittance and  $E_g$  of 3.18 eV.

Optical examination of 250 °C deposited thin films revealed that the films close to the ZnO corner generally exhibit higher transmittance than others. In fact, the

samples 7, 12, and 18 are the best three samples and all located on the third line from the ZnO corner. Further, sample 7 stands on the ZnO-SnO<sub>2</sub> binary equilibrium line, sample 18 stands on the ZnO-In<sub>2</sub>O<sub>3</sub> binary equilibrium line, and sample 12 is located in between these two. With reference to gun 2, sample 16 is nearest sample to ZnO target and the samples 11 and 17 are present on the second line from this corner. Therefore, the former includes higher amount of Zn in its composition compared to others. On the other hand,  $T_{vis}$  values of these samples were calculated as 44%, 55%, and 59% for samples 16, 11, and 17, respectively. If  $T_{vis}$  values of samples 7, 12, and 18 are included to this discussion, it is clear that the optical properties of ZITO thin films change depending on the Zn/[In+Sn] ratio. Moreover, higher  $E_g$  values were again obtained with the samples close to ZnO corner and also from the mid-region with the films having a certain amount of In+Sn in their compositions. In contrast, the samples located on and close to In<sub>2</sub>O<sub>3</sub>-SnO<sub>2</sub> binary equilibrium line presented lower  $E_g$  values.

Figure 4.28 compares the sheet resistances of samples 15-21 that are deposited at 10 mTorr sputtering pressure for 45 min at 250 °C to those of films deposited at RT.

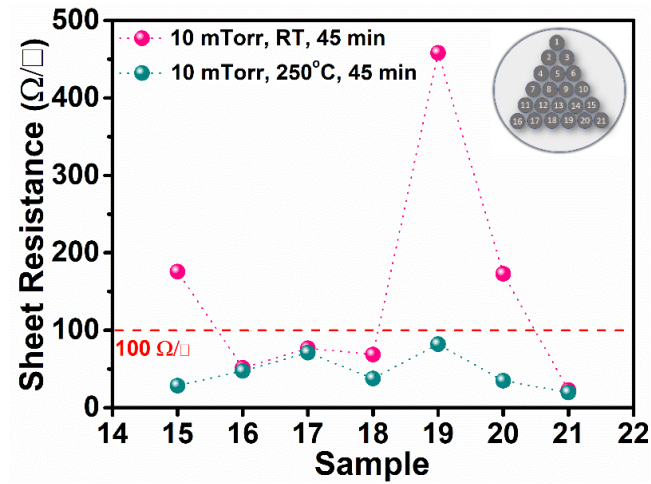


Figure 4.28 Sheet resistance values of a-ZITO thin films deposited at RT and 250 °C substrate temperatures for 45 min at 10 mTorr sputtering pressure

As can be seen from this figure, among the RT deposited samples, only 16, 17, 18, and 20 exhibited sheet resistance values less than 100 Ω/□. The sheet resistances

measured after depositing at higher temperature revealed two types of change in the electrical properties of the thin films. First, increasing the substrate temperature improved the  $R_s$  of the samples 15, 19, and 20 significantly (5 to 6-fold decrease in their  $R_s$ ). The  $R_s$  of these samples were measured to be 28, 82, and 34  $\Omega/\square$ , respectively. These samples were all formed in amorphous nature during RT deposition, but 15 and 20 were crystallized at 250 °C. Thus, the increase in conductivity may be attributed to crystallization of the films or increase in ionic displacements as the temperature is raised. On the other hand, the change in the  $R_s$  of samples 16, 17, 18, and 21 was negligible after being deposited at 250 °C. The  $R_s$  of these samples were measured to be 47, 71, 37, and 19  $\Omega/\square$ , respectively. These samples were formed as crystalline in both conditions, except sample 18. This thin film was obtained as amorphous at RT and crystallized after deposition at 250 °C. The change in the  $R_s$  of 18 is relatively high compared to 16, 17, and 21, which also supports the discussion given above on the improvement of  $R_s$  with increasing substrate temperature. As it is obvious from the reported values above, among others, the lowest  $R_s$  values were obtained with the samples 15, 20, and 21. However, these samples are still opaque after deposition at 250 °C.

At this point, sample 18 seems to be the most notable among all samples, with 76% average light transmittance in the visible region and relatively low sheet resistance of 37  $\Omega/\square$ .

### 4.3.3 Annealing optimization of a-ZITO thin films

A variety of post-deposition annealing experiments were conducted in order to improve the optical or electrical properties of RT deposited samples. Figure 4.29 (a and b) shows the digital images of these samples (15-21) in as-deposited state and after 1 h annealing at 400 °C in air atmosphere, respectively. As seen in the figures, annealing in air can improve the optical properties of samples 15-20. Especially, the sample 18 becomes quite transparent after annealing. Figure 4.29 (c) compares the measured sheet resistances of these thin film samples. Similar to optical



enhancement, annealing of the samples in air improved the electrical conductivity of almost all samples, except the sample 18. After air annealing, the sheet resistance values were measured to be 20, 46, 43, 85, 28, and 14  $\Omega/\square$  for the samples 15, 16, 17, 19, 20, and 21. On the other hand, the  $R_s$  of the sample 18 increased from 68  $\Omega/\square$  (as-deposited) to a very high value of 14.8 k $\Omega/\square$ , after air annealing. It is obvious from these data that the lowest sheet resistance values can be obtained with the samples 15, 20, and 21. Despite having the lowest  $R_s$  values, these thin films did not become transparent after annealing.

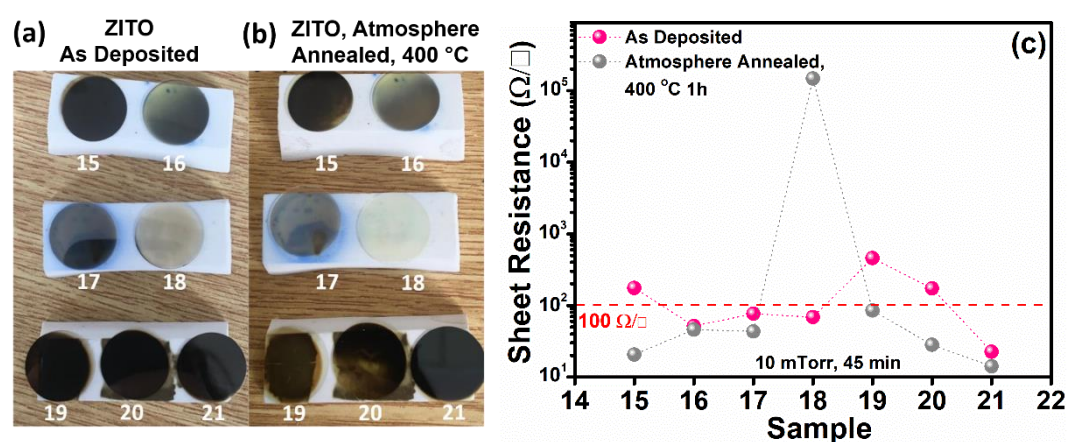


Figure 4.29 Digital images of a-ZITO thin films produced for 45 min at 10 mTorr sputtering pressure and RT, **a)** as deposited, **b)** annealed in air atmosphere for 1 h at 400 °C, **c)** sheet resistance of thin films given in (a) and (b)

To examine the effect of air atmosphere annealing on the structure of thin films XRD data from the as-deposited and annealed states of samples 17 and 18 were obtained and are given in Figure 4.30 (a and b). As previously stated, the sample 17 crystallized during the deposition process and revealed peaks that are well matching with the ZnO. However, the peak positions have slightly shifted to lower angles, and this was attributed to the presence of  $\text{In}^{3+}$  and  $\text{Sn}^{4+}$  in the structure.

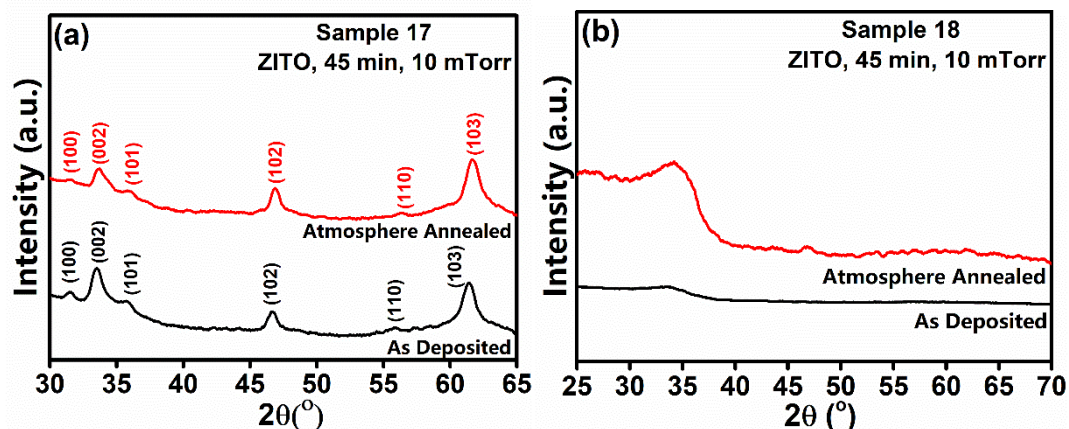


Figure 4.30 XRD patterns of ZITO thin films in as-deposited state (RT, 45 min, 10 mTorr Ar) and after annealing in air atmosphere at 400 °C for 1 h, **a)** sample 17, **b)** sample 18

The XRD pattern of annealed sample revealed a right shift for the positions of these peaks, probably due to relaxation at high temperatures. However, the lattice parameters are still greater than that of pure ZnO. Other aspects of this pattern are the decrease in the peak intensity of (100) and (002) peaks, a slight increase in the intensity of peaks such as (102) and (103) and narrowing of the peak widths with annealing. These can be interpreted as an increase in grain size and a slight improvement in crystallinity due to change in the preferred orientation during annealing. Looking at the XRD data of sample 18, which was amorphous in the as-deposited state, very low intensity and barely seen (102) and (103) peaks appeared after 400 °C annealing in air atmosphere. Besides, (002) peak can not be detected in this pattern due to superimposing of this peak with the hump. After all, it can be assumed that this sample still exhibits an XRD amorphous structure, which suggests that annealing of this thin film sample (amorphous in as-deposited state), at a moderate temperature such as 400 °C, did not change its structure significantly. Therefore, a maximum of 400 °C was selected as the safe annealing temperature for other atmospheres.

Figure 4.31 shows the sheet resistance of the samples annealed in Ar atmosphere at 300 and 400 °C, in comparison with their as-deposited state. The table given next to this figure, lists the samples with sheet resistance values less than 100  $\Omega/\square$ , under any applied condition. When the data in Figure 4.31 are analyzed, it is seen that the samples 1-7 still behave as insulator, even after annealing in Ar environment at 300 °C. However, after increasing the annealing temperature to 400 °C, measurements on these samples become available. This result is important, because it demonstrates the effect of annealing temperature on the electrical properties of the samples under consideration.

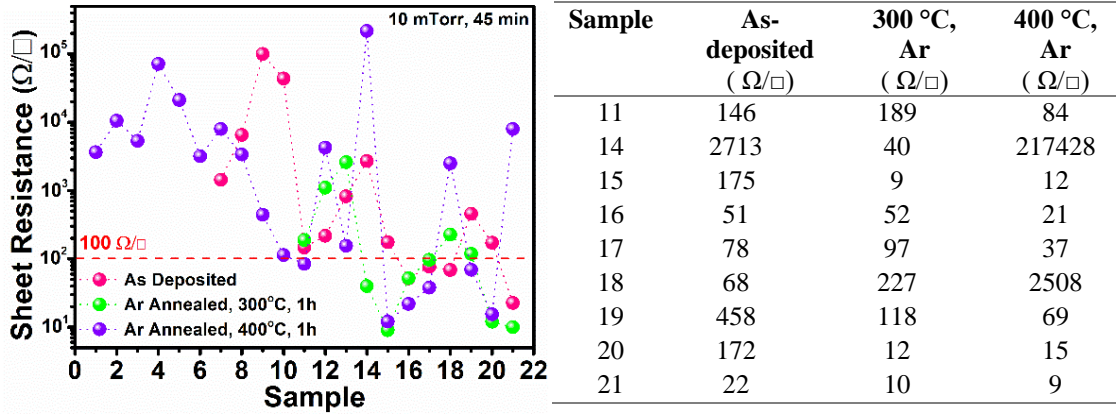


Figure 4.31 Sheet resistance of a-ZITO thin films deposited at RT and then annealed in Ar for 1 h at 300 °C and 400 °C; (the table shows the sheet resistance of samples which are lower than 100  $\Omega/\square$ , in any applied condition)

Sample 18 showed a higher transmittance than other samples, with 56%  $T_{vis}$  and an acceptable sheet resistance of 68  $\Omega/\square$ , in the as-deposited state. Its transmittance improved after annealing in air atmosphere, but its electrical conductivity dropped, and the sheet resistance increased to extremely high levels, i.e., 14.8 k $\Omega/\square$ . A similar alteration observed here, and the sheet resistance of the sample first increased to 227  $\Omega/\square$  after annealing at 300 °C and then to 2.5 k $\Omega/\square$  at 400 °C under Ar atmosphere. This sample has an In- and Zn-rich composition due to its location on the sample holder. As a matter of fact, if the sheet resistance of the sample decreases with high-temperature deposition in vacuum (37 k $\Omega/\square$ ) and increases with increasing temperature in the Ar atmosphere (2.5 k $\Omega/\square$ ), and if the value increases further with

high-temperature annealing in air ( $14.8 \text{ k}\Omega/\square$ ), an insulating phase containing oxygen in its composition should first decompose and then crystallize with annealing. However, based on the XRD patterns of this sample after high temperature deposition and atmosphere annealing, it is obvious that crystallization occurred to create only ZnO crystal structure with some preferred orientated. Therefore, the change in electrical conductivity of this sample may be related to changes in oxygen vacancy concentration or differences in ionic displacement caused by different environments and temperatures, rather than formation of a crystalline insulating phase. On the other hand, the sample 19 locates next to sample 18 on the sample holder, on the ZnO-In<sub>2</sub>O<sub>3</sub> binary equilibrium line, and its electrical conductivity was increased significantly by annealing of the sample in Ar. In case of 400 °C annealing, its  $R_s$  value was decreased down to  $69 \text{ }\Omega/\square$  from  $458 \text{ }\Omega/\square$ , in its as-deposited state. Following the same binary line on the carrier magazine, samples 20 and 21 stands at much closer location to gun 3 and therefore, their compositions are In-rich. The sheet resistance of these samples was measured to be 12 and  $10 \text{ }\Omega/\square$ , respectively, even after annealing at 300 °C temperature. This indicates that the properties of the films are highly composition dependent, and the applied combinatorial method provide a gradient in terms of composition for the samples even if they are located next to each other on the sample holder.

According to these results, samples exhibited better sheet resistance values after annealing at 400 °C. Figure 4.32 (a and b) demonstrates the digital images of these 400 °C annealed samples in comparison with their as-deposited state.

It is clear from the images provided in Figure 4.32 (a and b) that annealing in Ar atmosphere could not change the appearance of sample 21 only, which is the nearest sample to gun 3. Apart from that, films 15 and 20, which are also very close to this corner, showed slight discoloration after annealing. Furthermore, samples 10, 14, and 19, which were brownish when as-deposited, seemed almost transparent after Ar annealing. The yellow/brown colored samples near the SnO<sub>2</sub> target turned into pure yellow color as a result of annealing. Finally, the samples located close to the ZnO target remained as transparent. Figure 4.32 (c) shows the digital images of the

samples which gone through a profound change in their appearance upon annealing in Ar atmosphere in comparison to their as-deposited state. Among these, especially samples 7, 12, and 18 become completely transparent after annealing.

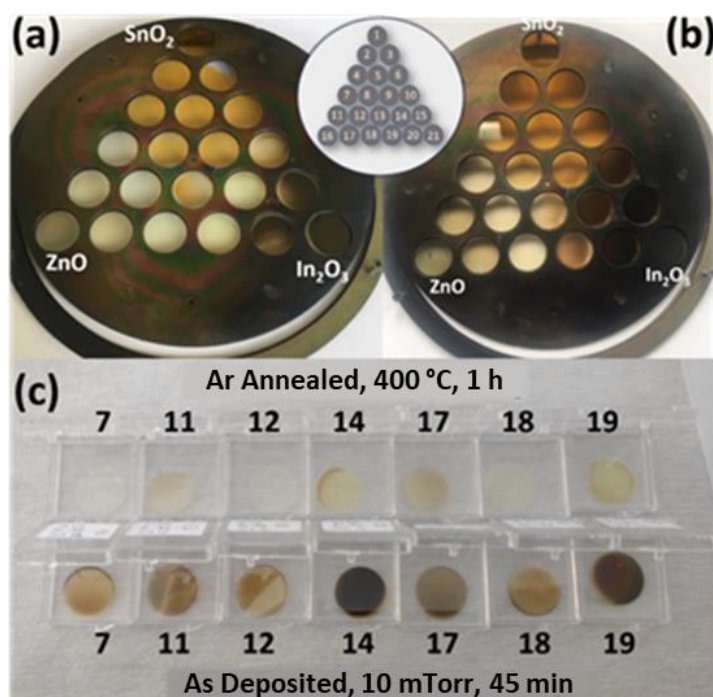


Figure 4.32 Digital images of a-ZITO thin films; **a)** annealed in Ar atmosphere for 1 h at 400 °C, **b)** in as-deposited state, **c)** samples with profound change in their transmittance after annealing

The effect of annealing on the optical properties of a-ZITO thin films were investigated by UV-Vis spectrophotometer in the wavelength range of 350-900 nm. Figure 4.33 (a) depicts the transmittance spectra of these Ar-annealed samples. In contrast to as-deposited samples, after annealing, only four samples could not satisfy the lowest transmittance limit of 75%. These are the samples 15, 16, 20, and 21 that are located closely to the ZnO and In<sub>2</sub>O<sub>3</sub> targets. Figure 4.33 (b) shows the Tauc's plots of these samples, while It is apparent from Table 4.14 that after annealing in Ar environment, 14 samples exhibited band gap values greater than 3.0 eV, and seven of them have T<sub>vis</sub> greater than 75 % limit value. This can be observed easily from Figure 4.33 (c), by checking the data points above the dashed line which



indicates the lowest limit of 75% for average transmittance in the visible region. The average transmittance values were calculated as 80, 82, 83, 84, 84, 87, and 88 % for the samples 11, 10, 19, 14, 18, 7, and 12, respectively. On the other hand, the lowest visible transmittance was demonstrated by the samples 15, 20, and 21, which are the three closest sample to gun 3. Their  $T_{vis}$  values were calculated to be 28%, 24%, and 1%, respectively.

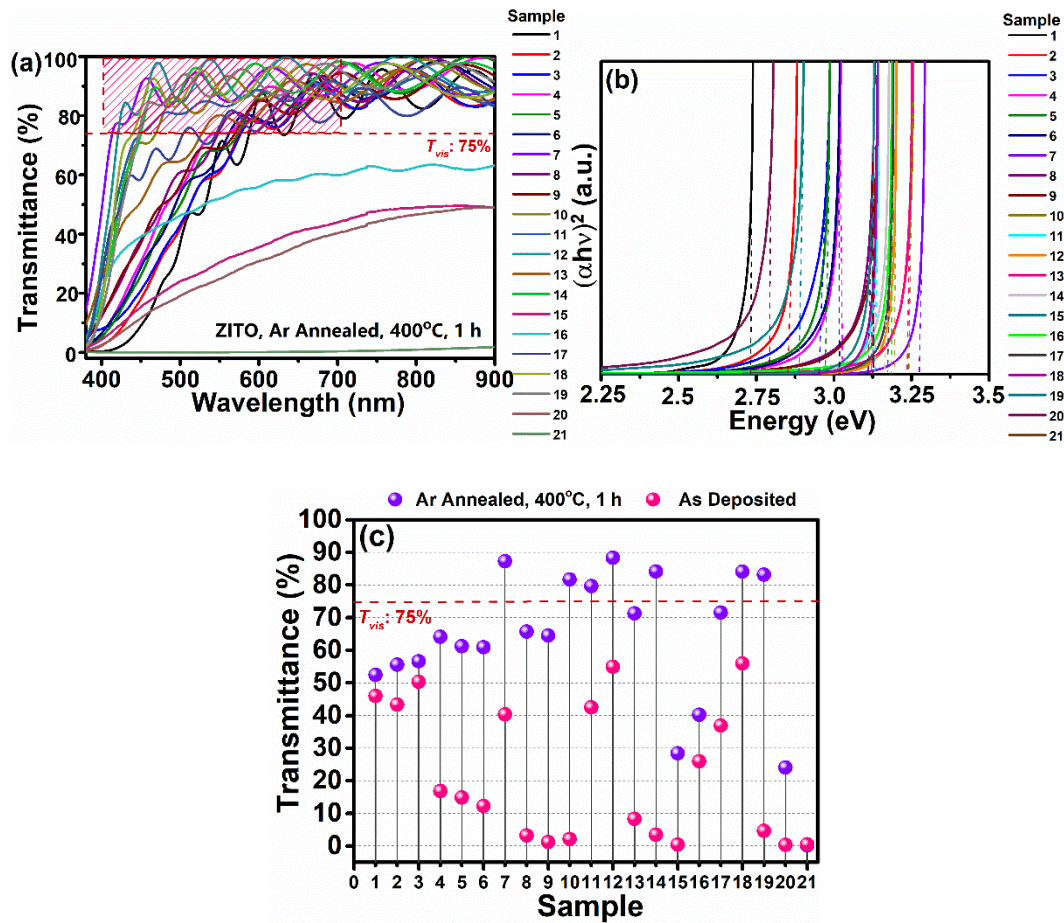


Figure 4.33 **a)** Transmittance spectra, and **b)** Tauc's plots of Ar-annealed (400 °C, 1h) a-ZITO thin films, **c)** comparison of the  $T_{vis}$  values of as-deposited and Ar- annealed a-ZITO thin films

It is apparent from Table 4.14 that after annealing in Ar environment, 14 samples exhibited band gap values greater than 3.0 eV, and seven of them have  $T_{vis}$  greater

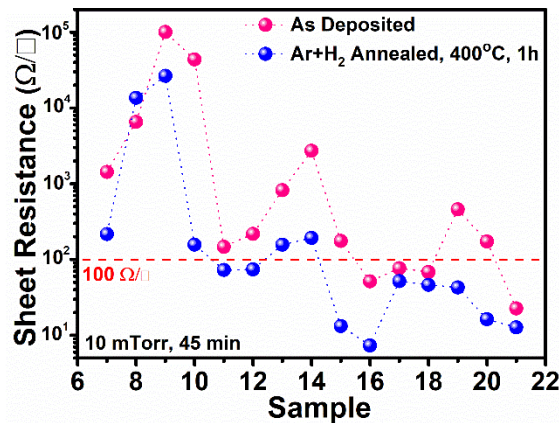
than 75 % limit value. This can be observed easily from Figure 4.33 (c), by checking the data points above the dashed line which indicates the lowest limit of 75% for average transmittance in the visible region. The average transmittance values were calculated as 80, 82, 83, 84, 84, 87, and 88 % for the samples 11, 10, 19, 14, 18, 7, and 12, respectively. On the other hand, the lowest visible transmittance was demonstrated by the samples 15, 20, and 21, which are the three closest sample to gun 3. Their  $T_{vis}$  values were calculated to be 28%, 24%, and 1%, respectively.

Table 4.14 Optical properties of a-ZITO films annealed in Ar atmosphere at 400 °C for 1 h after being deposited at RT under 10 mTorr sputtering pressure for 45 min

Sample	$T_{vis}$ (%)	$E_g$ (eV)
1	52	2.73
2	56	2.85
3	57	2.95
4	64	3.02
5	61	2.97
6	61	3.01
7	87	3.27
8	66	3.11
9	65	3.12
10	82	3.23
11	80	3.13
12	88	3.19
13	71	3.23
14	84	3.16
15	28	2.89
16	40	3.18
17	72	3.17
18	84	3.12
19	83	3.11
20	24	2.79
21	<1	-

Up to this point, only two samples could exhibit  $T_{vis}$  values above 75% and  $R_s$  values below 100  $\Omega/\square$ . These are sample 11 (80%, 84  $\Omega/\square$ ) and sample 19 (83%, 69  $\Omega/\square$ ). The values given in parenthesis for each sample can be assumed close to each other. On the other hand, the former includes only 6 wt.% In in it's composition, whereas the latter have 44 wt.% In. This indicates that the applied deposition conditions allowed the production of very different samples with various In content succesfully, but with similar optical or electrical properties.

The effect of annealing on the electrical and optical properties of a-ZITO thin films were further investigated under Ar+4%  $H_2$  atmosphere. Figure 4.34 shows the sheet resistance of the samples annealed in forming gas environment at 400 °C for 1 h, in comparison with the data belong to as-deposited state. Following a similar demonstration given above, a table is prepared and presented beside the figure to identify the samples with  $R_s$  values below 100  $\Omega/\square$ , in any processing condition.



Sample	As-deposited ( $\Omega/\square$ )	400 °C Ar+%4 $H_2$ ( $\Omega/\square$ )
11	146	72
12	218	74
15	175	13
16	51	7.3
17	78	52
18	68	46
19	458	43
20	172	16
21	22	13

Figure 4.34 Sheet resistance of a-ZITO thin films deposited at RT and then annealed in Ar+4%  $H_2$  for 1 h at 400 °C (the table shows the sheet resistance of samples lower than 100  $\Omega/\square$ , in any applied condition)

Figure 4.34 imply that Ar+4%  $H_2$  annealing improves the electrical properties of the samples as compared to their as-deposited state. The only exception here is sample 8. As shown in the table next to the figure, nine samples (11,12, 15, 16, 17, 18, 19, 20, and 21) had sheet resistance values less than 100  $\Omega/\square$  after forming gas



annealing. Furthermore, the sample 16, which exhibited  $51 \Omega/\square$  sheet resistance in the as-deposited state, reached a  $R_s$  of  $7.3 \Omega/\square$  after Ar+4 %  $H_2$  annealing. This value is comparable to  $R_s$  values provided by commercial ITO heaters. Based on these considerations, it is obvious that for some specific samples (e.g., 12 and 18), annealing under forming gas is more advantageous compared to Ar annealing in terms of their electrical conductivity. The  $R_s$  of these samples were measured to  $74 \Omega/\square$  and  $46 \Omega/\square$ , respectively, after annealing under Ar+4 %  $H_2$  atmosphere. These values are in the order of two magnitudes lower than that of obtained by Ar annealing at  $400^\circ\text{C}$ .

Figure 4.35 (a and b) displays the digital images of ZITO thin films after annealing at  $400^\circ\text{C}$  for 1 h under Ar+4 %  $H_2$  atmosphere and in-as deposited states, respectively. Similar to Ar annealing, the images given here demonstrate that forming gas annealing could improve the transparency of most samples. However, samples 15, 20, and 21 are still opaque with dark brown color. Figure 4.35 (c) clearly imply that only the sample 18 reached quite sufficient transparency among others. Although they exhibited some degree of coloration, a similar statement might be given for the samples 11, 12, and 17. This observation indicates that in terms of optical transmittance, forming gas annealing is not that successful compared to Ar atmosphere annealing.

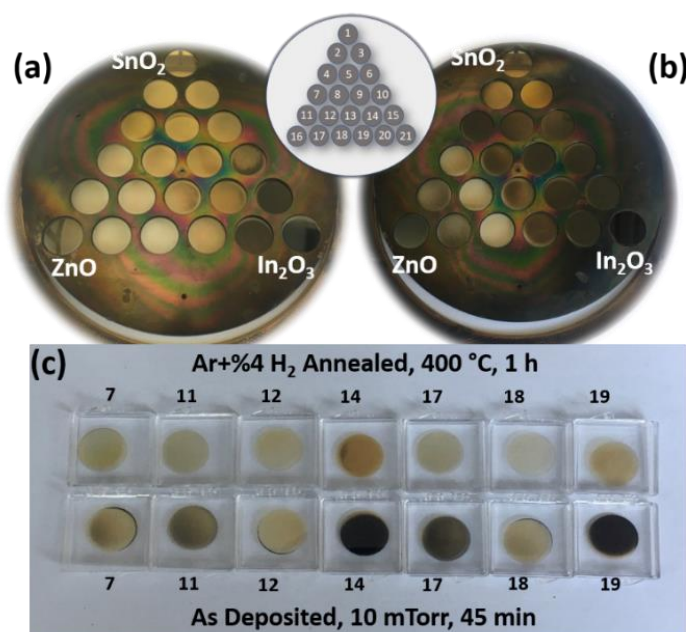


Figure 4.35 Digital images of a-ZITO thin films **a)** annealed in Ar+4% H<sub>2</sub> atmosphere for 1 h at 400 °C, **b)** in as-deposited state, **c)** samples with profound change in their transmittance after annealing

The effect of Ar+4% H<sub>2</sub> atmosphere annealing on the optical properties of a-ZITO thin films were investigated via UV-Vis spectrophotometer in the range of 350-900 nm and corresponding transmittance spectra are shown in Figure 4.36 (a). Similar to Ar annealing, the transmittance of the samples improved significantly after forming gas annealing. Only five samples showed lower visible transmittance values below 75% and did not present any value in the shaded area. On the other hand, the samples 18, 12, 7, 11, and 17 reached to this lower limit at much lower wavelengths. Among them, sample 18 exhibited 75% transmittance at ~420 nm and its transmittance increased to 95% at 700 nm wavelength. The average transmittance between this wavelength range was calculated to be 86%, for this sample. The numerical values for other samples are presented in Table 4.15.

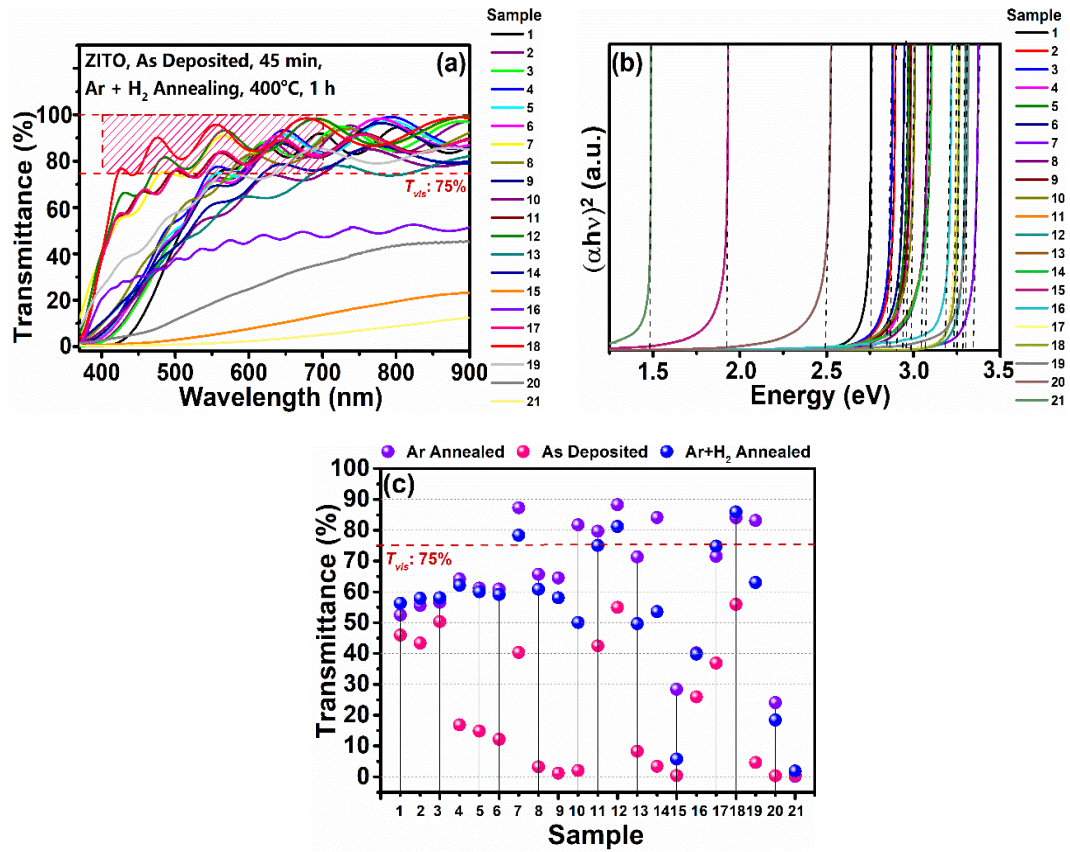


Figure 4.36 **a)** Transmittance spectra, and **b)** Tauc's plots of Ar+4% H<sub>2</sub> annealed (400 °C, 1h) a-ZITO thin films, **c)** comparison of the  $T_{vis}$  values of as-deposited, Ar annealed and Ar+4% H<sub>2</sub> annealed a-ZITO thin films

According to this table, 9 samples exhibited  $E_g$  value greater than 3.0 eV. However, only samples 7, 11, 12, 17, and 18 meet the thesis objectives by providing 78%, 75%, 81%, 75%, and 86% average light transmittance in the visible region, respectively. The comparison of the  $T_{vis}$  values of the samples in as-deposited state and after annealing in Ar or forming gas annealing are demonstrated in Figure 4.36 (c). As clearly seen from this image, the number of the samples with  $\geq 75\%$  average visible transmittance after Ar+4% H<sub>2</sub> annealing is less than the number of samples after Ar atmosphere annealing. At this point, it is worth to mention that only three samples (11, 14, and 19) were satisfied the objectives of this study after Ar annealing, whereas four samples (11, 12, 17, and 18) exhibited high transmittance and conductivity after forming gas annealing. No sample was satisfied the requirements

in the as-deposited state. This clearly indicates that the post-deposition annealing step improves the properties of the samples. On the other hand, the results imply that in terms of electrical conductivity the prominent compositions are In- and Zn-rich compositions, whereas for optical transparency Zn-rich samples are more convenient.

Table 4.15 Optical properties of a-ZITO films annealed in Ar+4% H<sub>2</sub> atmosphere for 1 h after being deposited at RT under 10 mTorr sputtering pressure for 45 min

Sample	$T_{vis}$ (%)	$E_g$ (eV)
1	56	2.75
2	58	2.86
3	58	2.84
4	62	2.90
5	60	2.93
6	59	2.90
7	78	3.34
8	61	3.04
9	58	2.95
10	50	2.98
11	75	3.20
12	81	3.28
13	50	2.80
14	54	3.06
15	6	1.91
16	40	3.18
17	75	3.22
18	86	3.25
19	63	3.30
20	18	2.49
21	2	1.48

As discussed above, Ar annealing produced better results than forming gas annealing in terms of optical properties. In contrast, Ar+4% H<sub>2</sub> annealing yielded samples with lower sheet resistance. Therefore, the samples were subjected to successive annealing in order to benefit from the advantage of Ar medium on optical properties as well as the favorable effect of Ar+4% H<sub>2</sub> medium on electrical properties. During this experiment, the thin films were loaded in an atmosphere-controlled furnace at RT and heated to 400 °C with a temperature increase of 2 °C/min under Ar+4% H<sub>2</sub> atmosphere, and first remained at this temperature for 1 h. Then, the furnace atmosphere was shifted to pure Ar and the samples kept under this gas for 1 h. The samples were cooled down to room temperature under flowing Ar gas. Digital images of these samples on the substrate holder is shown in Figure 4.37 (a). If the above-mentioned statement is followed, it can be seen visually that successive annealing improves transparency in all samples, with the exception of samples 15, 20, and 21.

Figure 4.37 (c) demonstrates the images of samples which showed profound change in their appearance with successive annealing. Among them, 11, 12, 17, and 18 appear quite transparent, with noticeable coloration for the samples in 11 and 17. In contrast to them, samples 12 and 18 looks better compared to their as-deposited state. Indeed, the optical property analyses presented below show that these two samples have  $T_{vis}$  values greater than 75%.

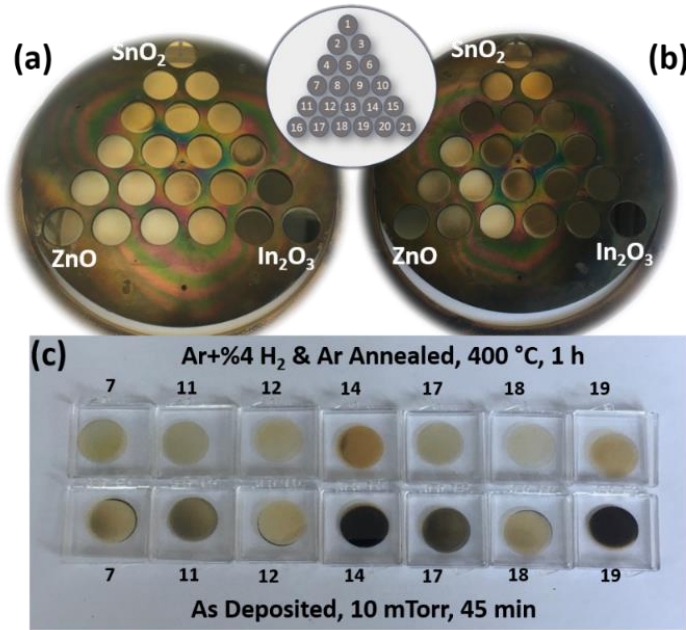


Figure 4.37 Digital images of a-ZITO thin films **a)** successively annealed in Ar+4% H<sub>2</sub> and Ar atmospheres for 1 h at 400 °C, **b)** in as-deposited state, **c)** samples with profound change in their transmittance after annealing.

As shown in Figure 4.38 (a), samples 12 and 18 were the first two samples which entering the shaded target region, and both thin films demonstrated 87 %  $T_{vis}$  in the 400-700 nm wavelength range. Apart from these two samples, none of other compositions provided an average of 75% visible light transmittance. The Tauc's plots of these samples are shown in Figure 4.38 (b), and the band gap energy values of all samples are listed in Figure 4.38. Most samples exhibited  $E_g$  values in the range of 2.5-3.0 eV. The following samples presented  $E_g$  values greater than 3.0 eV: 7, 10, 11, 12, 16, 17, and 18. These findings revealed that annealing in successive gas environments does not provide any advantage in terms of optical properties of a-ZITO thin films when compared to annealings under pure Ar or forming gas atmospheres.

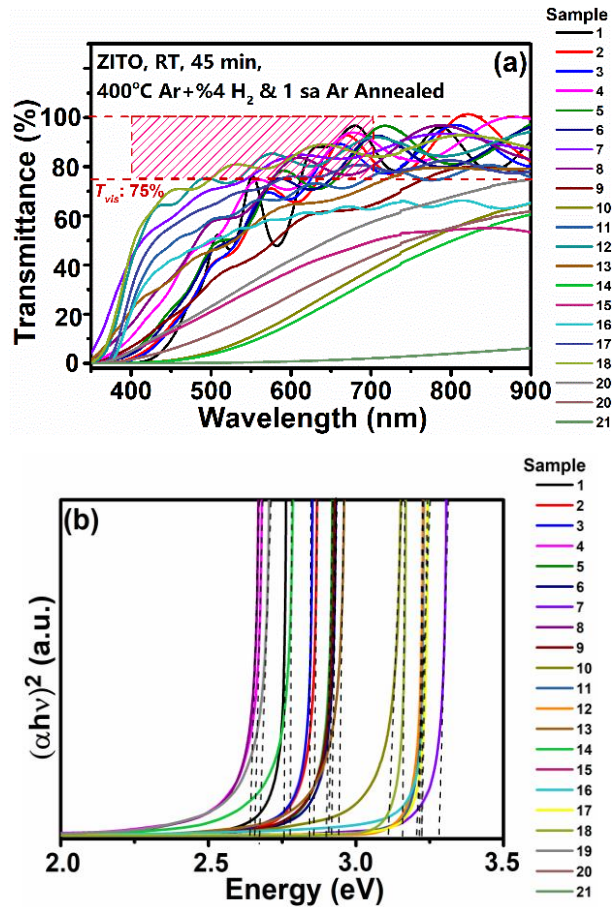


Figure 4.38 **a)** Transmittance spectra, **b)** Tauc's plots of a-ZITO thin films annealed successively in Ar+4% H<sub>2</sub> and Ar atmospheres for 1 h at 400 °C

Figure 4.39 (a) compares the sheet resistance values of successively annealed a-ZITO thin films with their  $R_s$  values in as-deposited state. As can be seen, electrical property of many samples can be improved via successive annealing process in forming gas and Ar atmospheres. The sheet resistance value of six samples (10, 11, 15, 17, 19, and 20) were measured to be lower than 100  $\Omega/\square$ . Apart from sample 10, all other samples already exhibited low sheet resistance values after annealed in pure Ar or Ar+4 % H<sub>2</sub> atmospheres. Further, none of these samples provide sufficient transparency in the visible region, Figure 4.39 (b). Moreover, the samples with high transparency (12 and 18) revealed sheet resistance values above 400  $\Omega/\square$ . Therefore, annealing of ZITO thin films in successive gas environments also does not provide

any advantage in terms of electrical properties when compared to annealings under pure Ar or forming gas atmospheres. As a result, it is not possible to conclude that successive annealing is an effective way to improve electrical and optical properties of the films simultaneously, under the experimental conditions applied.

Table 4.16 Optical properties of a-ZITO thin films annealed successively in Ar+4%H<sub>2</sub> and Ar atmospheres for 1 h at 400 °C

<b>Sample</b>	<b><math>T_{vis}</math> (%)</b>	<b><math>E_g</math> (eV)</b>
1	56	2.75
2	58	2.85
3	56	2.84
4	25	2.65
5	61	2.89
6	60	2.91
7	74	3.28
8	26	2.64
9	57	2.90
10	48	3.10
11	72	3.22
12	87	3.21
13	44	2.94
14	32	2.77
15	1	-
16	44	3.20
17	71	3.22
18	87	3.15
19	27	2.67
20	1	-
21	<1	-



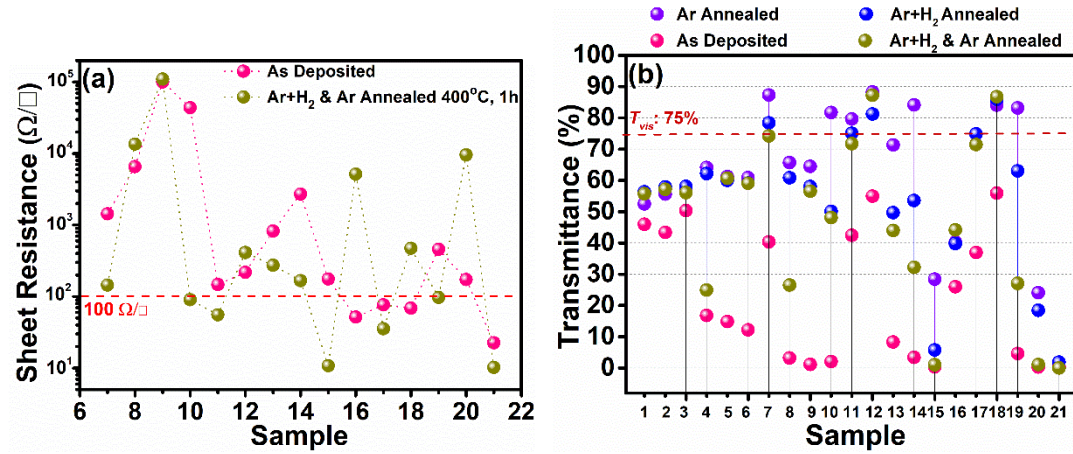


Figure 4.39 a) Sheet resistance of as-deposited (RT, 45 min), and annealed (successively in Ar+4 % H<sub>2</sub> and Ar for 1 h, 400 °C) a-ZITO thin films, b)  $T_{vis}$  values of as-deposited and annealed a-ZITO thin films (data for various annealing atmospheres denoted via different colored spheres)

Table 4.17 provides a useful view as a summary of the preceding studies conducted in this thesis until now and the basic criteria for the sample selection for further studies. Instead of giving all samples, the table contains only those that meet the optical requirements. Therefore, only the samples 7, 11, 12, 17, 18, and 19 are included in the table. Since none of the air atmosphere annealed samples were optically successful, they are not listed here. Highlights indicates the  $T_{vis}$  or  $R_s$  values of the samples which provided the objectives. Accordingly, none of the samples deposited at RT for 45 min at 10 mTorr Ar pressure could provide 75%  $T_{vis}$  limit. From an electrical perspective, sample 18 had the lowest sheet resistance with 68  $\Omega/\square$ , among the as-deposited samples.

After annealing under Ar, all samples have displayed  $T_{vis}$  values of  $\geq 80\%$ , with the exception of sample 17. The sample with the highest electrical conductivity was number 19 with a  $R_s$  of 69  $\Omega/\square$ . This thin film also exhibited 83%  $T_{vis}$  value. After Ar+4% H<sub>2</sub> annealing, 5 samples had  $T_{vis}$  values that are within the project's goal. Sample number 18 distinguishes from others when the lowest  $R_s$  value is considered along with high transparency ( $T_{vis} = 86\%$  and  $R_s = 46 \Omega/\square$ ). No samples were

provided both satisfactory optical and electrical property simultaneously as a result of successive annealing in Ar+4% H<sub>2</sub> and Ar atmospheres.

Table 4.17 Candidate samples for a-ZITO transparent heater production

Sample	7	11	12	17	18	19	
<b><math>T_{vis}</math> (%), As-deposited</b>	40	42	55	37	56	5	<b>RT</b>
<b><math>R_S</math> (<math>\Omega/\square</math>), As-deposited</b>	1433	146	218	76	68	458	
<b><math>T_{vis}</math> (%), Ar Annealed</b>	87	80	88	72	84	83	
<b><math>R_S</math> (<math>\Omega/\square</math>), Ar Annealed</b>	7982	84	4255	37	2508	69	
<b><math>T_{visr}</math> (%), Ar+%4 H<sub>2</sub> Annealed</b>	78	75	81	75	86	63	
<b><math>R_S</math> (<math>\Omega/\square</math>), Ar+%4 H<sub>2</sub> Annealed</b>	216	72	73	51	46	42	
<b><math>T_{vis}</math> (%), Ar+%4H<sub>2</sub> ve Ar Annealed</b>	74	72	87	71	87	27	
<b><math>R_S</math> (<math>\Omega/\square</math>), Ar+%4H<sub>2</sub> ve Ar Annealed</b>	145	55	412	35	471	97	
<b><math>T_{vis}</math> (%), As-deposited</b>	77	55	72	58	76	27	<b>250 °C</b>
<b><math>R_S</math> (<math>\Omega/\square</math>), As-deposited</b>	150	146	93	71	37	82	
<b><math>T_{vis}</math> (%), Ar ve Ar+%4H<sub>2</sub> Annealed</b>	73	61	76	67	78	32	
<b><math>R_S</math> (<math>\Omega/\square</math>), Ar ve Ar+%4H<sub>2</sub> Annealed</b>	147	72	74	36	46	42	

In case of the films deposited at a substrate temperature of 250 °C, the lowest sheet resistance (37  $\Omega/\square$ ) was provided with high enough (76%) average visible region transmittance by the sample 18. Further, after successive annealing under Ar+4% H<sub>2</sub>

and Ar atmospheres, the  $T_{vis}$  of this sample was increased to 78% at the expense of the sheet resistance. The value of  $R_s$  was increased to  $46 \Omega/\square$  after the annealing step. But yet, sample 18 is still the best among others after successive annealing in terms of optical and electrical properties.

According to the interpretations given above, it is concluded that the sample 18 provides the the most suitable composition for the objectives of this study. Therefore, the as-deposited state EDX data was obtained and used to determine the composition of this thin film sample.

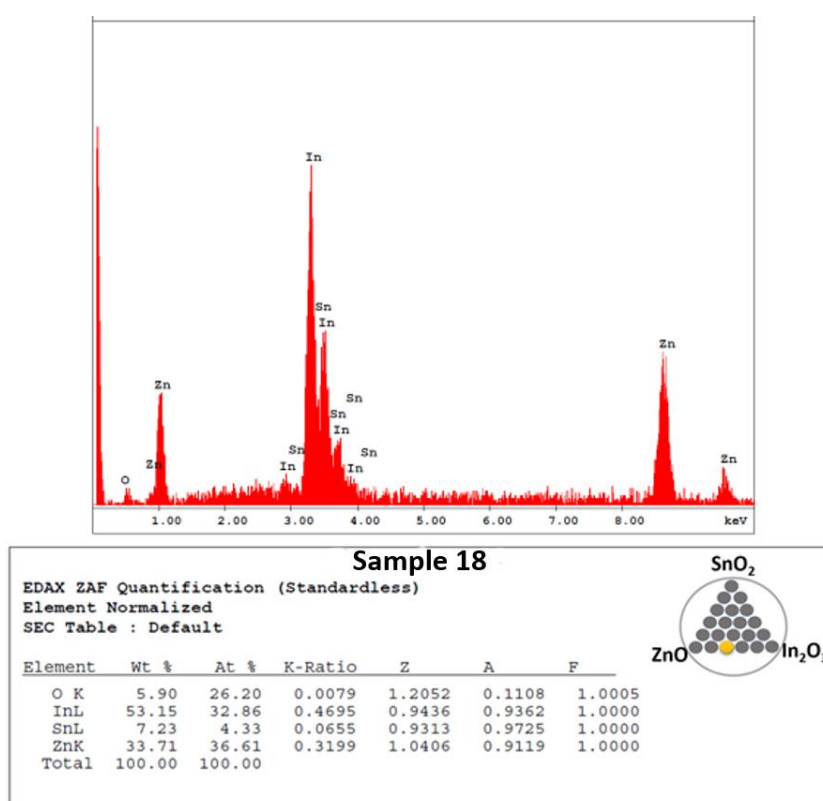


Figure 4.40 EDX spectrum and elemental composition of sample 18 (the sample was obtained under 10 mTorr sputtering pressure for 45 min and on substrates kept at RT)

The EDX spectrum of sample 18 is given in Figure 4.40. This spectrum demonstrates that the thin film is composed of In, Zn, Sn, and oxygen elements. In other words,

this thin film includes 33.71 wt.% Zn, 53.15 wt.% In, 7.23 wt.% Sn, and 5.9 wt.% oxygen. Based on a calculation that excludes the oxygen element, the cation ratios in the thin film are found to be 49.60 at.% Zn, 44.52 at.% In, and 5.86 at.% Sn. It is known that the composition of commercial ITO consists of 74 wt.% In, 18 wt.% O<sub>2</sub>, and 8 wt.% Sn. From this perspective, sample 18 includes ~21 wt.% less In in its composition when compared to commercial ITO.

#### **4.4 Production and characterization of a-ZITO transparent heaters**

In order to obtain the final a-ZITO transparent heaters, a 3" target was produced using high purity ZnO, In<sub>2</sub>O<sub>3</sub>, and SnO<sub>2</sub> powders based on the composition of sample 18 given above. This target material was used to deposit a-ZITO thin films on glass substrates with dimensions of 50 mm × 75 mm size. As described in Chapter 3, a-ZITO thin films were deposited at various substrate temperatures, i.e., RT, 150, and 250 °C. In the process, all depositions were continued to achieve a thin film thickness of 750 nm. Deposited samples were annealed under Ar+4% H<sub>2</sub> for 90 min at 400 °C. For other characterization purposes, samples were also reproduced on 18 mm diameter glass substrates.

##### **4.4.1 Visual examination**

Figure 4.41 (a) shows the digital images of a-ZITO thin films deposited on the substrates arranged on a multi-substrate carrier magazine. Unlike the previous examples obtained via the combinatorial approach, all of the samples in this case appear to be the same, since all 21 samples on the holder for each temperature have the same composition. Further, one can see that the deposition temperature does not lead significant difference between the samples in terms of appearance. For this reason, a-ZITO thin films were produced on larger substrates. Digital images of these samples are displayed on the left side in Figure 4.41 (b). It is seen that the films are quite transparent for all substrate temperatures. Among them, the one deposited at a

substrate temperature of 150 °C seem slightly better than others, i.e., particularly transparent and colorless. The right side of this image shows the appearance of these thin films after 90 min of annealing in Ar+4% H<sub>2</sub> atmosphere at 400 °C. These images clearly illustrate that annealing can entirely remove the partial coloration observed at the as-deposited samples. This further indicates that a-ZITO thin films with very high visible transmittance can be produced independent of substrate temperature.

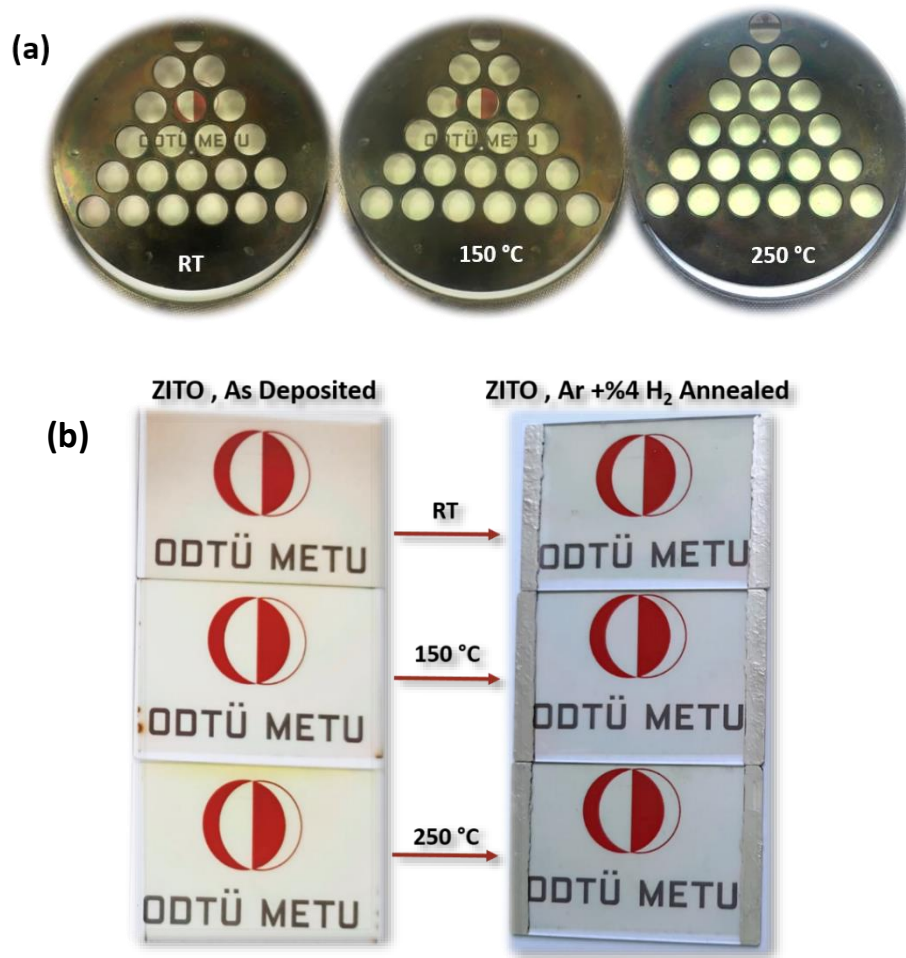


Figure 4.41 Digital images of a-ZITO thin films deposited at various substrate temperatures, **a)** on 18 mm diameter glass substrates **b)** on 5 cm x 7.5 cm glass substrates, left; as-deposited, right; after annealing under Ar+4% H<sub>2</sub> atmosphere for 1.5 h at 400 °C

#### 4.4.2 Structural examination

Figure 4.42 (a and b) shows the XRD patterns of a-ZITO thin films produced on glass substrates at RT, 150 °C, and 250 °C, and then annealed in Ar+4% H<sub>2</sub> atmosphere at 400 °C for 90 min., respectively. The patterns belong to as-deposited state of the samples indicate that all thin films, regardless of deposition temperature, were developed in amorphous structure. As a result, a low intensity and wide peak in the region of  $2\theta = 30\text{--}35^\circ$  are recorded in the patterns. Furthermore, the patterns shown in Figure 4.42 (b) shows that the amorphous structure can be preserved after annealing the thin films at 400 °C for 90 min.

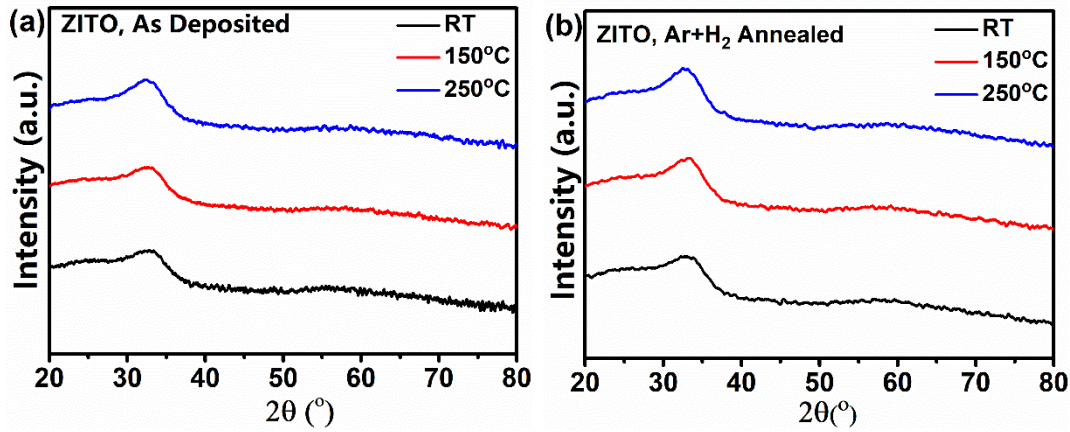


Figure 4.42 XRD patterns of a-ZITO thin films deposited on glass substrates at various temperatures **a)** as-deposited, **b)** after annealing in Ar+4% H<sub>2</sub> atmosphere at 400 °C for 90 min.

It is known that the grain boundaries in thin films of oxides such as In<sub>2</sub>O<sub>3</sub> or ZnO, have a negative effect on mobility due to charge scattering [110]. The absence of long-range order in amorphous materials eliminates the effect of grain boundaries on electrical properties, therefore, the charge carrier mobility can be expected to be quite high for the current a-ZITO thin films.

#### 4.4.3 Morphological examination

Figure 4.43 (a, c, and e) demonstrates high magnification surface SEM images of a-ZITO thin films deposited at RT, 150 °C, and 250 °C substrate temperatures, respectively. As can be seen from the scale bar given on lower right, these images were obtained from a relatively small area of the surface. The surfaces of the films are featureless in general. On the other hand, for the images of RT and 150 °C deposited thin films, in some regions, the surfaces exhibited hill-like protrusions. These hill-like formations are clearly seen in the 3D AFM surface topography images of these samples as given in Figure 4.44 (a and b). It is obvious that the hills are much smaller in diameter (up to 80 nm) in the RT deposited sample, but their frequency is high. On the other hand, for 150 °C deposited sample, their diameter can reach up to 300 nm, but they are more scattered. In addition, these topography images revealed that the height of these hill-like protrusions are not higher than 20-30 nm. While these thin films were obtained at relatively low substrate temperatures and under low diffusion conditions, these features may be formed during the nucleation stage and continue to grow for the entire deposition process due to shadowing effect. Because the sample surface deposited at 250 °C is free from these formations, see Figure 4.44 (c).

The inset SEM images in Figure 4.43 (a,c, and d) were obtained from a much larger area on the surfaces of these thin films and shows that a-ZITO samples can be deposited with high homogeneity and without any cracks, voids, and so on. Further, AFM measurements revealed that the surface with highest roughness was obtained in the sample deposited at 150 °C with an RMS value of 3.12 nm. In contrast, the surface with lowest roughness was formed in the thin film deposited at 250 °C. The RMS value of this sample was calculated to be 0.453 nm. And finally, RMS value was measured as 1.83 nm for the sample deposited at RT. The surface roughness of glass substrates used here is ~2 nm. This shows that, a-ZITO thin films can be obtained with much lower roughness when compared to that of sputtered AZO/SiO<sub>2</sub> thin films.



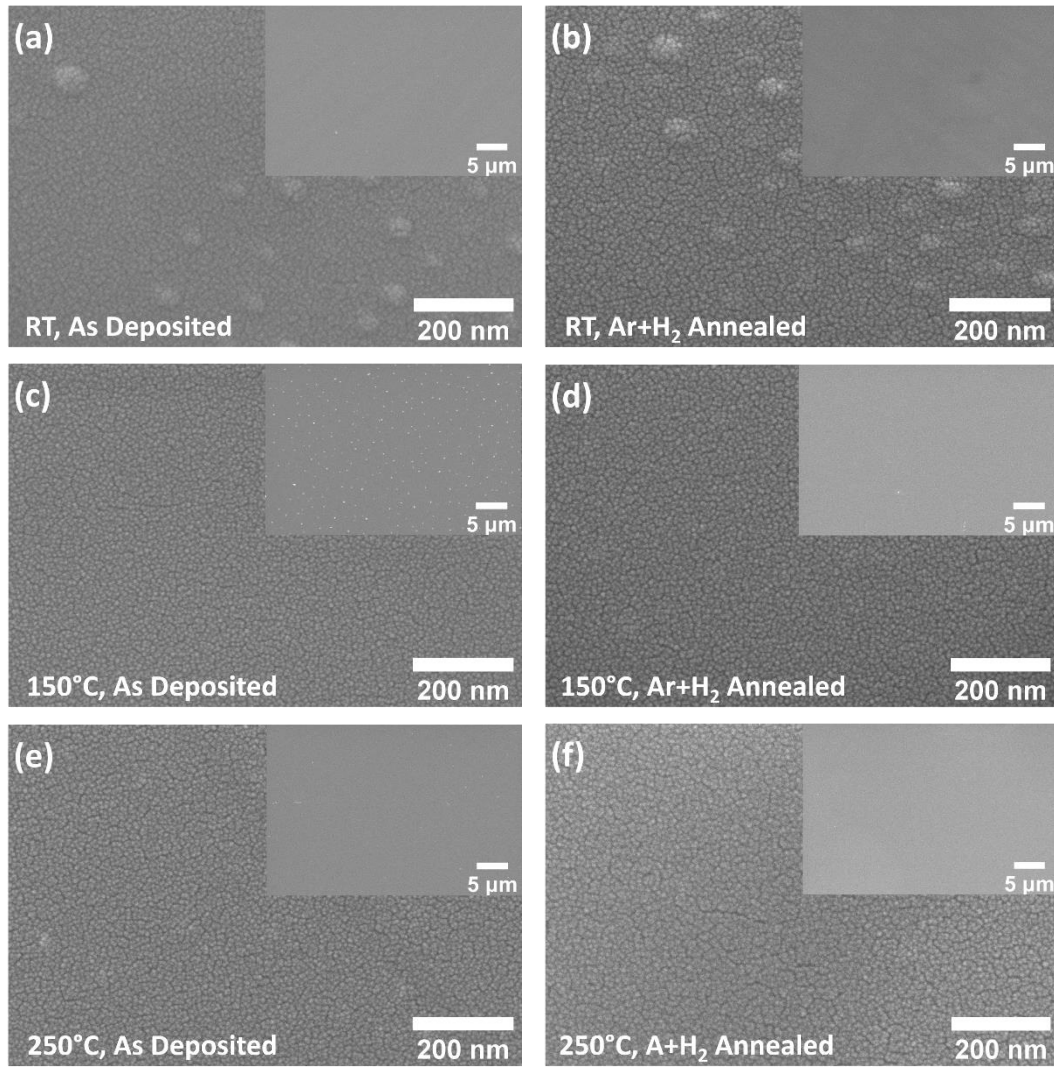


Figure 4.43 Surface SEM images of a-ZITO thin films produced at various substrate temperatures, as-deposited **a)** RT, **c)** 150 °C, **e)** 250 °C, after annealing in Ar+4% H<sub>2</sub> atmosphere at 400 °C for 90 min. **b)** RT, **d)** 150 °C, **f)** 250 °C (inset images provide general view for the surfaces)

Figure 4.43 (b, d, and f) shows the surface SEM images of RT, 150 °C, and 250 °C deposited a-ZITO thin films, respectively, after annealing in Ar+4 % H<sub>2</sub> atmosphere for 90 min at 400 °C. It is clear from these images that the annealing process led to coarsening of the surface of the films, regardless of the initial deposition temperature. This phenomenon is most noticeable in the annealed surface image of the film deposited at RT. In this SEM image, the surface can be seen in relatively higher



detail than the as-deposited surface. On the other hand, the inset images given in each figure reveals that the thin films have remarkably homogenous surfaces, after annealing.

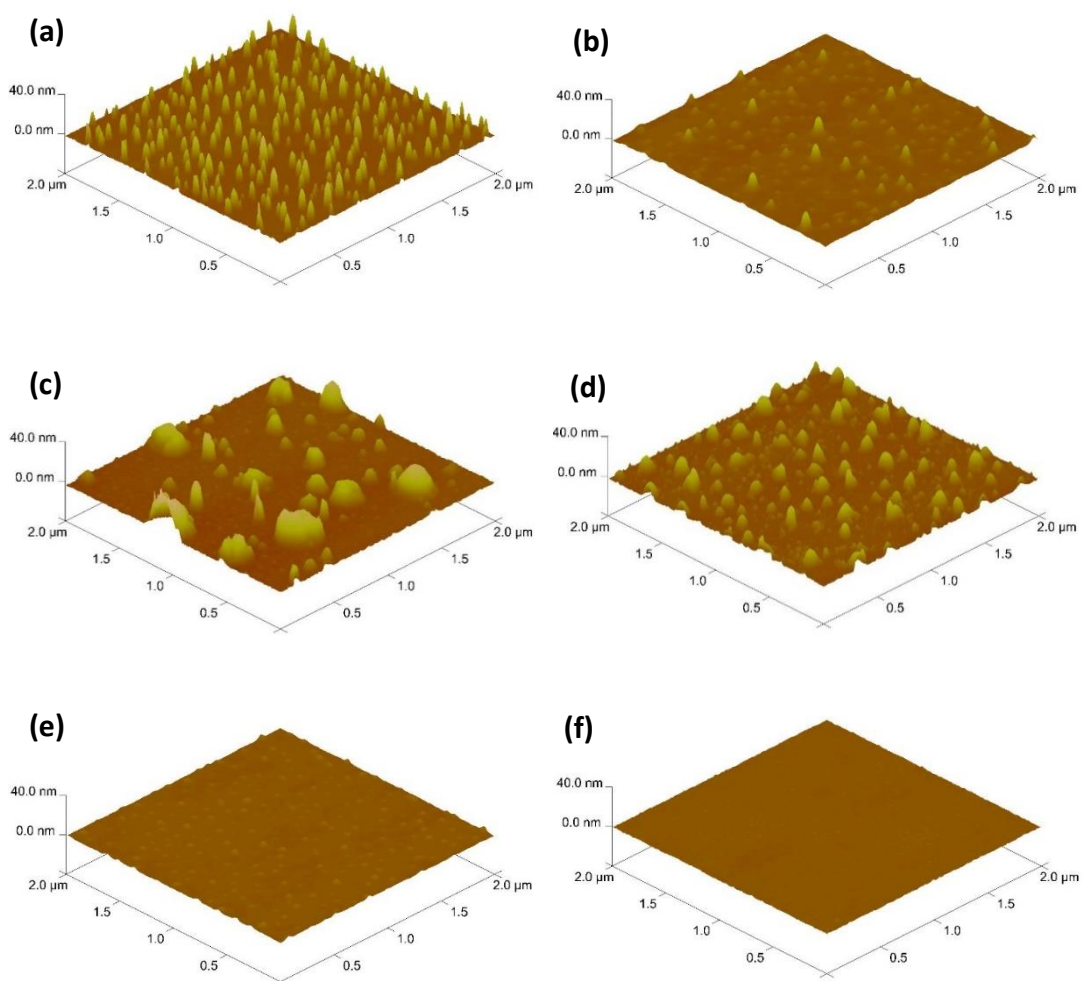


Figure 4.44 3D AFM images of a-ZITO thin films produced at various substrate temperatures, as-deposited **a)** RT, **c)** 150 °C, **e)** 250 °C, after annealing in Ar+4% H<sub>2</sub> atmosphere at 400 °C for 90 min. **b)** RT, **d)** 150 °C, **f)** 250 °C

AFM measurements showed that the surface roughness could be reduced at approximately 50% for all samples after annealing. This can clearly be seen by comparing the AFM topographies images of the samples given in Figure 4.44 (b, d,

and e) with their topography in as-deposited state. Annealing reduced the number of protrusions significantly for RT deposited sample, whereas for 150 °C deposited thin film, the sizes of these hill-like features decreased. This is probably due to effect of high temperature used during annealing which allows the formation of surface reactions. The RMS values of a-ZITO thin films after annealing were found to be 0.808, 1.98 and 0.294 nm over a surface area of 2  $\mu\text{m}$  x 2  $\mu\text{m}$ , respectively for RT, 150 °C, and 250 °C deposited samples.

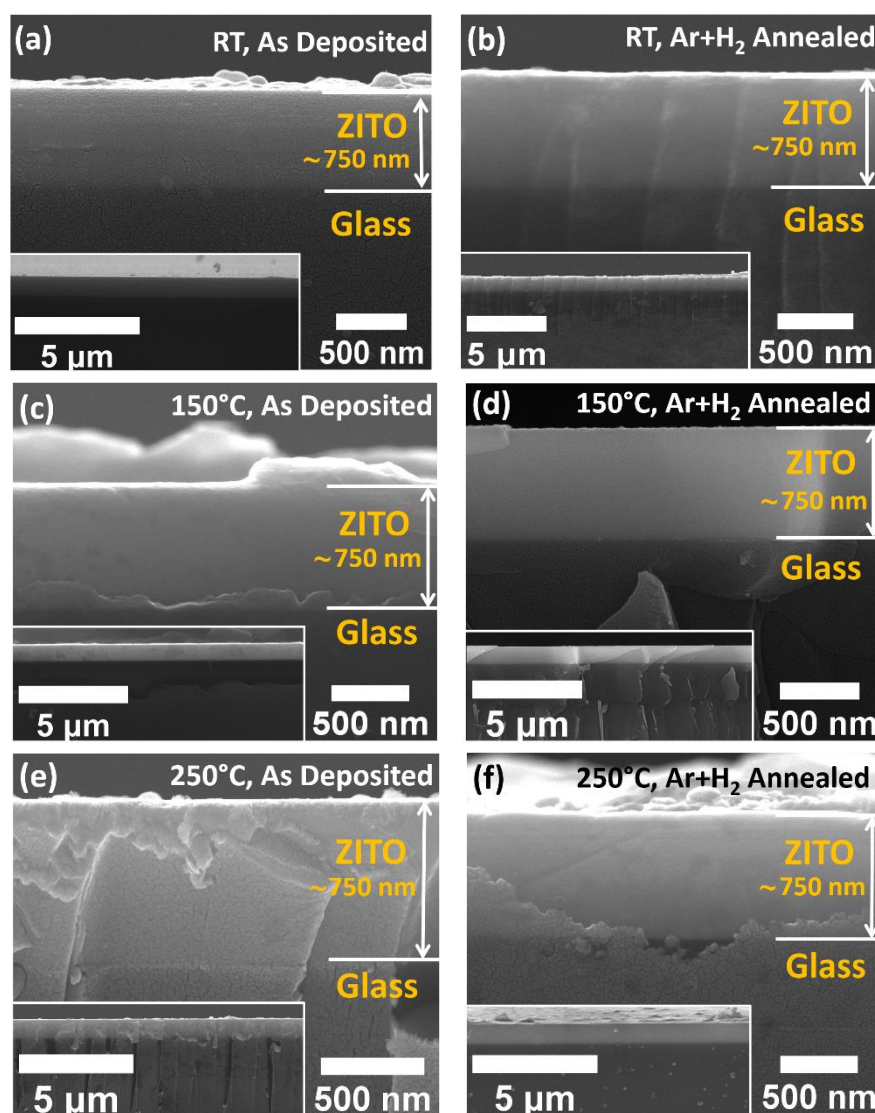


Figure 4.45 Through thickness fracture surface SEM images of a-ZITO thin films produced at various substrate temperatures, as-deposited **a)** RT, **c)** 150 °C, **e)** 250 °C, after annealing in Ar+4% H<sub>2</sub> atmosphere at 400 °C for 90 min. **b)** RT, **d)** 150 °C, **f)** 250 °C. (inset images provide general views of the surfaces)

Figure 4.45 (a, c, and e) demonstrates high magnification cross-sectional SEM images of a-ZITO thin films deposited at RT, 150 °C, and 250 °C substrate temperatures, respectively. It is seen that the films almost exhibit the same thickness for all deposition temperatures. This is achieved via the tuning of the deposition rates. The annealed cross-section images are given in Figure 4.45 (b, d, and f). Similar to the SEM surface images given above, the cross-sections of both as-deposited and annealed thin films present no recognizable features, due to amorphous nature. The inset images given in each figure indicate that all samples were deposited with uniform thickness and without any peeling from the substrate even after moderately high temperature annealing.

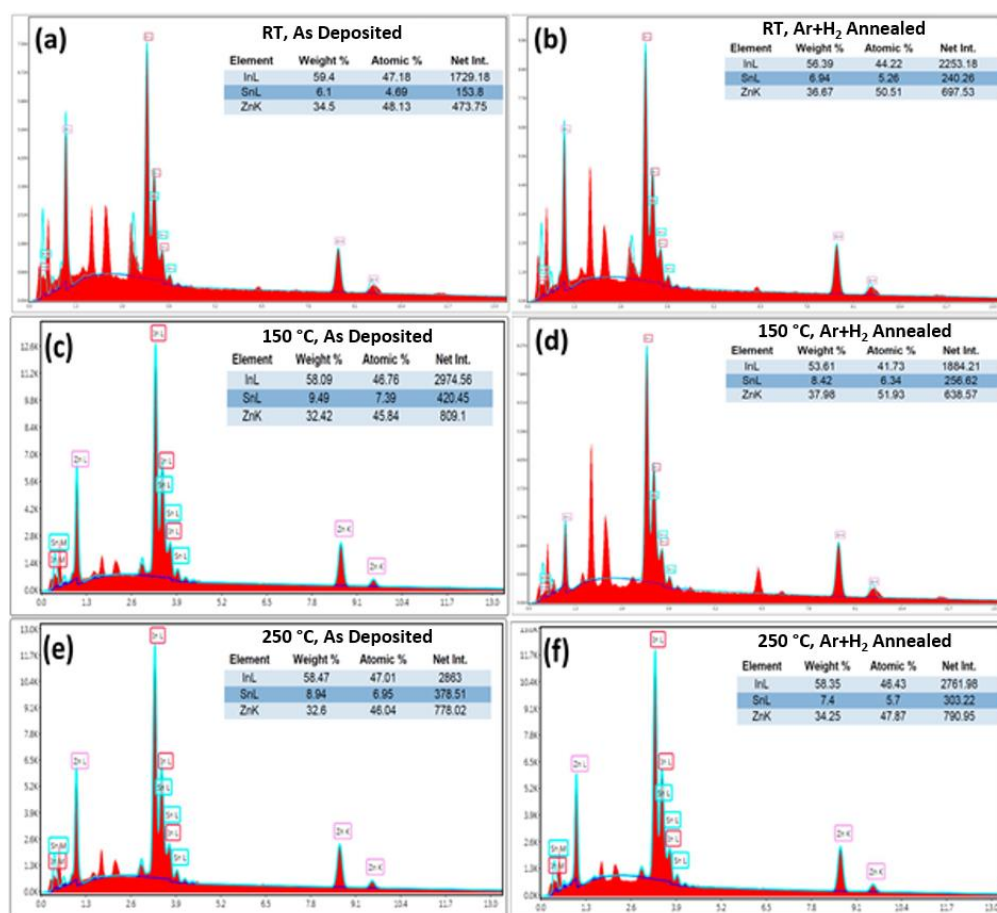


Figure 4.46 EDX analyses of a-ZITO thin films produced at various substrate temperatures, as deposited at **a)** RT, **c)** 150 °C, **e)** 250 °C, after annealing in Ar+4% H<sub>2</sub> atmosphere at 400 °C for 90 min (The inset tables denote the elemental ratio of the cations present in the samples)

As mentioned above, these a-ZITO samples were produced using a 3” sputtering target where its composition was based on sample 18. As to remind, the composition of sample 18 was determined as 44.52 at. % In, 5.86 at.% Sn, and 49.60 at.% Zn by EDX. The composition of the thin films produced from this target was also characterized via EDX and the results are presented in Figure 4.46 (a, c, and e) for the as-deposited and in Figure 4.46 (b, d, and f) for the annealed samples. EDX analyses of the deposited thin films reveal that the compositions are enriched by In, in comparison to the target’s composition. The amount of In in the thin film samples was found to be around 47 at. % for all three substrate temperatures. Further, there are 1-2 at.% interchangings between the quantity of Sn and Zn with changing substrate temperature. Following annealing, the atomic composition of the films approached to the desired composition and enriched in terms of element Zn for all substrate temperatures. This indicates that the annealing process provides an atomic distribution in the film that is relatively close to the desired ratios. At this point, it is important to point out that the difference in the atomic composition of the films with respect to the target or each other are in the limit of the measurement error of EDX. Therefore, practically, it can be stated that the a-ZITO samples produced at various substrate temperatures exhibited almost the same composition with the target material.

#### **4.4.4 Optical analysis of a-ZITO thin films**

Optical properties of a-ZITO thin films were investigated by UV-Vis and UV-Vis-NIR spectrophotometers. Figure 4.47 (a) shows the transmittance spectra of a-ZITO thin films deposited at substrate temperatures of RT, 150 °C, and 250 °C. As seen in the figure, regardless of the substrate temperature, all thin films exhibited very high transmittance in the visible region.  $T_{vis}$  values were calculated as 82.53 %, 85.96 %, and 84.08 % for the thin film samples deposited at RT, 150 °C, and 250 °C, respectively. In the same order, the films exhibited 75% transparency at wavelengths of 441, 437, and 434 nm. This implies a slight shift towards lower wavelengths with

increasing deposition temperature. The lowest absorption edge among these thin films was recorded as 371 nm for the sample deposited at a substrate temperature of 150 °C. Accordingly, the band gap values of a-ZITO thin films were found to be 3.13 eV, 3.17 eV, and 3.09 eV, as shown in Figure 4.47 (b). Therefore, a linear relationship could not be established between the average visible region transmittance, band gap energies and substrate temperatures for a-ZITO thin films. Although the samples produced at different substrate temperatures showed similar optical transmittance behaviour, the one deposited at 150 °C substrate temperature presented the highest values ( $T_{vis}$ =85.96 %,  $T_{550}$ =90 %).

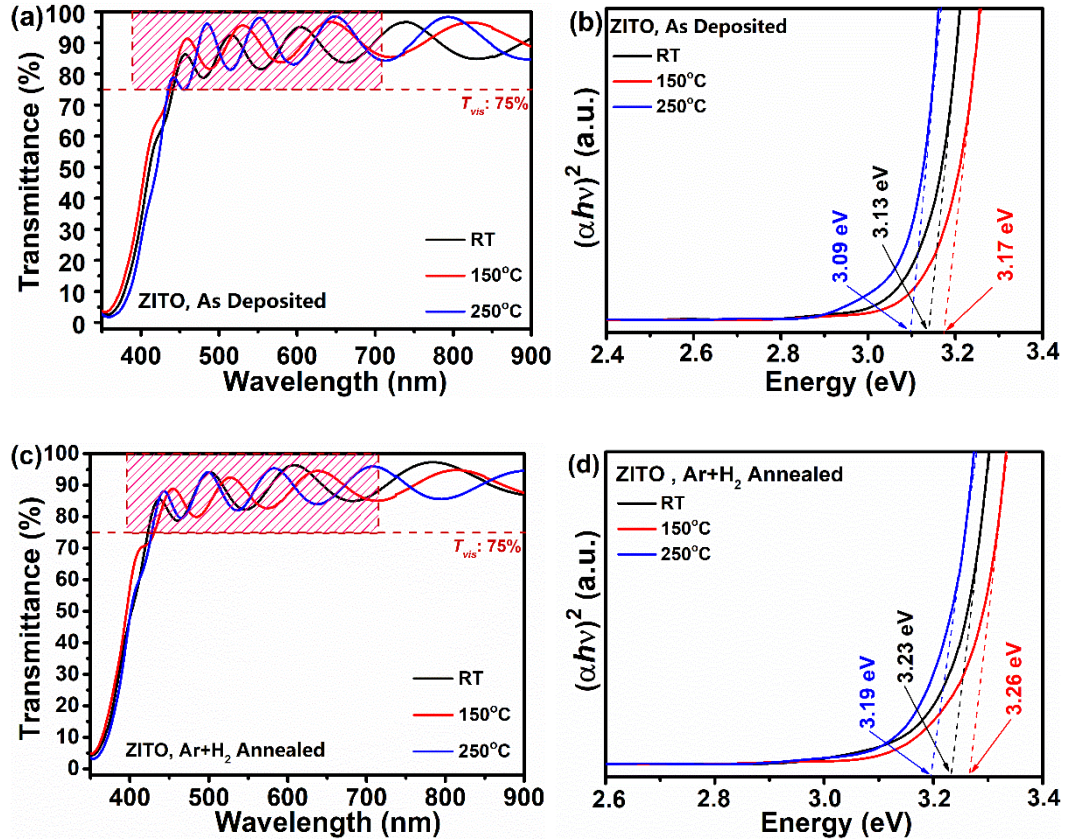


Figure 4.47 Transmittance spectra and Tauc's plots of a-ZITO thin films produced at various substrate temperatures, **a)** and **b)** as-deposited, **c)** and **d)** after annealing in Ar+4% H<sub>2</sub> atmosphere at 400 °C for 90 min (the inset numerical values given in (b) and (d) denotes the band gap values of the corresponding samples).



Figure 4.47 (c) shows the transmittance spectra corresponding to a-ZITO thin films after annealing in Ar+4% H<sub>2</sub> atmosphere for 90 min at 400 °C.  $T_{vis}$  values of 85.60 %, 85.60 %, and 85.50 % were calculated for thin films deposited at RT, 150 °C, and 250 °C, respectively. This implies that annealing under forming gas does not led a significant improvement in the optical transmittance of the samples, as expected. On the other hand, annealing induced a blue-shift of the absorption edge for all thin films and further, band gaps of all samples were widened ~0.1 eV. Therefore, the films satisfy the minimum transmittance of 75% at lower wavelengths when compared to their as-deposited states. It is found that the transmittance reached to shaded are at 423 nm, 433 nm, and 428 nm, in accordance with the increasing substrate temperature.

These findings indicate that a-ZITO thin films produced at different substrate temperatures are qualified enough to satisfy the current study's optical transmittance goal. Furthermore, these findings demonstrate that the optical properties of the films produced from a single source, result in significantly different values than those produced from three separate sources (i.e., In<sub>2</sub>O<sub>3</sub>, SnO<sub>2</sub>, and ZnO).

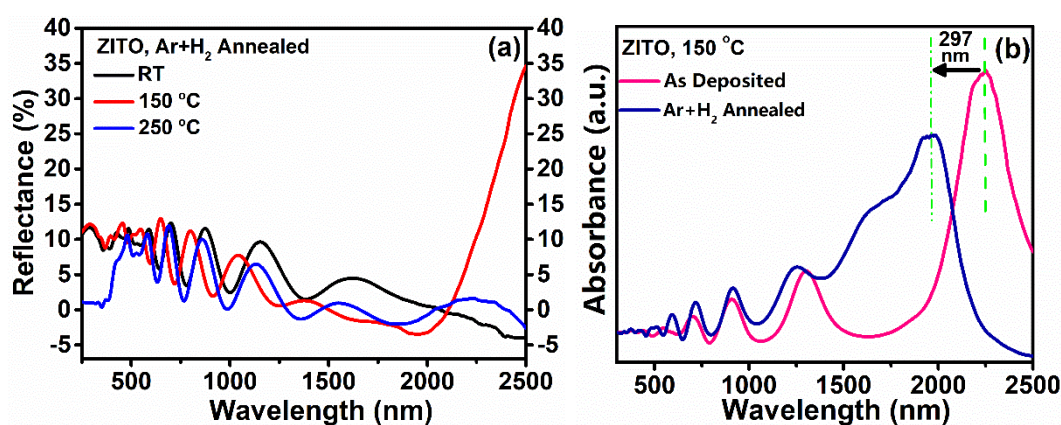


Figure 4.48 **a)** Reflectance spectra, and **b)** absorption spectra of a-ZITO thin films deposited at 150 °C substrate temperature and annealed at 400 °C Ar+4% H<sub>2</sub> for 90 min

Figure 4.48 (a) shows the reflectance spectra of a-ZITO thin films after annealing in Ar+4 % H<sub>2</sub> atmosphere for 90 min at 400 °C. The figure comprises the spectra of RT, 150 °C, and 250 °C substrate temperatures. The results were recorded up to a wavelength of 2500 nm. As seen from these spectra, samples deposited at RT and 250 °C did not show any noticeable reflectance in the wavelength range considered. On the other hand, the reflectance of 150 °C deposited sample exhibited an increase in the near infrared region. After the sample showed a minimum of around 3% at 1956 nm, its reflectance increased rapidly with increasing wavelength. At the targeted wavelength of 2.5 μm, the value reached ~35%. This value is significantly greater than the reflectance value presented by as-deposited AZO thin films, but it is almost half of that exhibited by annealed AZO/SiO<sub>2</sub>. Since the reflectivity in the IR region is primarily determined by the charge carrier concentration and their mobility, and because the carrier concentrations of both as-deposited and annealed a-ZITO thin films are probably lower than that of annealed AZO thin films, it is not surprising that the reflectance is lower for the former.

Absorption spectra of 150 °C deposited sample are given in Figure 4.48 (b) for as-deposited and annealed states. In accordance with high optical transmittance, the sample exhibits low absorbance in the visible region in both states. On the other hand, as-deposited sample presented a significant absorbance peak extending from 1700 nm to wavelengths beyond 2500 nm. Therefore, this sample showed a very low reflectance (less than 10 %, the data is not shown here) value at the wavelength of 2.5 μm. After annealing, however, the intensity of this absorbance peak decreased while its width is increased. The center of the peak was shifted ~300 nm to lower wavelengths and located at 1952 nm. As can be seen from Figure 4.48 (a), the reflectance of the sample is at its minimum at around this wavelength and then started to increase suddenly with the decreasing absorbance at higher wavelengths. This also indicates that the plasma wavelength of this sample could be shifted towards the visible region as result of annealing.

#### 4.4.5 Electrical analysis of a-ZITO thin films

The electrical properties of a-ZITO thin films were determined by Hall effect measurements, in as-deposited state and after annealing under Ar+4% H<sub>2</sub> atmosphere for 90 min at 400 °C. I-V measurements were carried out at RT using Van der Pauw geometry and 10 mA current and were repeated three times. The results are listed in Table 4.18. Figure 4.49 (a and b) emphasizes the average of the sheet resistance and resistivity values obtained from these measurements. As clearly seen from the data points given in this figure, the thin film deposited at 150 °C exhibited the lowest sheet resistance among all samples, with  $R_s$  of 24.23  $\Omega/\square$ . The resistivity of this sample was determined as  $\rho = 17.93 \times 10^{-4} \Omega \cdot \text{cm}$ . Further, the carrier concentration and carrier mobility values were measured as  $\eta = 0.0828 \times 10^{21} \text{ cm}^{-3}$  and  $\mu = 42.01 \text{ cm}^2/\text{Vs}$ , respectively. The film deposited at 250 °C exhibited slightly higher mobility ( $\mu = 44.56 \text{ cm}^2/\text{Vs}$ ), although its carrier concentration ( $\eta = 0.0457 \times 10^{21} \text{ cm}^{-3}$ ) is about the half of that deposited at 150 °C. As a result, the sheet resistance ( $R_s = 41.41 \Omega/\square$ ) of 250 °C deposited sample was obtained almost twice as high compared to one deposited at 150 °C. The RT produced sample has both lower mobility ( $\mu = 36.77 \text{ cm}^2/\text{Vs}$ ) and slightly lower carrier concentration ( $\eta = 0.0764 \times 10^{21} \text{ cm}^{-3}$ ) compared to the thin film deposited at 150 °C. Accordingly, its sheet resistance was measured to be  $R_s = 30 \Omega/\square$ .

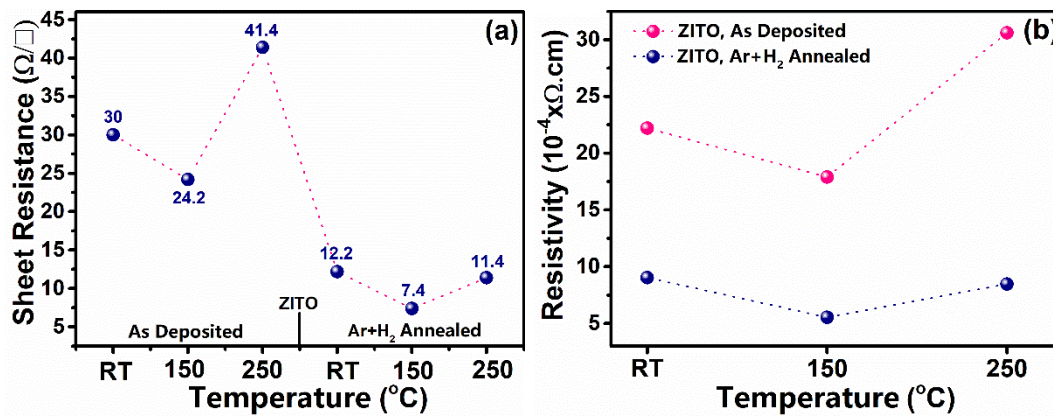


Figure 4.49 Electrical properties of a-ZITO thin films as a function of substrate temperature a) Sheet resistance and b) resistivity values of the films in as-deposited state and after annealing for 90 min at 400 °C in Ar+4 % H<sub>2</sub> atmosphere.



As proved by the XRD measurements, all ZITO thin films were obtained in amorphous structure, regardless of the employed substrate temperature. And this was maintained after annealing at moderately high temperatures. It is known that the absence of grain boundaries or long-range ordering in amorphous materials contributes to increases the charge carrier mobility [100]. The conduction band minimum in amorphous oxides is composed of spherically expanded orbitals of metal atoms and overlapping of these orbitals with neighboring metal orbitals does not result in a significant change. Therefore, since the conduction band minimum is unaffected by local bond stresses in these materials, electron transport can occur if the mobility is high [98], [160], [161]. The mobility values given in Table 4.18 for the as-deposited thin films were quite high, confirming these statements. Further, mobility values achieved here vary between 36 to 44 cm<sup>2</sup>/V s depending on the substrate temperature, which is almost over twice the value of  $\mu = 20.47$  cm<sup>2</sup>/V s, that obtained for the annealed AZO thin films.

As can be seen from Figure 4.49 and Table 4.18, after annealing under Ar+4% H<sub>2</sub>, the sheet resistance of all samples is improved. The  $R_s$  of as-deposited thin films were changed from 30  $\Omega/\square$  to 12.21  $\Omega/\square$  for RT deposited, from 24.23  $\Omega/\square$  to 7.49  $\Omega/\square$  for 150 °C deposited, and from 41.41  $\Omega/\square$  to 11.45  $\Omega/\square$  for 250 °C deposited sample. Although the film deposited at a substrate temperature of 150 °C exhibited the lowest sheet resistance after annealing, the highest improvement was obtained for 250 °C deposited sample with a reduction of 3.6-fold in its sheet resistance compared to as-deposited resistance. On the other hand, the electrical conductivities of these samples were calculated as 1106, 1805 and 1180 S/cm, respectively. Accordingly, the FOM values of RT, 150 °C, and 250 °C deposited a-ZITO thin films were obtained as  $11.79 \times 10^{-3}$ ,  $34.21 \times 10^{-3}$ , and  $17.35 \times 10^{-3} \Omega^{-1}$ , respectively.

Table 4.18 Hall effect measurement results for a-ZITO thin films deposited at various substrate temperatures and after annealing for 90 min at 400 °C in Ar+4 % H<sub>2</sub> atmosphere.

Sample		$\rho \cdot 10^{-4}$ ( $\Omega$ cm)	$R_s$ ( $\Omega/\square$ )	$\eta \cdot 10^{21}$ (cm <sup>-3</sup> )	$\mu$ (cm <sup>2</sup> /V s)
As-deposited	RT	22.2029	30.003	0.07642	36.787
		22.2027	30.003	0.07647	36.765
		22.2026	30.003	0.07645	36.774
	150 °C	17.9328	24.233	0.08285	42.012
		17.9325	24.233	0.08284	42.015
		17.9323	24.232	0.08284	42.016
	250 °C	30.6582	41.430	0.04564	44.608
		30.6437	41.409	0.04573	44.536
		30.6428	41.410	0.04572	44.548
Ar+4 % H <sub>2</sub> Annealed, 400 °C, 90 min	RT	9.0421	12.219	0.1766	39.089
		9.0422	12.219	0.1766	39.088
		9.0409	12.217	0.1767	39.053
	150 °C	5.5466	7.495	0.3076	36.580
		5.5466	7.495	0.3074	36.609
		5.5465	7.495	0.3075	36.596
	250 °C	8.4743	11.451	0.2100	35.068
		8.4743	11.451	0.2100	35.060
		8.4741	11.451	0.2101	35.053

The Hall effect measurements revealed n-type conductivity for the produced a-ZITO thin films. Therefore, the conductivity in these samples depends on the charge of an electron, carrier concentration, and mobility. As seen from the listed values in Table 4.18, the carrier concentration of as-deposited thin films was measured as  $0.0764 \times 10^{21}$ ,  $0.0828 \times 10^{21}$ , and  $0.0457 \times 10^{21}$  cm<sup>-3</sup> for the films deposited at RT, 150 °C, and 250 °C, respectively.

On the other hand, the highest carrier concentration after the annealing process was obtained as  $0.307 \times 10^{21}$  cm<sup>-3</sup>, for the sample deposited at 150 °C substrate temperature. This value is almost 2 and 1.5 times higher than that of RT ( $0.176 \times 10^{21}$ ) and 250 °C ( $0.21 \times 10^{21}$ ) deposited samples, respectively. The carrier mobility of as-

deposited thin films was measured as 36.775, 42.014, and 44.564 cm<sup>2</sup>/Vs for the films deposited at RT, 150 °C, and 250 °C, respectively. After annealing, the carrier mobility of these thin films was changed to 39.07, 36.54, and 35.06 cm<sup>2</sup>/Vs, as in the same order for the employed substrate temperatures. This indicates a slight increase in the carrier mobility of RT deposited sample after annealing. On the contrary, the carrier mobility of 150 °C and 250 °C deposited thin films were reduced 13% and 20%, respectively, as compared to their mobility values in the as-deposited state. One can see that for the as-deposited thin films, the carrier mobility increased with the increasing substrate temperature. On the other hand, this is not the case for carrier concentration. The carrier mobility first slightly increase with the increase of substrate temperature from RT to 150 °C, but then significantly decrease for 250 °C. This might be attributed to partial relaxation of the amorphous structure with the increasing substrate temperature. Therefore, similar to the increase of mobility with the increasing substrate temperature under high vacuum conditions ( $P_{O_2} \cong 0$ ), the increase in the mobility of RT deposited sample after annealing ( $P_{O_2} \cong 0$ ) can be expected. However, the observed decrease in the mobility of other samples after annealing, indicates that the improvement of the electrical conductivity with annealing mostly depends on the increase of carrier concentrations instead the change in the carrier mobility of the samples. Ndione et al., (2016) stated that the electrical conductivity in amorphous In-Zn-Sn-oxide thin films depends on the cation composition and partial pressure of oxygen during sputter deposition. In the current study, all thin film samples were deposited under the same conditions from a single target and annealed under identical conditions. If the small differences in the elemental composition of the films that determined by EDX is ignored, it is clear that the conductivity of these thin films depends on the employed substrate temperature and carrier concentration of the samples. It is known that the electrical conductivity of amorphous thin films composed of different cations depends on the atomic substitution induced electron/hole formation and oxygen vacancies [100], [160], [162]. For the current study, deposition under high purity Ar atmosphere on substrates held at various temperatures probably effects the number of successful

atomic substitutions and the concentration of oxygen vacancies in the bulk or surface of the films. Further, annealing in reducing atmosphere at moderately high temperatures modify the concentration of donors and oxygen vacancies and also doping of hydrogen to the structure which provides free electrons to contribute conductivity [98]. Moreover, the energy provided by annealing, probably induce the rearrangement of amorphous structure through the diffusion of oxygen [163]. This reduced the inordered distribution of charge density to the structure and suppress the strongly localized defects. As a result, the carrier concentration of all samples was improved after annealing. For the current study, the highest increase in carrier concentration and also the highest decrease in mobility was recorded for the sample deposited at 250 °C, after annealing. Due to inverse relationship between them, the observed decrease in mobility after annealing is not surprising. In amorphous oxides, mobility is effected from a variety of local or mid-range structural properties [164], such as the difference between the bond strength of In-O, Zn-O, and Sn-O, the modification of metal-oxygen coordinations and distortions in the metal-oxygen polyhedras, the formation of InO<sub>6</sub>-SnO<sub>6</sub> chains and random distribution of ZnO<sub>4</sub>. Therefore, the statements given above on the difference or the change of the electrical properties of a-ZITO thin films depends on the current experimental observations and literature data and requires more detailed characterization to be proven.

The reported data up to this point clearly imply that among others the sample produced at 150 °C is more suitable for the objectives of this thesis study in terms of visible light transmittance, near IR reflectivity, and electrical conductivity.

#### **4.4.6 Electro-thermal analysis of a-ZITO thin films**

The heating behavior and de-icing capacity of a-ZITO thin films deposited at various substrate temperatures were investigated by electro-thermal property measurements. The tests were conducted on samples with 50 mm x 75 mm dimensions. The response time, saturation surface temperature, stability, recyclability, and thermal resistance

of the heaters were determined using the samples kept at ambient temperature and by applying 3, 6, 9, and 12 V.

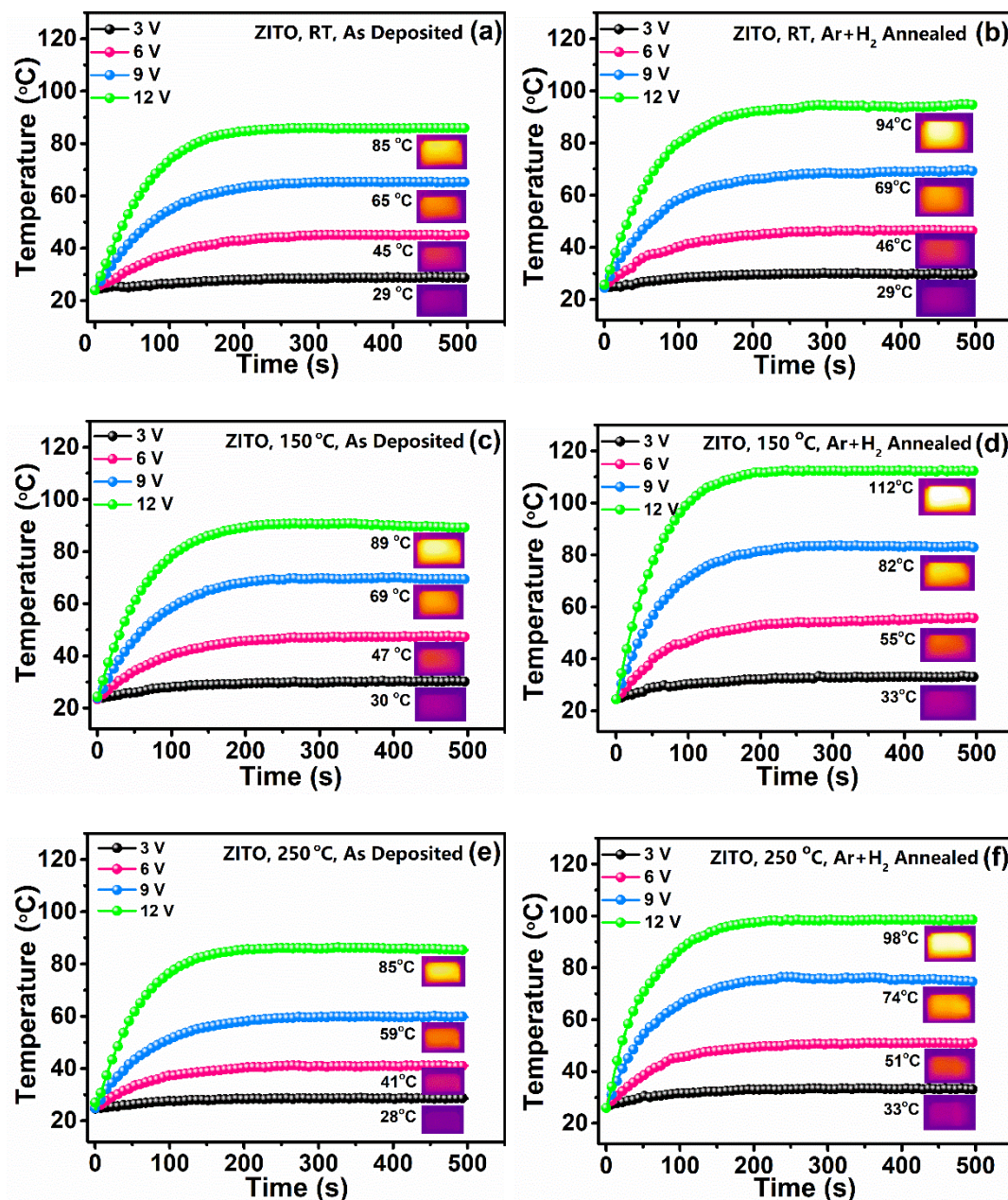


Figure 4.50 Heating behaviour of a-ZITO transparent heaters as a function of applied voltage **a)** RT deposited, **b)** annealed, **c)** 150 °C deposited, **d)** annealed, **e)** 250 °C deposited, **f)** annealed (annealing was performed at 400 °C for 90 min under Ar+4% H<sub>2</sub> atmosphere, the inset images given in each figure refers to the thermal camera image of the sample at the corresponding saturation temperature)

Figure 4.50 displays the heating behavior of a-ZITO thin films as a function of input voltage. The heating curves of as-deposited thin films are given in Figure 4.50 (a, c, and e). As seen from these curves, the saturation temperature increases with increasing supply voltage for all samples. As previously indicated, the mentioned temperature values are the average temperature of the entire surface, excluding the Ag-electrodes. Surface temperatures were recorded as 29, 45, 65, and 85 °C in case of applying 3, 6, 9, and 12 V, respectively, to the RT deposited sample. The transparent heater showed a linear response to input voltages over 3 V, such that the surface saturation temperature increased by 20 °C with every 3 V increment. This reveals that the achieved maximum temperature is depending on the supplied electrical power. For 150 °C deposited a-ZITO transparent heater, the surface saturation temperatures can be listed as 30, 47, 69 and 89 °C with the increasing voltage, Figure 4.50 (c). Similarly, 28, 41, 59, and 85 °C were measured for 250 °C deposited sample by applying 3, 6, 9, and 12 V, respectively.

Figure 4.50 (b, d and f) shows the heating behavior of these a-ZITO transparent heaters after annealing at 400 °C in Ar+4 %H<sub>2</sub> atmosphere for 90 min. Similar to the tests conducted with the as-deposited samples, here the heaters were subjected to input voltages of 3, 6, 9, and 12 V. In the order of increasing voltage input, saturation temperatures of 29, 46, 69, and 94 °C for RT deposited, 33, 55, 82, and 112 °C for 150 °C deposited, and 33, 51, 74, and 98 °C for 250 °C deposited sample were recorded. These results showed that annealing improves the heating behaviour of the samples, as expected. As observed for as-deposited samples, the film deposited at 150 °C substrate temperature exhibited the best heating performance among others, after annealing. The response time of this transparent heater in case of 6, 9, and 12 V inputs were recorded as 124, 114, and 102 s, respectively. As compared to the reported values previously for the response time of AZO/SiO<sub>2</sub> transparent heater (~65 s), the response time of a-ZITO thin films is longer. This might be due to slower heat conduction in the amorphous structure [165]. Furthermore, the dependence of the response time to the input voltage in case of AZO/SiO<sub>2</sub> thin films is insignificant, whereas for a-ZITO thin films it is decreases with increasing voltage. This indicates

an increase in thermal conductivity, and can be attributed to increase in the specific heat of the film with increasing input power due to higher voltage inputs [166].

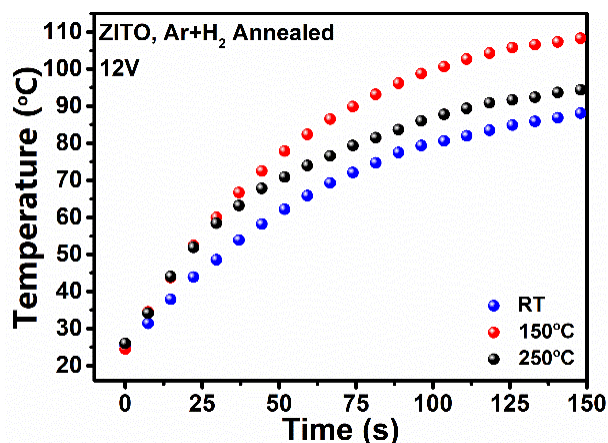


Figure 4.51 Heating behavior of annealed a-ZITO thin films under 12 V

Figure 4.51 is given to compare the heating behavior of annealed a-ZITO thin films, under 12 V supply. As previously stated, the highest saturation temperature achieved with these samples are 94, 112, and 98 °C, in accordance with the increasing substrate temperature. The figure shows that the 150 °C deposited sample not only provides the highest saturation temperature but a higher heating rate than the others. The heating curve of the sample deviates at the 7<sup>th</sup> s from the curve of RT deposited and at the 29<sup>th</sup> s from the curve of 250 °C deposited thin film. Accordingly, the response time were measured to be 124, 102, and 105 s, respectively with the increasing substrate temperature. In other words, the lowest response time was recorded for the sample deposited at 150 °C. These findings once more indicate that the best sample among the produced a-ZITO thin films, in terms of the purposes of this thesis study is the one deposited at a substrate temperature of 150 °C.

Figure 4.52 demonstrates the heating behaviour of this sample in different aspects. The response of the heater to incremental voltage increase is given in Figure 4.52 (a). In this test, an initial voltage of 2 V was applied from both edges (5 cm) of the sample at RT, and the sample kept under this condition for 60 s, and then the voltage



was increased to 4 V. The experiment was continued in this way up to 12 V. Thus, the change in the surface temperature of the sample as a function of voltage increment and time was determined. The obtained curve shows that there is no significant change in sample surface temperature up to 4 V. The heater responded similar to each voltage increase after 4 V and the surface temperature increased almost linearly beginning from 6 V. From the thermal camera images given as insets, one can see that the temperature of the heater increases with increasing input voltage. After waiting for 60 s at 12 V, the test was terminated at a surface temperature of  $\sim 96^\circ\text{C}$ .

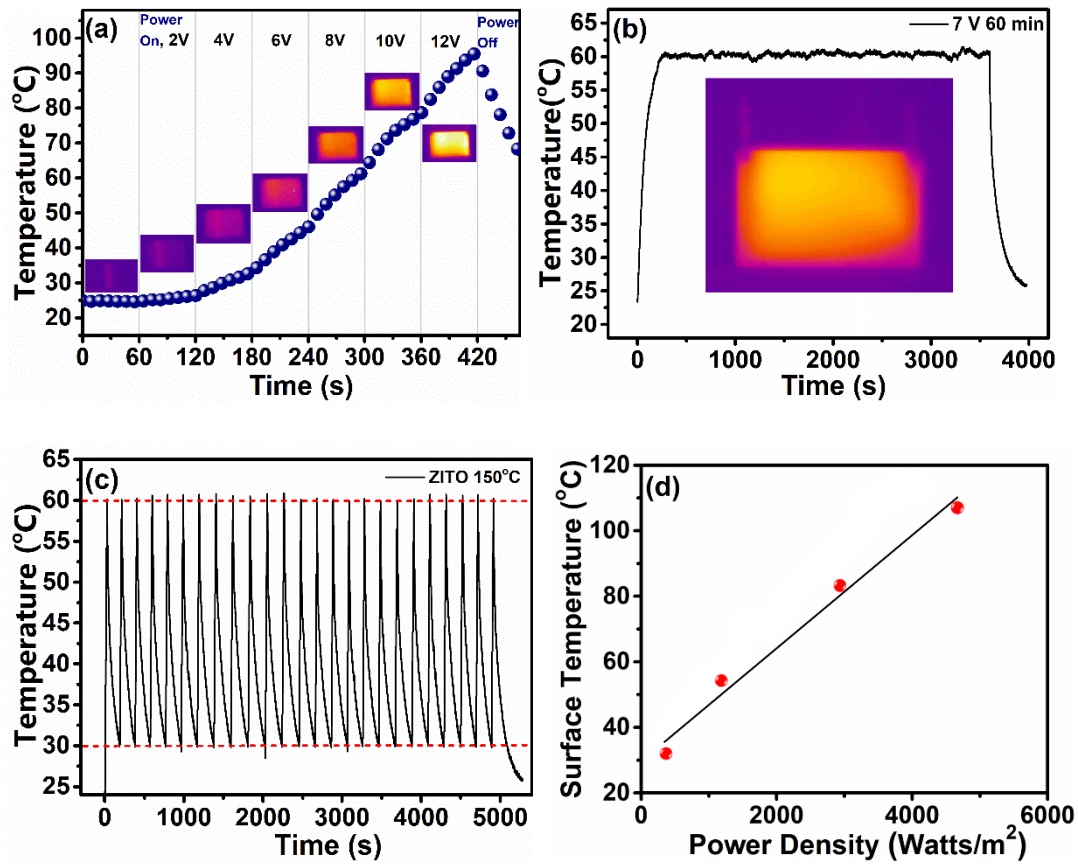


Figure 4.52 Electro-thermal response of 150  $^\circ\text{C}$  deposited a-ZITO transparent heater after annealing under Ar+4%  $\text{H}_2$  for 90 min at 400  $^\circ\text{C}$ ; **a)** thermal response of the heater to incremental input voltage increase, **b)** long-term loading stability, **c)** cyclic loading performance of the heater, **d)** power density vs. surface saturation temperature plot (the insets in (a) and (b) refer to thermal camera images of the sample at the relevant temperature)



In order to evaluate the heating performance of a-ZITO transparent heater in cyclic or long-term loadings, two separate tests were carried out using samples kept at RT. The first of these tests was applied by increasing the sample to a constant temperature of 60 °C by applying a constant voltage such as 7 V, and by monitoring the change in the surface temperature for 3600 s., Figure 4.52 (b). As can be seen, the mean surface temperature of the sample remains almost constant ( $\pm 0.4$  °C) throughout this duration. This result reveals the operational stability of the heater in excess of 3600 s, under atmospheric conditions when kept at 60 °C. The inset image shows the homogeneous temperature distribution of the sample under these test conditions. The surface temperature homogeneity of the heater was determined as 19.66% using this inset and Equation (3.8). This value is better than the temperature uniformity provided by wire-patterned de-icers proposed for automobile windows [154], and Ni-quantum nanoparticle coated FTO transparent heaters [123]. Further, its comparable to temperature uniformity of NiCr/FTO (19.2 %), and bare FTO (19.7 %) heaters, but less than Cr/FTO (14.65 %), AZO/SiO<sub>2</sub> (13.66 %), FTO/AZO (11.42 %), and AZO (17.70 %) thin film transparent heaters [52], [167], [168].

Figure 4.52 (c) represents the result of the cycling loading behavior of the a-ZITO transparent heater. During measurement, first the sample was supplied with 12 V and when the surface temperature reached 60 °C, the input voltage was shifted to 0 V to allow the cooling of the sample to 30 °C. Then the sample loaded again with 12 V up to 60 °C. This successive loadings were repeated for 25 cycles. The thermal cycle limits are shown by the red dashed lines at the top and bottom of the figure. In each cycle, the sample reached the peak temperature in around 25 s and cooled within 1 min. This shows that the heater can provide a heating rate of 1.2 °C/s in the case of 12 V input.

The areal power densities of the transparent heater were calculated for each voltage value and plotted against the corresponding saturation temperatures and presented in Figure 4.52 (d). Then, the thermal resistance of a-ZITO transparent heater was obtained as 181.7 °C.cm<sup>2</sup>/Watt from the slope of  $T$  vs.  $P$ . This value is slightly lower

than the thermal resistance ( $219\text{ }^{\circ}\text{C}\cdot\text{cm}^2/\text{Watt}$ ) determined for the AZO/SiO<sub>2</sub> transparent heater. This is not surprising due to lower thermal conductivity of the sample in related to its amorphous nature.

Using  $P=I^2R$  and  $R=(L/W_e d_k)$  equations, the power consumption of this heater is calculated to be  $3.95\text{ W}$  ( $L=5\text{ cm}$ ,  $W_e = 6.44\text{ cm}$ , and  $d_k = 7.5\times 10^{-5}\text{ cm}$ ). Finally, the power density of the heater under  $12\text{ V}$  supply was calculated to be  $0.4635\text{ Watt}/\text{cm}^2$  which is in the range ( $0.4\text{--}0.77\text{ Watt}/\text{cm}^2$ ) necessary for deicing applications.

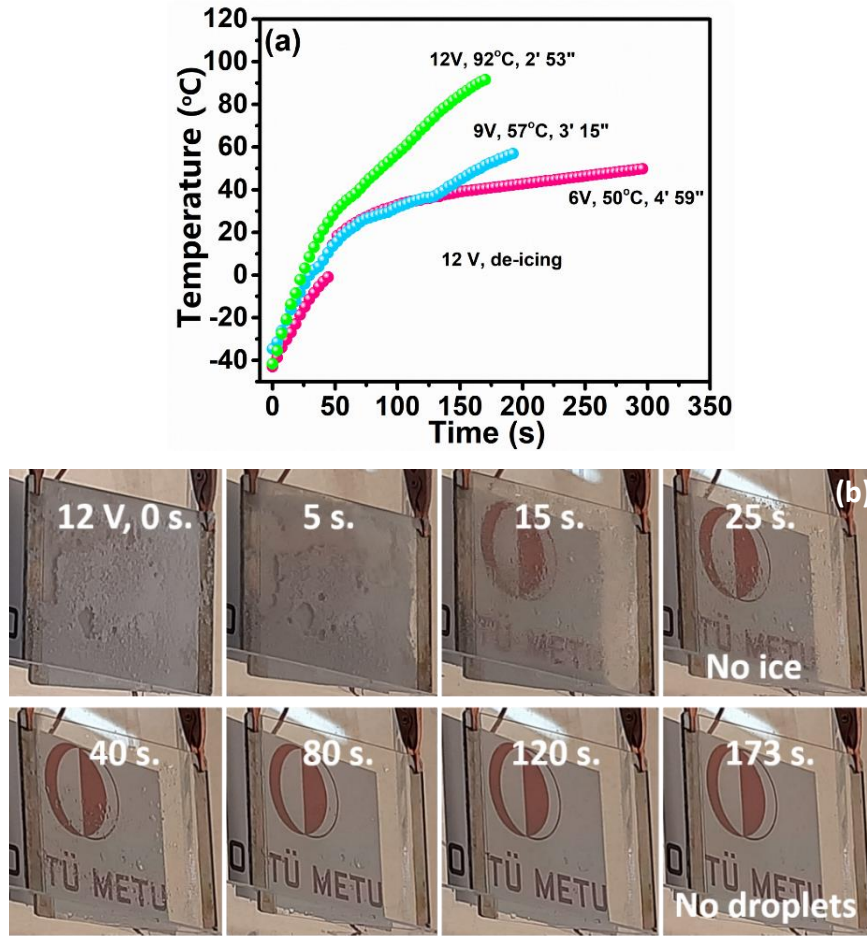


Figure 4.53 **a)** Deicing performance and heating curves of dry-ice cooled a-ZITO transparent heater with various input voltages **b)** digital images showing the course of deicing under  $12\text{ V}$  on  $5.0 \times 7.5\text{ mm}^2$  a-ZITO transparent heater (the insets given in (a) shows the thermal camera images of the sample during deicing at some certain time and temperatures)

The de-icing performance of 150 °C deposited sample was examined by holding the sample in a dry-ice filled box for 1 h, prior to measurements. The tests were conducted by loading certain constant voltages (6, 9, or 12 V) to sample at -40 °C. By doing this, the tunability of its deicing capacity was determined. The de-icing curves under these conditions are presented in Figure 4.53 (a). The inset values given next to each curve refers to elapsed time until the last water droplet was evaporated from the surface and the maximum recorded mean surface temperature at the end of this time.

In case of 6 V, the mean surface temperature of the heater increased 0 °C after 45 s and reached to 20 °C at the 66. s. The overall time for de-icing was recorded as 299 s. At this point the mean surface temperature was measured as 50 °C. For the input voltage of 9 V, 0 °C was achieved at 29<sup>th</sup> s and all ice/water-based residues were removed at 57 °C after 195 s.

Finally, for 12 V the mean surface temperature was reached to 92 °C and de-icing was completed in a shorter time than others, i.e., after 173 s. 0 °C was attained in ~23 s., and a temperature of ~30 °C was recorded after ~50 s. Above this temperature, the slope of the temperature rise was steeper and the linear fit yielded a heating rate of 0.68 °C/s. The inset images given in this figure corresponds to thermal camera images of the sample at the beginning of the test (left), at 50 °C mean surface temperature and at the end of deicing process (right). As it is clear from the left image, at -40 °C the color of the sample is Prussian blue. At about 50 °C, the appearing of the sample is not homogenous, there are some dark spots on the image corresponding to water droplets after melting of the ice. Finally, at the end of the test all water droplets are evaporated, and the image is more homogenous in terms of color distribution.

Real-time images of the sample during deicing are shown in Figure 4.53 (a). In the beginning of the process the sample is covered with ice and there is no visibility. Partial melting is observed at the 15. s, the mean temperature is still below -0 °C and the sample is blurry with low visibility. With increasing temperature all ice melted,

and only scattered water droplets are left on the surface. Finally, all droplets are evaporated, and a clear visibility was obtained.

## CHAPTER 5

### CONCLUSION

In this thesis study, AZO/SiO<sub>2</sub> and a-ZITO coatings were produced on 5.0 x 7.5 cm<sup>2</sup> glass substrates for transparent heater and heat reflection applications. Most of the work is devoted to determining the optimum magnetron sputtering conditions, specific to each type of coating. SiO<sub>2</sub>-capped AZO thin films were achieved via successive sputtering of high purity AZO and SiO<sub>2</sub> targets. On the other hand, the final composition of a-ZITO coating was determined via the combinatorial approach and co-sputtering of In<sub>2</sub>O<sub>3</sub>, ZnO, and SnO<sub>2</sub> targets. Among the produced sample library, the best sample's composition was selected according to electrical and optical properties, and then this composition was transferred to a 3" single target. Final a-ZITO thin films were produced by sputtering of this mixed-oxide target. All samples were subjected to post-deposition annealing under vacuum, Ar or Ar+4% H<sub>2</sub> atmospheres to improve the optoelectronic properties of the samples. Annealing experiments were conducted at 300-400 °C in the sputtering system or using an atmosphere-controlled furnace.

Indium free AZO/SiO<sub>2</sub> coatings were deposited at a thickness of 750 nm. The AZO layer was first achieved at 200 °C substrate temperature, then the SiO<sub>2</sub> layer was formed at RT. AZO coatings were obtained in polycrystalline form with strong preferred orientation along (002). Ar +4% H<sub>2</sub> atmosphere was determined as the optimum annealing condition for these coatings and therefore, the films were annealed at 400 °C for 1 h under flowing forming gas environment. The RMS surface roughness value was measured to be ~6 nm after SiO<sub>2</sub> top layer coating. In the annealed state, the sheet resistance at RT, the average light transmittance in the visible region, and reflectance at 2500 nm wavelength were determined to be 3.53 Ω/□, 96%, and 73%, respectively. Electrothermal property measurements showed

that the mean surface temperature of AZO/SiO<sub>2</sub> transparent heater can reach to 161 °C under 12 V input. Under these conditions, the power density of the heater was calculated to be 0.5981 Watt/cm<sup>2</sup>. Further, the heater provided remarkable deicing performance and removed all ice/water from the surface within 3 min, starting from -40 °C. The heating rate was obtained as 0.82 °C/s.

a-ZITO coatings, with reduced Indium in their composition compared to commercial ITO coatings, were produced from a single target. The target composition was determined as 53.15 wt. % In, 33.71 wt.% Zn, 7.23 wt.% Sn, and 5.9 wt.% O<sub>2</sub> via the combinatorial approach. Thin films were produced at a thickness of 750 nm, on substrates kept at RT, 150 °C, and 250 °C. Their compositions were determined almost similar to the target composition after post-deposition annealing. Therefore, the thin films produced were comprise of ~21% less In in their compositions than that of commercial ITO. Characterizations showed that all samples were obtained in amorphous structure, and this structure was maintained after annealing in Ar +4% H<sub>2</sub> atmosphere at 400 °C for 90 min. Among them, the sample produced at 150 °C exhibit the best properties in terms of sheet resistance (7.49 Ω/□), average visible light transmittance (~86%), and reflectance at 2500 nm (35%). Further, this film provided a very low RMS value of 1.98 nm. In case of 12 V input, the mean surface temperature reached to a maximum of 112 °C and the power density of the heater was calculated as 0.4635 Watt/cm<sup>2</sup>. The deicing performance of the heater was tested under identical conditions with the AZO coatings and revealed a total deicing time of 2 min 53 sec. The heating rate of the heater was obtained as 0.68 °C/s.

Finally, the study has shown that the produced samples provide sufficient power density in the proposed range (0.4-0.77 Watt/cm<sup>2</sup>) for deicing applications. By assuming identical electrical properties for 1 m<sup>2</sup> heater, an areal projection calculation has revealed that AZO/SiO<sub>2</sub> coatings can compete with commercially available transparent heaters under 12 V of input values. Further, very high reflectivity of 73% at 2500 nm makes this functional coating a suitable choice for heat reflecting applications. In case of a-ZITO coatings, the necessary power density range for deicing applications can be satisfied by 13.5 V. If its reflectivity can be

improved, these amorphous thin films can successfully compete with commercial ITO heaters due to its reduced In content.





## **CHAPTER 6**

### **FUTURE STUDY**

In this thesis study, AZO/SiO<sub>2</sub> and a-ZITO coatings were developed using RF magnetron sputtering method, which is a vacuum-based thin film deposition technique. As mentioned in detail in the previous sections, both functional coatings provided sufficient performance as a transparent heater in the laboratory environment. Furthermore, although it is not included in the scope of this study, and despite the fact that the heaters have been proven to be stable under working condition for 1 h or cycling thermal loading, it is suggested that the long-term stability tests can be performed for practical applications. At this point, one of the important points to be considered is the necessity of applying these performance tests in cold ambient condition.



## REFERENCES

- [1] H. McMaster, “Conductive coating for glass and method of application,” 1947.
- [2] A. Piegari and F. Flory, *Optical Thin Films and Coatings From Materials to Applications*, 2nd ed. Sawston, Cambridge: Woodhead Publishing, 2013.
- [3] Joule, “Joules Law This Month Physics History: December 1840: Joule’s abstract on converting mechanical power into heat,” *American Physical Society*, 1840. .
- [4] D. T. Papanastasiou *et al.*, “Transparent Heaters: A Review,” *Adv. Funct. Mater.*, vol. 30, no. 21, pp. 1–33, 2020, doi: 10.1002/adfm.201910225.
- [5] M. Chen, Z. L. Pei, X. Wang, Y. H. Yu, X. H. Liu, and C. Sun, “Intrinsic limit of electrical properties,” *J. Phys. D. Appl. Phys.*, vol. 33, pp. 2538–2548, 2000.
- [6] U. Nations, “Concerning the adoption of uniform technical prescriptions for wheeled vehicles, equipment and parts which can be fitted and/or be used on wheeled vehicles and the conditions for reciprocal recognition of approvals granted on the basis of these prescripti,” 2012.
- [7] D. S. Y. Jayathilake, J. S. Sagu, and K. G. U. Wijayantha, “Transparent heater based on Al,Ga co-doped ZnO thin films,” *Mater. Lett.*, vol. 237, no. November, pp. 249–252, 2019, doi: 10.1016/j.matlet.2018.11.092.
- [8] O. Ergun, S. Coskun, Y. Yusufoglu, and H. E. Unalan, “High-performance, bare silver nanowire network transparent heaters,” *Nanotechnology*, vol. 27, no. 44, pp. 1–9, 2016, doi: 10.1088/0957-4484/27/44/445708.
- [9] R. Gupta, K. D. M. Rao, S. Kiruthika, and G. U. Kulkarni, “Visibly

- Transparent Heaters,” *ACS Appl. Mater. Interfaces*, vol. 8, no. 20, pp. 12559–12575, 2016, doi: 10.1021/acsami.5b11026.
- [10] T. J. Kang, T. Kim, S. M. Seo, Y. J. Park, and Y. H. Kim, “Thickness-dependent thermal resistance of a transparent glass heater with a single-walled carbon nanotube coating,” *Carbon N. Y.*, vol. 49, no. 4, pp. 1087–1093, 2011, doi: 10.1016/j.carbon.2010.11.012.
- [11] K. J. Nasr and B. S. AbdulNour, “Defrosting of automotive windshields: progress and challenges,” *Int. J. Veh. Des.*, vol. 23, no. 3, pp. 360–375, 2000, doi: 10.1504/ijvd.2000.001901.
- [12] W. G. Park, M. S. Park, Y. R. Jung, and K. L. Jang, “Numerical study of defrosting phenomena of automotive windshield glass,” *Numer. Heat Transf. Part A Appl.*, vol. 47, no. 7, pp. 725–739, 2005, doi: 10.1080/10407780590911512.
- [13] “THERMOVIT® Electrically heated glass solutions for marine applications,” 2021. [https://www.vetrotech.com/system/files/2017-10/20170914\\_Thermovit\\_Brochure\\_EN\\_0.pdf](https://www.vetrotech.com/system/files/2017-10/20170914_Thermovit_Brochure_EN_0.pdf) (accessed Jul. 13, 2021).
- [14] R. T. Wipfler and M. Narasimhan, “Patterned Conductive Elements For Resistively Heated Glazing,” *US 2007 / 0197807 A1*, vol. 1, no. 60, pp. 19–21, 2007.
- [15] S. Kiruthika, R. Gupta, and G. U. Kulkarni, “Large area defrosting windows based on electrothermal heating of highly conducting and transmitting Ag wire mesh,” *RSC Adv.*, vol. 4, no. 91, pp. 49745–49751, 2014, doi: 10.1039/c4ra06811d.
- [16] Y. Sun, Y. Yin, B. T. Mayers, T. Herricks, and Y. Xia, “Uniform silver nanowires synthesis by reducing AgNO<sub>3</sub> with ethylene glycol in the presence of seeds and poly(vinyl pyrrolidone),” *Chem. Mater.*, vol. 14, no. 11, pp. 4736–4745, 2002, doi: 10.1021/cm020587b.

- [17] S. De *et al.*, “Silver Nanowire Networks as Flexible ,” vol. 3, no. 7, pp. 1767–1774, 2009.
- [18] L. Hu, H. S. Kim, J. Y. Lee, P. Peumans, and Y. Cui, “Scalable coating and properties of transparent, flexible, silver nanowire electrodes,” *ACS Nano*, vol. 4, no. 5, pp. 2955–2963, 2010, doi: 10.1021/nn1005232.
- [19] J. Y. Lee, S. T. Connor, Y. Cui, and P. Peumans, “Solution-processed metal nanowire mesh transparent electrodes,” *Nano Lett.*, vol. 8, no. 2, pp. 689–692, 2008, doi: 10.1021/nl073296g.
- [20] Y. C. Lu and K. S. Chou, “Tailoring of silver wires and their performance as transparent conductive coatings,” *Nanotechnology*, vol. 21, no. 21, p. 215707, 2010, doi: 10.1088/0957-4484/21/21/215707.
- [21] A. Tao *et al.*, “Langmuir-Blodgett silver nanowire monolayers for molecular sensing using surface-enhanced Raman spectroscopy,” *Nano Lett.*, vol. 3, no. 9, pp. 1229–1233, 2003, doi: 10.1021/nl0344209.
- [22] H. H. Khaligh *et al.*, “The Joule heating problem in silver nanowire transparent electrodes,” *Nanotechnology*, vol. 28, no. 42, p. 425703, Oct. 2017, doi: 10.1088/1361-6528/aa7f34.
- [23] X. Chen *et al.*, “Printable High-Aspect Ratio and High-Resolution Cu Grid Flexible Transparent Conductive Film with Figure of Merit over 80 000,” *Adv. Electron. Mater.*, vol. 5, no. 5, pp. 1–8, 2019, doi: 10.1002/aelm.201800991.
- [24] S. Polat Genlik *et al.*, “All-Solution-Processed, Oxidation-Resistant Copper Nanowire Networks for Optoelectronic Applications with Year-Long Stability,” *Cite This ACS Appl. Mater. Interfaces*, vol. 12, pp. 45136–45144, 2020, doi: 10.1021/acsami.0c11729.
- [25] A. K. Geim and K. S. Novoselov, “The rise of graphene PROGRESS,” *Nat. Mater.*, vol. 6, no. 3, pp. 183–191, 2007.
- [26] X. Li *et al.*, “Transfer of large-area graphene films for high-performance

- transparent conductive electrodes,” *Nano Lett.*, vol. 9, no. 12, pp. 4359–4363, 2009, doi: 10.1021/nl902623y.
- [27] V. C. Tung, M. J. Allen, Y. Yang, and R. B. Kaner, “High-throughput solution processing of large-scale graphene,” *Nat. Nanotechnol.*, vol. 4, no. 1, pp. 25–29, 2009, doi: 10.1038/nnano.2008.329.
- [28] R. R. Nair *et al.*, “Fine structure constant defines visual transparency of graphene,” *Science* (80-. ), vol. 320, no. 5881, p. 1308, 2008, doi: 10.1126/science.1156965.
- [29] S. Bae *et al.*, “Roll-to-roll production of 30-inch graphene films for transparent electrodes,” *Nat. Nanotechnol.*, vol. 5, no. 8, pp. 574–578, 2010, doi: 10.1038/nnano.2010.132.
- [30] G. Kalita, M. Matsushima, H. Uchida, K. Wakita, and M. Umeno, “Graphene constructed carbon thin films as transparent electrodes for solar cell applications,” *J. Mater. Chem.*, vol. 20, no. 43, p. 9713, 2010, doi: 10.1039/c0jm01352h.
- [31] D. Langley, G. Giusti, C. Mayousse, C. Celle, D. Bellet, and J.-P. Simonato, “Flexible transparent conductive materials based on silver nanowire networks: a review,” *Nanotechnology*, vol. 24, no. 45, p. 452001, Nov. 2013, doi: 10.1088/0957-4484/24/45/452001.
- [32] B. S. Shim, J. Zhu, E. Jan, K. Critchley, and N. A. Kotov, “Transparent Conductors from Layer-by-Layer Assembled SWNT Films: Importance of Mechanical Properties and a New Figure of Merit,” *ACS Nano*, vol. 4, no. 7, pp. 3725–3734, 2010, doi: 10.1021/nn100026n.
- [33] Y. H. Yoon *et al.*, “Transparent film heater using single-walled carbon nanotubes,” *Adv. Mater.*, vol. 19, no. 23, pp. 4284–4287, 2007, doi: 10.1002/adma.200701173.
- [34] B. Qing Cao *et al.*, “Highly Bendable, Transparent Thin-Film Transistors That

- Use Carbon-Nanotube-Based Conductors and Semiconductors with Elastomeric Dielectrics\*\*,” *Adv. Mater.*, vol. 18, pp. 304–309, 2006, doi: 10.1002/adma.200501740.
- [35] H. S. Jang, S. K. Jeon, and S. H. Nahm, “The manufacture of a transparent film heater by spinning multi-walled carbon nanotubes,” *Carbon N. Y.*, vol. 49, no. 1, pp. 111–116, Jan. 2011, doi: 10.1016/j.carbon.2010.08.049.
- [36] K. Zhu, H. Wang, F. Xiao, and F. Xu, “Effect of buffer thickness on the properties of Al-doped ZnO thin films prepared by DC magnetron sputtering,” *J. Mater. Sci. Mater. Electron.*, vol. 28, no. 10, pp. 7302–7306, 2017, doi: 10.1007/s10854-017-6415-7.
- [37] A. Facchetti and T. . Marks, *Transparent electronics from synthesis to applications*. Wiley, 2010.
- [38] A. . Freeman, K. R. Poeppelmeier, T. O. Mason, R. P. H. Chang, and T. . Marks, “Chemical and Thin-Film Strategies for New Transparent Conducting Oxides,” *MRS Bull.*, vol. 25, pp. 45–51, 2000, doi: <https://doi.org/10.1557/mrs2000.150>.
- [39] E. Burstein, “Anomalous optical absorption limit in InSb [4],” *Phys. Rev.*, vol. 93, no. 3, pp. 632–633, 1954, doi: 10.1103/PhysRev.93.632.
- [40] T. S. Moss, “The interpretation of the properties of indium antimonide,” *Proc. Phys. Soc. Sect. B*, vol. 67, no. 10, pp. 775–782, 1954, doi: 10.1088/0370-1301/67/10/306.
- [41] VarTech Systems Inc., “COTS Military Grade Ultra Rugged LCDs.” <http://www.xycom.co.kr/pdfs/brochures/xtremeseries.pdf> (accessed Jun. 03, 2021).
- [42] “Indium Tin Oxide,” 2017. [https://www.wikizero.com/en/Indium\\_tin\\_oxide](https://www.wikizero.com/en/Indium_tin_oxide) (accessed Dec. 25, 2017).
- [43] “Aerospace technologies heating systems,” 2021. <http://www.saint-gobain->

sully.com/aerospace\_technologies\_heating\_systems.php (accessed Jun. 03, 2021).

- [44] F. Kurdesau, G. Khripunov, A. F. da Cunha, M. Kaelin, and A. N. Tiwari, “Comparative study of ITO layers deposited by DC and RF magnetron sputtering at room temperature,” *J. Non. Cryst. Solids*, vol. 352, no. 9-20 SPEC.ISS., pp. 1466–1470, Jun. 2006, doi: 10.1016/j.jnoncrysol.2005.11.088.
- [45] T. Maruyama and K. Fukui, “Indium tin oxide thin films prepared by chemical vapour deposition,” *Thin Solid Films*, vol. 203, no. 2, pp. 297–302, Aug. 1991, doi: 10.1016/0040-6090(91)90137-M.
- [46] S. M. Rozati and T. Ganj, “Transparent conductive Sn-doped indium oxide thin films deposited by spray pyrolysis technique,” *Renew. Energy*, vol. 29, no. 10, pp. 1671–1676, Aug. 2004, doi: 10.1016/j.renene.2004.01.008.
- [47] “Transparent Heaters,” 2019. <https://dontech.com/transparent-heaters/> (accessed May 30, 2021).
- [48] D. S. Liu, C. S. Sheu, C. T. Lee, and C. H. Lin, “Thermal stability of indium tin oxide thin films co-sputtered with zinc oxide,” *Thin Solid Films*, vol. 516, no. 10, pp. 3196–3203, Mar. 2007, doi: 10.1016/j.tsf.2007.09.009.
- [49] K. Yang, K. Cho, K. Im, and S. Kim, “Heat generation characteristics of microheaters prepared with ITO nanoparticles and organic additives,” *Mater. Res. Bull.*, vol. 63, pp. 194–198, Mar. 2015, doi: 10.1016/j.materresbull.2014.12.018.
- [50] H. T. Cao *et al.*, “Properties of transparent conducting ZnO : Al oxide thin films and their application for molecular organic light-emitting diodes,” *J. Mater. Sci. Electron.*, vol. 15, no. 3, pp. 169–174, 2004.
- [51] T. Minami, “Substitution of transparent conducting oxide thin films for indium tin oxide transparent electrode applications,” *Thin Solid Films*, vol. 516, no. 7, pp. 1314–1321, 2008, doi: 10.1016/j.tsf.2007.03.082.



- [52] B. Tönbul, H. A. Can, T. Öztürk, and H. Akyıldız, “Solution processed aluminum-doped ZnO thin films for transparent heater applications,” *Mater. Sci. Semicond. Process.*, vol. 127, p. 105735, Jun. 2021, doi: 10.1016/j.mssp.2021.105735.
- [53] J. G. Lu *et al.*, “Structural, optical, and electrical properties of (Zn,Al)O films over a wide range of compositions,” *J. Appl. Phys.*, vol. 100, no. 7, p. 073714, 2006, doi: 10.1063/1.2357638.
- [54] S. Mridha and D. Basak, “Aluminium doped ZnO films,” 2007, doi: 10.1088/0022-3727/40/22/008.
- [55] M. Olvera, H. Gómez, and A. Maldonado, “Doping, vacuum annealing, and thickness effect on the physical properties of zinc oxide films deposited by spray pyrolysis,” *Sol. Energy Mater. Sol. Cells*, vol. 91, no. 15–16, pp. 1449–1453, Sep. 2007, doi: 10.1016/j.solmat.2007.05.007.
- [56] T. Minami, “Transparent conducting oxide semiconductors for transparent electrodes,” *Semicond. Sci. Technol.*, vol. 20, no. 4, pp. 35–44, 2005, doi: 10.1088/0268-1242/20/4/004.
- [57] M. Burriel, J. Santiso, M. D. Rossell, G. Van Tendeloo, A. Figueras, and G. Garcia, “Enhancing Total Conductivity of  $\text{La}_{2}\text{NiO}_{4+\delta}$  Epitaxial Thin Films by Reducing Thickness,” doi: 10.1021/jp7101622.
- [58] Y. S. Liu *et al.*, “Mechanism of conductivity degradation of AZO thin film in high humidity ambient,” *Appl. Surf. Sci.*, vol. 282, pp. 32–37, 2013, doi: 10.1016/j.apsusc.2013.04.167.
- [59] V. Huong Nguyen, D. Bellet, B. Masenelli, D. Mun, U. Grenoble Alpes, and L. Bourget-du-Lac, “Increasing the Electron Mobility of ZnO-Based Transparent Conductive Films Deposited by Open-Air Methods for Enhanced Sensing Performance,” *ACS Appl. Nano Mater.*, vol. 1, no. 12, pp. 6922–6931, 2018, doi: 10.1021/acsanm.8b01745.

- [60] V. Huong Nguyen, ab Ulrich Gottlieb, A. Valla, D. Muñoz, D. Bellet, and D. Muñoz-Rojas, “Electron tunneling through grain boundaries in transparent conductive oxides and implications for electrical conductivity: the case of ZnO:Al thin films †,” vol. 5, p. 715, 2018, doi: 10.1039/c8mh00402a.
- [61] Y. C. Lin, J. H. Jiang, and W. T. Yen, “Effect of Cr and V dopants on the chemical stability of AZO thin film,” *Appl. Surf. Sci.*, vol. 255, no. 6, pp. 3629–3634, 2009, doi: 10.1016/j.apsusc.2008.10.019.
- [62] K. Tominaga, T. Takao, A. Fukushima, T. Moriga, and I. Nakabayashi, “Film properties of ZnO:Al films deposited by co-sputtering of ZnO:Al and contaminated Zn targets with Co, Mn and Cr,” *Vacuum*, vol. 66, no. 3–4, pp. 511–515, Aug. 2002, doi: 10.1016/S0042-207X(02)00124-0.
- [63] W. Chen *et al.*, “ITO@SiO<sub>2</sub> and ITO@{M 6 Br 12 }@SiO<sub>2</sub> (M ¼ Nb, Ta) nanocomposite films for ultraviolet-near infrared shielding †,” 2019, doi: 10.1039/c9na00400a.
- [64] X. Li, W. Tang, C. Chen, C. Lin, and C. Xu, “Effect of annealing treatment on the structure and performance of transparent conductive AZO/Al<sub>2</sub>O<sub>3</sub> bi-layer films,” *Mater. Res. Express*, vol. 6, no. 9, p. 096414, 2019, doi: 10.1088/2053-1591/ab2e58.
- [65] H. Chen, Y.-H. Jeong, and C.-B. Park, “Enhancement of Electrical Properties on ZnO: Al Thin Film due to Hydrogen Annealing and SiO<sub>2</sub> Coating in Damp-heat Environment,” *Trans. Electr. Electron. Mater.*, vol. 10, no. 2, pp. 58–61, 2009, doi: 10.4313/teem.2009.10.2.058.
- [66] T. Guo, L. Zheng, J. P. Nshimiyimana, X. Diao, and Q. Chen, “Design of antireflective coatings for AZO low infrared emissivity layer,” *Chinese Opt. Lett.*, no. 13, pp. 9–11, 2013, doi: 10.3788/COL201311.S10103.
- [67] D. Miao, S. Jiang, S. Shang, and Z. Chen, “Effect of heat treatment on infrared reflection property of Al-doped ZnO films,” *Sol. Energy Mater. Sol. Cells*, vol. 127, pp. 163–168, doi: 10.1016/j.solmat.2014.04.030.

- [68] L. Gong *et al.*, “Highly transparent conductive and near-infrared reflective ZnO:Al thin films,” *Vacuum*, vol. 84, no. 7, pp. 947–952, 2010, doi: 10.1016/j.vacuum.2010.01.010.
- [69] R. Das and S. Ray, “Zinc oxide - A transparent, conducting IR-reflector prepared by rf-magnetron sputtering,” *J. Phys. D. Appl. Phys.*, vol. 36, no. 2, pp. 152–155, 2003, doi: 10.1088/0022-3727/36/2/312.
- [70] D. Miao, S. Jiang, S. Shang, and Z. Chen, “Infrared reflective properties of AZO/Ag/AZO trilayers prepared by RF magnetron sputtering,” *Ceram. Int.*, vol. 40, no. 8, pp. 12847–12853, Sep. 2014, doi: 10.1016/J.CERAMINT.2014.04.139.
- [71] U. Gangopadhyay, K. Kim, D. Mangalaraj, and J. Yi, “Low cost CBD ZnS antireflection coating on large area commercial mono-crystalline silicon solar cells,” *Appl. Surf. Sci.*, vol. 230, no. 1–4, pp. 364–370, May 2004, doi: 10.1016/j.apsusc.2004.02.059.
- [72] T. Wiktorczyk and M. Oleś, “Design, fabrication and optical characterization of cerium oxide-magnesium fluoride double layer antireflection coatings on monocrystalline silicon substrates,” *Opt. Mater. (Amst.)*, vol. 29, no. 12, pp. 1768–1773, Aug. 2007, doi: 10.1016/j.optmat.2006.09.018.
- [73] J. Ni, Q. Zhao, and X. Zhao, “Transparent and high infrared reflection film having sandwich structure of SiO<sub>2</sub>/Al:ZnO/SiO<sub>2</sub>,” *Prog. Org. Coatings*, vol. 64, no. 2–3, pp. 317–321, 2009, doi: 10.1016/j.porgcoat.2008.08.030.
- [74] D. Zhu, K. Li, F. Luo, and W. Zhou, “Preparation and infrared emissivity of ZnO: Al (AZO) thin films,” *Appl. Surf. Sci.*, vol. 255, no. 12, pp. 6145–6148, Apr. 2009, doi: 10.1016/j.apsusc.2009.01.068.
- [75] W. G. J. H. . Van sark, F. Roca, and L. Korte, *Physics and technology of amorphous-crystalline heteronstructures sillicon solar cells*. 2011.
- [76] B. P. Shantheyanda, V. O. Todi, K. B. Sundaram, A. Vijayakumar, and I.

- Oladeji, “Compositional study of vacuum annealed Al doped ZnO thin films obtained by RF magnetron sputtering,” *J. Vac. Sci. Technol. A Vacuum, Surfaces, Film.*, vol. 29, no. 5, p. 051514, 2011, doi: 10.1116/1.3624787.
- [77] L. Gong *et al.*, “Highly transparent conductive and near-infrared reflective ZnO:Al thin films,” *Vacuum*, vol. 84, no. 7, pp. 947–952, Mar. 2010, doi: 10.1016/j.vacuum.2010.01.010.
- [78] T. Ivanova, A. Harizanova, T. Koutzarova, and B. Vertruyen, “Optical characterization of sol-gel ZnO:Al thin films,” *Superlattices Microstruct.*, vol. 85, pp. 101–111, Jun. 2015, doi: 10.1016/j.spmi.2015.05.013.
- [79] D. K. Kim and H. B. Kim, “Room temperature deposition of Al-doped ZnO thin films on glass by RF magnetron sputtering under different Ar gas pressure,” *J. Alloys Compd.*, vol. 509, no. 2, pp. 421–425, 2011, doi: 10.1016/j.jallcom.2010.09.047.
- [80] Y. Q. Li, Y. Z. Shen, and F. L. Du, “Infrared emissivity properties of Sn doped ZnO films deposited by sol-gel method,” *Mater. Res. Innov.*, vol. 18, no. 1, pp. 57–62, 2014, doi: 10.1179/1433075X13Y.0000000113.
- [81] M. Saad and A. Kassis, “Effect of rf power on the properties of rf magnetron sputtered ZnO:Al thin films,” *Mater. Chem. Phys.*, vol. 136, no. 1, pp. 205–209, Sep. 2012, doi: 10.1016/j.matchemphys.2012.06.053.
- [82] Z. Zhang, C. Bao, W. Yao, S. Ma, L. Zhang, and S. Hou, “Influence of deposition temperature on the crystallinity of Al-doped ZnO thin films at glass substrates prepared by RF magnetron sputtering method,” *Superlattices Microstruct.*, vol. 49, no. 6, pp. 644–653, Jun. 2011, doi: 10.1016/j.spmi.2011.04.002.
- [83] D. S. Kim *et al.*, “Effect of deposition temperature on the properties of Al-doped ZnO films prepared by pulsed DC magnetron sputtering for transparent electrodes in thin-film solar cells,” *Appl. Surf. Sci.*, vol. 259, pp. 596–599, 2012, doi: 10.1016/j.apsusc.2012.07.082.

- [84] B. L. Zhu *et al.*, “Influence of hydrogen introduction on structure and properties of ZnO thin films during sputtering and post-annealing,” *Thin Solid Films*, vol. 519, no. 11, pp. 3809–3815, Mar. 2011, doi: 10.1016/j.tsf.2011.01.187.
- [85] M. Chaves *et al.*, “Al-doping and properties of AZO thin films grown at room temperature: Sputtering pressure effect,” *Mater. Res.*, vol. 22, no. 2, 2019, doi: 10.1590/1980-5373-MR-2018-0665.
- [86] Y. Igasaki and H. Kanma, “Argon gas pressure dependence of the properties of transparent conducting ZnO:Al films deposited on glass substrates,” *Appl. Surf. Sci.*, vol. 169–170, pp. 508–511, Jan. 2001, doi: 10.1016/S0169-4332(00)00748-0.
- [87] M. Saad and A. Kassis, “Effect of rf power on the properties of rf magnetron sputtered ZnO:Al thin films,” *Mater. Chem. Phys.*, vol. 136, no. 1, pp. 205–209, 2012, doi: 10.1016/j.matchemphys.2012.06.053.
- [88] C. Lennon, R. B. Tapia, R. Kodama, Y. Chang, S. Sivananthan, and M. Deshpande, “Effects of annealing in a partially reducing atmosphere on sputtered Al-Doped ZnO thin films,” *J. Electron. Mater.*, vol. 38, no. 8, pp. 1568–1573, 2009, doi: 10.1007/s11664-009-0747-x.
- [89] P. Nunes, E. Fortunato, and R. Martins, “Influence of the post-treatment on the properties of ZnO thin films,” *Thin Solid Films*, vol. 383, no. 1–2, pp. 277–280, Feb. 2001, doi: 10.1016/S0040-6090(00)01577-7.
- [90] P. Nunes, A. Malik, B. Fernandes, E. Fortunato, P. Vilarinho, and R. Martins, “Influence of the doping and annealing atmosphere on zinc oxide thin films deposited by spray pyrolysis,” *Vacuum*, vol. 52, no. 1–2, pp. 45–49, 1999, doi: 10.1016/s0042-207x(98)00321-2.
- [91] A. Rose and G. J. Exarhos, “Ellipsometric studies of thermally induced transformation phenomena in oxide films,” *Thin Solid Films*, vol. 308–309, no. 1–4, pp. 42–49, 1997, doi: 10.1016/S0040-6090(97)00534-8.

- [92] W. Tang and D. C. Cameron, "Aluminum-doped zinc oxide transparent conductors deposited by the sol-gel process," *Thin Solid Films*, vol. 238, no. 1, pp. 83–87, 1994, doi: 10.1016/0040-6090(94)90653-X.
- [93] K. Tominaga, M. Kataoka, H. Manabe, T. Ueda, and I. Mori, "Transparent ZnO:Al films prepared by co-sputtering of ZnO:Al with either a Zn or an Al target," *Thin Solid Films*, vol. 290–291, pp. 84–87, Dec. 1996, doi: 10.1016/S0040-6090(96)09127-4.
- [94] S. Yanfeng, W. Liu, H. Zhidan, L. Shaolin, Z. Zhao Yi, and G. Du, "Novel properties of AZO film sputtered in Ar+H<sub>2</sub> ambient at high temperature," *Vacuum*, vol. 80, no. 9, pp. 981–985, Jun. 2006, doi: 10.1016/j.vacuum.2005.12.011.
- [95] M. K. Roul, B. Obasogie, G. Kogo, J. R. Skuza, R. M. Mundle, and A. K. Pradhan, "Transparent and flexible heaters based on Al:ZnO degenerate semiconductor," *J. Appl. Phys.*, vol. 122, no. 13, p. 135110, 2017, doi: 10.1063/1.4992007.
- [96] S. Ke *et al.*, "Van der Waals epitaxy of Al-doped ZnO film on mica as a flexible transparent heater with ultrafast thermal response," *Appl. Phys. Lett.*, vol. 112, no. 3, p. 031905, 2018, doi: 10.1063/1.5010358.
- [97] J. M. Phillips *et al.*, "Zinc-indium-oxide: A high conductivity transparent conducting oxide," *Appl. Phys. Lett.*, vol. 67, no. 1995, p. 2246, 1995, doi: 10.1063/1.115118.
- [98] T. Kamiya, K. Nomura, and H. Hosono, "Origins of High Mobility and Low Operation Voltage of Amorphous Oxide TFTs: Electronic Structure, Electron Transport, Defects and Doping\*," *J. Disp. Technol.*, vol. 5, no. 12, pp. 468–483, 2009, doi: 10.1109/jdt.2009.2034559.
- [99] D. S. Kim *et al.*, "Effect of deposition temperature on the properties of Al-doped ZnO films prepared by pulsed DC magnetron sputtering for transparent electrodes in thin-film solar cells," *Appl. Surf. Sci.*, vol. 259, pp. 596–599,

Oct. 2012, doi: 10.1016/j.apsusc.2012.07.082.

- [100] P. F. Ndione *et al.*, “Tuning the physical properties of amorphous In-Zn-Sn-O thin films using combinatorial sputtering,” *Mrs Commun.*, vol. 6, no. 4, pp. 360–366, 2016, doi: 10.1557/mrc.2016.57.
- [101] D. E. Proffit *et al.*, “Thermal stability of amorphous Zn-In-Sn-O films,” *J. Electroceramics*, vol. 34, no. 2–3, pp. 167–174, 2015, doi: 10.1007/s10832-014-9967-4.
- [102] P. Carreras, A. Antony, F. Rojas, and J. Bertomeu, “Electrical and optical properties of Zn-In-Sn-O transparent conducting thin films,” *Thin Solid Films*, vol. 520, no. 4, pp. 1223–1227, Dec. 2011, doi: 10.1016/j.tsf.2011.06.078.
- [103] D. S. Yang *et al.*, “Local structure and local conduction paths in amorphous (In,Ga,Hf)-ZnO semiconductor thin films,” *Solid State Commun.*, vol. 152, no. 20, pp. 1867–1869, Oct. 2012, doi: 10.1016/j.ssc.2012.07.021.
- [104] S. Calnan and A. N. Tiwari, “High mobility transparent conducting oxides for thin film solar cells,” *Thin Solid Films*, vol. 518, no. 7, pp. 1839–1849, Jan. 2010, doi: 10.1016/j.tsf.2009.09.044.
- [105] D. Bruce Buchholz *et al.*, “The Structure and Properties of Amorphous Indium Oxide,” *Chem. Mater*, vol. 26, p. 26, 2014, doi: 10.1021/cm502689x.
- [106] H. Chou, “Extended wide band gap amorphous aluminium-doped zinc oxide thin films grown at liquid nitrogen temperature,” *J. Phys. D. Appl. Phys.*, vol. 44, p. 205404, 2011, doi: 10.1088/0022-3727/44/20/205404.
- [107] J. D. Perkins *et al.*, “Combinatorial optimization of Transparent conducting oxides (TCOS) for PV,” *Conf. Rec. IEEE Photovolt. Spec. Conf.*, pp. 145–147, 2005, doi: 10.1109/PVSC.2005.1488090.
- [108] D. S. Ginley *et al.*, “Combinatorial exploration of novel transparent conducting oxide materials,” 2005.

- [109] M. Putri, C. Y. Koo, J. A. Lee, J. J. Kim, and H. Y. Lee, “Transparent conducting indium zinc tin oxide thin films with low indium content deposited by radio frequency magnetron sputtering,” in *Thin Solid Films*, May 2014, vol. 559, pp. 44–48, doi: 10.1016/j.tsf.2014.02.016.
- [110] D. B. Buchholz, D. E. Proffit, M. D. Wisser, T. O. Mason, and R. P. H. Chang, “Electrical and band-gap properties of amorphous zinc–indium–tin oxide thin films,” *Prog. Nat. Sci. Mater. Int.*, vol. 22, no. 1, pp. 1–6, Feb. 2012, doi: 10.1016/J.PNSC.2011.12.001.
- [111] K. J. Chen, F. Y. Hung, T. S. Lui, S. J. Chang, and T. Y. Liao, “Characteristics of thin-film-transistors based on Zn-In-Sn-O thin films prepared by co-sputtering system,” *Mater. Trans.*, vol. 53, no. 3, pp. 571–574, 2012, doi: 10.2320/matertrans.M2011347.
- [112] Y. R. Denny *et al.*, “Electrical, electronic and optical properties of amorphous indium zinc tin oxide thin films,” *Appl. Surf. Sci.*, vol. 315, no. 1, pp. 454–458, Oct. 2014, doi: 10.1016/j.apsusc.2014.03.047.
- [113] C. A. Hoel, D. B. Buchholz, R. P. H. Chang, and K. R. Poeppelmeier, “Pulsed-laser deposition of heteroepitaxial corundum-type ZITO: Cor-In<sub>2</sub>-2xZn xSn xO<sub>3</sub>,” *Thin Solid Films*, vol. 520, no. 7, pp. 2938–2942, Jan. 2012, doi: 10.1016/j.tsf.2011.10.012.
- [114] M. H. Kim and H. S. Lee, “Effect of in addition and annealing temperature on the device performance of solution-processed In-Zn-Sn-O thin film transistors,” *Solid. State. Electron.*, vol. 96, pp. 14–18, 2014, doi: 10.1016/j.sse.2014.04.021.
- [115] Y.-B. Lu *et al.*, “How does the multiple constituent affect the carrier generation and charge transport in multicomponent TCOs of In-Zn-Sn oxide †,” *J. Mater. Chem. C*, vol. 3, p. 7727, 2015, doi: 10.1039/c5tc01256b.
- [116] J. E. Medvedeva, D. Bruce Buchholz, R. P. H. Chang, E. Medvedeva, D. B. Buchholz, and R. P. H. Chang, “Review [www.advelectronicmat.de](http://www.advelectronicmat.de) Recent



- Advances in Understanding the Structure and Properties of Amorphous Oxide Semiconductors,” *Adv. Electron. Mater.*, vol. 3, no. 9, p. 1700082, 2017, doi: 10.1002/aelm.201700082.
- [117] T.-W. Kim, G.-S. Heo, H.-S. Kim, and J.-H. Lee, “Combinatorial exploration of new transparent conducting oxide films by using radio frequency sputtering and their application in optoelectronic devices,” *Mater. Res. Soc. Symp. Proc.*, p. 1425, 2012, doi: 10.1557/opl.2012.
- [118] J. H. Ko *et al.*, “Transparent and conducting Zn-Sn-O thin films prepared by combinatorial approach,” *Appl. Surf. Sci.*, vol. 253, no. 18, pp. 7398–7403, Jul. 2007, doi: 10.1016/j.apsusc.2007.03.036.
- [119] M. P. Taylor *et al.*, “Combinatorial Growth and Analysis of the Transparent Conducting Oxide ZnO/In (IZO),” *Macromol. Rapid Commun.*, vol. 25, no. 1, pp. 344–347, 2004, doi: 10.1002/marc.200300231.
- [120] F. Otieno *et al.*, “Role of oxygen concentrations on structural and optical properties of RF magnetron sputtered ZnO thin films,” *Opt. Quantum Electron.*, vol. 51, no. 11, pp. 1–13, 2019, doi: 10.1007/s11082-019-2076-5.
- [121] R. Cebulla, R. Wendt, and K. Ellmer, “Al-doped zinc oxide films deposited by simultaneous rf and dc excitation of a magnetron plasma: Relationships between plasma parameters and structural and electrical film properties,” *J. Appl. Phys.*, vol. 83, no. 2, pp. 1087–1095, 1998, doi: 10.1063/1.366798.
- [122] O. Stenzel, *The Physics of Thin Film Optical Spectra*. Springer, Cham, 2005.
- [123] C. Hudaya, B. J. Jeon, and J. K. Lee, “High Thermal Performance of SnO<sub>2</sub>:F Thin Transparent Heaters with Scattered Metal Nanodots,” *ACS Appl. Mater. Interfaces*, vol. 7, pp. 57–61, 2015, doi: 10.1021/am507497u.
- [124] S. Hayamizu, H. Tabata, H. Tanaka, and T. Kawai, “Preparation of crystallized zinc oxide films on amorphous glass substrates by pulsed laser deposition,” *J. Appl. Phys.*, vol. 80, no. 2, pp. 787–791, 1996, doi:

10.1063/1.362887.

- [125] W. J. Jeong and G. C. Park, “Electrical and optical properties of ZnO thin film as a function of deposition parameters,” *Sol. Energy Mater. Sol. Cells*, vol. 65, no. 1, pp. 37–45, 2001, doi: 10.1016/S0927-0248(00)00075-1.
- [126] V. Şenay, “Some physical properties of nanostructured Al doped ZnO thin films synthesized by RF magnetron sputtering at room temperature,” *J. Mater. Sci. Mater. Electron.*, vol. 30, no. 10, pp. 9910–9915, 2019, doi: 10.1007/s10854-019-01329-6.
- [127] T. Gungor, E. Gungor, and B. Saka, “Fast and interference fringe independent optical characterization of zinc oxide nano thin films using model-based genetic algorithm for optoelectronic applications,” *Nanomater. Nanotechnol.*, vol. 6, pp. 1–7, 2016, doi: 10.1177/1847980416673785.
- [128] A. Monemdjou, F. E. Ghodsi, and J. Mazloom, “The effects of surface morphology on optical and electrical properties of nanostructured AZO thin films: Fractal and phase imaging analysis,” *Superlattices Microstruct.*, vol. 74, pp. 19–33, 2014, doi: 10.1016/j.spmi.2014.06.002.
- [129] Q. You *et al.*, “Highly transparent and conductive Al-doped ZnO films synthesized by pulsed laser co-ablation of Zn and Al targets assisted by oxygen plasma,” *J. Alloys Compd.*, vol. 626, pp. 415–420, 2015, doi: 10.1016/j.jallcom.2014.11.153.
- [130] Y. Kim *et al.*, “Optical and electronic properties of post-annealed ZnO:Al thin films,” *Appl. Phys. Lett.*, vol. 96, no. 17, pp. 1–4, 2010, doi: 10.1063/1.3419859.
- [131] W. Tang and D. C. Cameron, “Aluminum-doped zinc oxide transparent conductors deposited by the sol-gel process,” *Thin Solid Films*, vol. 238, no. 1, pp. 83–87, Jan. 1994, doi: 10.1016/0040-6090(94)90653-X.
- [132] C. Guillén and J. Herrero, “Structure, optical, and electrical properties of

- indium tin oxide thin films prepared by sputtering at room temperature and annealed in air or nitrogen,” *J. Appl. Phys.*, vol. 101, no. 7, 2007, doi: 10.1063/1.2715539.
- [133] B. L. Zhu, S. J. Zhu, J. Wang, J. Wu, D. W. Zeng, and C. S. Xie, “Thickness effect on structure and properties of ZAO thin films by RF magnetron sputtering at different substrate temperatures,” *Phys. E Low-Dimensional Syst. Nanostructures*, vol. 43, no. 9, pp. 1738–1745, 2011, doi: 10.1016/j.physe.2011.05.033.
- [134] J. H. Park *et al.*, “Deposition-temperature effects on AZO thin films prepared by RF magnetron sputtering and their physical properties,” *J. Korean Phys. Soc.*, vol. 49, no. SUPPL. 2, pp. 584–588, 2006.
- [135] L. Dejam, S. Mohammad Elahi, H. H. Nazari, H. Elahi, S. Solaymani, and A. Ghaderi, “Structural and optical characterization of ZnO and AZO thin films: the influence of post-annealing,” *J. Mater. Sci. Mater. Electron.*, vol. 27, no. 1, pp. 685–696, 2016, doi: 10.1007/s10854-015-3804-7.
- [136] U. N. Roy *et al.*, “Al-doped ZnO contact to CdZnTe for x- and gamma-ray detector applications,” *Appl. Phys. Lett.*, vol. 108, no. 24, pp. 1–5, 2016, doi: 10.1063/1.4953883.
- [137] R. Tuyaerts, J. P. Raskin, and J. Proost, “Opto-electrical properties and internal stress in Al:ZnO thin films deposited by direct current reactive sputtering,” *Thin Solid Films*, vol. 695, no. December 2019, p. 137760, 2020, doi: 10.1016/j.tsf.2019.137760.
- [138] K. Tang, S. Gu, J. Liu, J. Ye, S. Zhu, and Y. Zheng, “Effects of indium doping on the crystallographic, morphological, electrical, and optical properties of highly crystalline ZnO films,” *J. Alloys Compd.*, vol. 653, pp. 643–648, Dec. 2015, doi: 10.1016/j.jallcom.2015.09.051.
- [139] D. B. Potter, I. P. Parkin, and C. J. Carmalt, “The effect of solvent on Al-doped ZnO thin films deposited via aerosol assisted CVD,” *RSC Adv.*, vol. 8,

no. 58, pp. 33164–33173, 2018, doi: 10.1039/C8RA06417B.

- [140] N. P. Poddar and S. K. Mukherjee, “Effect of substrates and post-deposition annealing on rf-sputtered Al-doped ZnO (AZO) thin films,” *J. Mater. Sci. Mater. Electron.*, vol. 30, no. 15, pp. 14269–14280, 2019, doi: 10.1007/s10854-019-01796-x.
- [141] G. Fang, D. Li, and B. L. Yao, “Fabrication and vacuum annealing of transparent conductive AZO thin films prepared by DC magnetron sputtering,” *Vacuum*, vol. 68, no. 4, pp. 363–372, Dec. 2002, doi: 10.1016/S0042-207X(02)00544-4.
- [142] W. Zhang, J. Xiong, L. Liu, X. Zhang, and H. Gu, “Influence of annealing temperature on structural, optical and electrical properties of AZO/Pd/AZO films,” *Sol. Energy Mater. Sol. Cells*, vol. 153, pp. 52–60, Aug. 2016, doi: 10.1016/j.solmat.2016.04.015.
- [143] X. C. Ma *et al.*, “Influence of hydrogen annealing on structure and optoelectronic properties in Al doped ZnO thin films,” *Mater. Technol.*, vol. 29, no. 2, pp. 101–104, 2014, doi: 10.1179/1753555713Y.00000000097.
- [144] X. Chen, W. Guan, G. Fang, and X. Z. Zhao, “Influence of substrate temperature and post-treatment on the properties of ZnO:Al thin films prepared by pulsed laser deposition,” *Appl. Surf. Sci.*, vol. 252, no. 5, pp. 1561–1567, Dec. 2005, doi: 10.1016/j.apsusc.2005.02.137.
- [145] S. Singh and S. H. Park, “Effect of post deposition annealing treatments on properties of AZO thin films for schottky diode applications,” *J. Nanosci. Nanotechnol.*, vol. 16, no. 1, pp. 861–866, 2016, doi: 10.1166/jnn.2016.12097.
- [146] Z. Liu, J. Ji, J. Jiang, and J. Wang, “Experimental analysis for electromagnetic scattering characteristics of aluminum-doped zinc oxide (AZO) coated glass,” *Optik (Stuttg.)*, vol. 155, pp. 133–138, Feb. 2018, doi: 10.1016/J.IJLEO.2017.10.122.

- [147] S. Ghosh, A. Mallick, B. Dou, M. F. A. M. van Hest, S. M. Garner, and D. Basak, “A novel blanket annealing process to achieve highly transparent and conducting Al doped ZnO thin films: Its mechanism and application in perovskite solar cells,” *Sol. Energy*, vol. 174, pp. 815–825, Nov. 2018, doi: 10.1016/j.solener.2018.09.017.
- [148] L. Sun, J. T. Grant, J. G. Jones, and N. R. Murphy, “Tailoring electrical and optical properties of Al-doped ZnO thin films grown at room temperature by reactive magnetron co-sputtering: From band gap to near infrared,” *Opt. Mater. (Amst.)*, vol. 84, no. April, pp. 146–157, 2018, doi: 10.1016/j.optmat.2018.06.024.
- [149] D. Miao, H. Zhao, Q. Peng, S. Shang, and S. Jiang, “Fabrication of high infrared reflective ceramic films on polyester fabrics by RF magnetron sputtering,” *Ceram. Int.*, vol. 41, no. 1, pp. 1595–1601, Jan. 2015, doi: 10.1016/J.CERAMINT.2014.09.096.
- [150] D. Miao, S. Jiang, S. Shang, and Z. Chen, “Highly transparent and infrared reflective AZO/Ag/AZO multilayer film prepared on PET substrate by RF magnetron sputtering,” *Vacuum*, vol. 106, pp. 1–4, 2014, doi: 10.1016/j.vacuum.2014.02.021.
- [151] D. Lordan *et al.*, “Asymmetric Pentagonal Metal Meshes for Flexible Transparent Electrodes and Heaters,” *ACS Appl. Mater. Interfaces*, vol. 9, no. 5, pp. 4932–4940, 2017, doi: 10.1021/acsami.6b12995.
- [152] S. Xie, T. Li, Z. Xu, Y. Wang, X. Liu, and W. Guo, “A high-response transparent heater based on a CuS nanosheet film with superior mechanical flexibility and chemical stability,” *Nanoscale*, vol. 10, no. 14, pp. 6531–6538, 2018, doi: 10.1039/c7nr09667d.
- [153] D. Sui, Y. Huang, L. Huang, J. Liang, Y. Ma, and Y. Chen, “Flexible and transparent electrothermal film heaters based on graphene materials,” *Small*, vol. 7, no. 22, pp. 3186–3192, 2011, doi: 10.1002/sml.201101305.

- [154] C. Baldasseroni, D. R. Queen, D. W. Cooke, K. Maize, A. Shakouri, and F. Hellman, "Heat transfer simulation and thermal measurements of microfabricated x-ray transparent heater stages," *Rev. Sci. Instrum.*, vol. 82, no. 9, 2011, doi: 10.1063/1.3640407.
- [155] B. Singh and S. Ghosh, "Highly Conducting Transparent Indium-Doped Zinc Oxide Thin Films," *J. Electron. Mater.*, vol. 43, no. 9, pp. 3217–3221, 2014, doi: 10.1007/s11664-014-3256-5.
- [156] F. Z. Bedia, A. Bedia, M. Aillerie, N. Maloufi, and B. Benyoucef, "Structural, Optical and Electrical Properties of Sn-doped Zinc Oxide Transparent Films Interesting for Organic Solar Cells (OSCs)," *Energy Procedia*, vol. 74, pp. 539–546, Aug. 2015, doi: 10.1016/J.EGYPRO.2015.07.745.
- [157] A. Walsh, J. L. F. Da Silva, and S. H. Wei, "Multi-component transparent conducting oxides: Progress in materials modelling," *J. Phys. Condens. Matter*, vol. 23, no. 33, 2011, doi: 10.1088/0953-8984/23/33/334210.
- [158] T. Moriga, T. Okamoto, K. Hiruta, A. Fujiwara, I. Nakabayashi, and K. Tominaga, "Structures and Physical Properties of Films Deposited by Simultaneous DC Sputtering of ZnO and In<sub>2</sub>O<sub>3</sub> or ITO Targets," *J. Solid State Chem.*, vol. 155, no. 2, pp. 312–319, Dec. 2000, doi: 10.1006/JSSC.2000.8919.
- [159] S. Martha, K. H. Reddy, and K. M. Parida, "Fabrication of In<sub>2</sub>O<sub>3</sub> modified zno for enhancing stability, optical behaviour, electronic properties and photocatalytic activity for hydrogen production under visible light," *J. Mater. Chem. A*, vol. 2, no. 10, pp. 3621–3631, 2014, doi: 10.1039/c3ta14285j.
- [160] K. D. Li and K. S. Chang, "Effects of Zn Ratio Tuning on the Structural and Transport Properties of Amorphous Indium Zinc Tin Oxide Thin Films," *J. Electron. Mater.*, vol. 49, no. 12, pp. 7336–7342, 2020, doi: 10.1007/s11664-020-08502-2.
- [161] S. J. Seo, C. G. Choi, Y. H. Hwang, and B. S. Bae, "High performance

- solution-processed amorphous zinc tin oxide thin film transistor,” *J. Phys. D. Appl. Phys.*, vol. 42, no. 3, p. 035106, 2009, doi: 10.1088/0022-3727/42/3/035106.
- [162] P. Y. Liao *et al.*, “Effect of mechanical-strain-induced defect generation on the performance of flexible amorphous In-Ga-Zn-O thin-film transistors,” *Appl. Phys. Express*, vol. 9, no. 12, p. 124101, 2016, doi: 10.7567/APEX.9.124101.
- [163] J. E. Medvedeva, D. B. Buchholz, and R. P. H. Chang, “Recent Advances in Understanding the Structure and Properties of Amorphous Oxide Semiconductors,” *Adv. Electron. Mater.*, vol. 3, no. 9, p. 1700082, 2017, doi: 10.1002/aelm.201700082.
- [164] R. Khanal, D. B. Buchholz, R. P. H. Chang, and J. E. Medvedeva, “Composition-dependent structural and transport properties of amorphous transparent conducting oxides,” *Phys. Rev. B - Condens. Matter Mater. Phys.*, vol. 91, no. 20, pp. 1–13, 2015, doi: 10.1103/PhysRevB.91.205203.
- [165] L. Chen, N. Kumari, and Y. Hou, “Thermal resistances of crystalline and amorphous few-layer oxide thin films,” *AIP Adv.*, vol. 7, no. 11, p. 115205, 2017, doi: 10.1063/1.5007299.
- [166] P. Nath and K. L. Chopra, “Related content Amorphous/epitaxial superlattice for thermoelectric application,” *Japanese J. Appl. Phys. To*, vol. 13, p. 781, 1974.
- [167] H. A. Can, B. Tönbül, F. Pişkin, T. Öztürk, and H. Akyıldız, “Processing optimization of SiO<sub>2</sub>-capped aluminum-doped ZnO thin films for transparent heater and near-infrared reflecting applications,” *J. Mater. Sci. Mater. Electron.*, vol. 32, pp. 5116–5137, 2021, doi: 10.1007/s10854-021-05245-6.
- [168] B. Tönbül, H. A. Can, T. Öztürk, and H. Akyıldız, “Solution processed glass/fluorine-doped tin oxide/aluminum-doped zinc oxide double layer thin films for transparent heater and near-infrared reflecting applications,” *J. Sol-*

*Gel Sci. Technol.*, vol. 99, no. 3, pp. 482–496, 2021, doi: 10.1007/s10971-021-05591-1.



